Grain Boundary Engineering in Sintered Nd-Fe-B Permanent Magnets for Efficient Utilization of Heavy Rare Earth Elements

Korngrenzenmodifikation in gesinterten Nd-Fe-B Permanentmagneten zur effizienten Nutzung schwerer Seltenerd-Elemente

Dissertation genehmigt zur Erlangung des akademischen Grades Doktoringenieur (Dr.-Ing.)

vorgelegt dem Fachbereich Material- und Geowissenschaften der Technischen Universität Darmstadt

von Dipl.-Ing. Konrad Löwe aus Stralsund

TECHNISCHE UNIVERSITÄT DARMSTADT

Tag der Einreichung: 18.10.2016
Tag der mündlichen Prüfung: 13.12.2016

1. Gutachter: Prof. Dr. Oliver Gutfleisch
2. Gutachter: Prof. Dr. George C. Hadjipanayis

Darmstadt 2016
Hochschulkennziffer D17

Erklärung zur Dissertation

Hiermit versichere ich, die vorliegende Dissertation ohne Hilfe Dritter nur mit den angegebenen Quellen und Hilfsmitteln angefertigt zu haben. Alle Stellen, die aus Quellen entnommen wurden, sind als solche kenntlich gemacht. Diese Arbeit hat in gleicher oder ähnlicher Form noch keiner Prüfungsbehörde vorgelegen.

Darmstadt, den 14. Oktober 2016

Konrad Löwe

Abstract

The first part of the thesis investigates the diffusion of rare-earth (RE) elements in commercial sintered Nd-Fe-B based permanent magnets. A strong temperature dependence of the diffusion distance and resulting change in magnetic properties were found. A maximum increase in coercivity of ≈+350 kA/m using a Dy diffusion source occurred at the optimum annealing temperature of 900 °C. After annealing for 6 h at this temperature, a Dy diffusion distance of about 4 mm has been observed with a scanning Hall probe. Consequently, the maximum thickness of grain boundary diffusion processed magnets with homogeneous properties is also only a few mm. The microstructural changes in the magnets after diffusion were investigated by electron microscopy coupled with electron probe microanalysis. It was found that the diffusion of Dy into sintered Nd-Fe-B permanent magnets occurs along the grain boundary phases, which is in accordance with previous studies. A partial melting of the Nd-Fe-B grains during the annealing process lead to the formation of so - called (Nd,Dy)-Fe-B shells at the outer part of the grains. These shells are µm thick at the immediate surface of the magnet and become thinner with increasing diffusion distance towards the center of the bulk. With scanning transmission electron microscopy coupled with electron probe analysis a Dy content of about 1 at.% was found in a shell located about 1.5 mm away from the surface of the magnet. The evaluation of diffusion speeds of Dy and other RE (Tb, Ce, Gd) in Nd-Fe-B magnets showed that Tb diffuses significantly faster than Dy, and Ce slightly slower than Dy, which is attributed to differences in the respective phase diagrams. The addition of Gd to the grain boundaries has an adverse effect on coercivity. Exemplary of the heavy rare earth element Tb, the nano - scale elemental distribution around the grain boundaries after the diffusion process was visualized with high resolution scanning transmission electron microscopy.

The second part of the thesis explores an experimental production technique for (Nd,Dy)-Fe-B sintered magnets that involves blending powders with different Dy contents and grain sizes. As precursors, a Dy - free *base powder* (BP) and a Dy - rich *anisotropy powder* (AP) were mixed. During the sintering, a core - shell microstructure was created, similar to the immediate surface region of grain boundary diffusion processed magnets. However, the powder blending technique allows the production of magnets of any size, without the geometric limitations of the grain boundary diffusion process. As a novelty to previous works, the AP consists mainly of (Nd,Dy)-Fe-B ϕ - phase instead of Dy - rich binary compounds. The main advantages are the avoidance of deleterious secondary phases within the magnet and a decreased sintering temperature. Of the several used AP compounds, the best magnetic properties were achieved with thermally homogenized $(Nd_{0.725}Dy_{0.275})_{15}Fe_{79}B_6$. However, with 1.63 T the coercivity of the blended

magnet is below the value of a conventionally produced single - powder magnet. The reason is most likely the presence of a high amount of grains with Dy - rich cores within the microstructure, as was found with scanning electron microscopy. These grains are unmolten AP particles, which were not milled fine enough. To solve this problem, the utilization of more sophisticated milling equipment than the planetary ball milling available in this work is proposed.

Zusammenfassung

Im ersten Teil der Doktorarbeit wurde die Diffusion von Seltenerd-Elementen in kommerziellen Nd-Fe-B basierten Permanentmagneten untersucht. Eine starke Temperaturabhängigkeit der Diffusionsweite und der daraus resultierenden Veränderungen der magnetischen Eigenschaften konnte festgestellt werden. Der Anstieg der Koerzitivfeldstärke von ≈+350 kA/m für Dy als Diffusionsquelle ist maximal bei der optimalen Glühtemperatur von 900 °C. Nach einer sechsstündigen Glühbehandlung bei dieser Temperatur wurde mit einer Hall Sonde eine Diffusionsweite von Dy von etwa 4 mm beobachtet. Dies entspricht auch ungefähr der maximalen Dicke, die ein korngrenzenmodifizierter Magnet in Diffusionsrichtung haben darf, wenn homogene magnetische Eigenschaften erreicht werden müssen. Die Gefügeveränderung in den diffusionsbehandelten Magneten wurden mit Elektronenmikroskopie und energie- bzw. wellenlängendispersiver Röntgenspektroskopie untersucht. Es wurde gezeigt, dass die Diffusion von Dy über die Korngrenzen des Nd-Fe-B Magneten geschieht. Das partielle Aufschmelzen der Außenbereiche der Körner führt hierbei zur Bildung sogenannter (Nd,Dy)-Fe-B Schalen. Diese Schalen sind in direkter Oberflächennähe des Magneten einige µm breit, werden mit zunehmender Diffusionsweite aber schmaler, bis sie nach etwa 0.5 mm nur noch einige nm breit sind. In einer Eindringtiefe von 1.5 mm wurde mit Transmissionselektronenmikroskopie eine Dy Konzentration von etwa 1 at.% in den Schalen nachgewiesen. Die Untersuchung der Diffusionsgeschwindigkeiten von Dy und anderen seltenen Erden (Tb, Ce, Gd) in Nd-Fe-B Magneten zeigt, dass Tb signifikant schneller und Ce etwas langsamer diffundiert als Dy. Dies wurde mit Unterschieden in den jeweiligen Phasendiagrammen erklärt. Das Einbringen von Gd in die Korngrenzenbereiche hat eine schädliche Wirkung auf die Koerzitivfeldstärke. Die nanoskalige Tb Elementverteilung um eine Korngrenze wurde mittels hochaufgelöster Rastertransmissionselektronenmikroskopie dargestellt.

Der zweite Teil der Arbeit untersucht eine experimentelle Herstellungsmethode für gesinterte (Nd,Dy)-Fe-B Magneten, die dadurch gekennzeichnet ist, dass vor dem Sintern ein Dy - freies *Basispulver* (BP) und ein Dy - reiches *Anisotropiepulver* (AP) miteinander gemischt werden. Das Gefüge der späteren

Magnete zeigt eine ausgeprägte Kern - Schalen Struktur, ähnlich dem Gefüge in den Randbereichen korngrenzendiffundierter Magnete. Vorteilhaft an deuen Technik ist, dass Proben beliebiger Größe hergestellt werden können, ohne die geometrischen Beschränkungen des Korngrenzen-diffusionsprozesses. Eine Neuerung gegenüber bestehender Literatur ist, dass das AP hauptsächlich aus (Nd,Dy)-Fe-B ϕ - Phase besteht, anstelle von elementarem Dy oder binären Dy - reichen Verbindungen. Die Hauptvorteile dieser Herangehensweise sind, das keine unerwünschten Zweitelemente in den Magneten eingebracht werden und eine starke Erniedrigung der Sintertemperatur erreicht wird. Von den untersuchten AP Verbindungen wurden hierbei die besten magnetischen Eigenschaften mit thermisch homogenisiertem $(Nd_{0.725}Dy_{0.275})_{15}Fe_{79}B_6$ erzielt. Allerdings ist die Koerzitivfeldstärke trotzdem geringfügig kleiner als die eines aus einem Pulver hergestellten Vergleichsmagneten. Ein mögliche Erklärung ist, dass ein Teil des AP beim Sintern nicht aufschmilzt und so das in den Partikeln enthaltene Dy nicht auf die Korngrenzen wirken kann. Zur Verbesserung des Prozesses wird die Verwendung von komplexeren Mahltechniken als das in dieser Arbeit zur Verfügung stehende Planetenkugelmahlen vorgeschlagen.

Content

List of figures

List of tables

List of abbreviations and symbols

3DAP	3-dimensional atom probe
AP	axial field pressing
AP	anisotropy powder
BP	base powder
BSE	backscatter electron
CIP	cold isostatic pressing
DOT	degreea of texture
DSC	differential scanning calorimetry
EBSD	electron backscatter diffraction
EDX	energy dispersive spectroscopy
FEM	finite element
GB	grain boundary
GBD	grain boundary diffusion
GBDP	grain boundary diffusion process
GBP	grain boundary phase
GBT	grain boundary tail
HAADF	high angle annular dark field
HCS	Helmholtz coil setup
HD	hydrogen decrepitation
HDDR	Hydrogenation Disproportionation Desorption Recombination
HRE	heavy rare earth
HRTEM	high-resolution transmission electron microscopy
ICP-OES	Inductively coupled plasma atomic emission spectroscopy
JM	jet mill
LRE	light rare earth
MOKE	magneto-optical Kerr effect
PSA	post-sinter annealing
RE	rare earth
RIP	rubber isostatic pressing
RT	room temperature
SC	strip casting
SC	single crystalline
SE	secondary electron
SEM	scanning electron microscopy
SPD	singular point detection
STEM	scanning transmission electron microscopy
TEM	transmission electron microscopy
TP	transversal field pressing
VSM	vibrating sample magnetometer
WDX	wavelength dispersive spectroscopy
XRD	X-ray diffraction

α	Kronmüller parameter α
$\alpha_K \alpha_\psi$	Kronmüller parameter $\alpha_K \alpha_\psi$
A	area
B	magnetic flux density
B_r	remanent magnetic flux density
$(BH)_{max}$	maximum energy product
c	concentration
c_{bulk}	bulk concentration
c_{surf}	surface concentration
D	bulk diffusion coefficient
d	grain size
d_{50}	mean particle diameter
d_{crit}	critical particle diameter
δ	grain boundary width
D_d	dislocation pipe diffusivity
D_{Dy}	diffusion coefficient of Dy
D_{eff}	effective diffusion coefficient
D_{gb}	grain boundary diffusion coefficient
D_s	surface diffusion coefficient
E_0	electrochemical standard potential
g	volumetric ratio of grain boundaries to bulk material
H	magnetic field strength
H_a	anisotropy field
H_c, $H_{c,M}$ / $H_{c,B}$	coercivity, coercivity of the M(H) / B(H) curve
$H_{c,bulk}$	bulk coercivity
$H_{c,surf}$	surface coercivity
H_{ci}	coercivity of slice i
H_{ext}	external magnetic field strength
H_i	inner magnetic field strength
H_N	nucleation field
H_S	switching field
J	magnetic polarization
J_r	remanent polarization
J_r'	open circuit remanent polarization
J_s	saturation polarization
K_1	anisotropy constant 1
L	liquid phase
M	magnetization
M_r	remanent magnetization or remanence
M_r'	open circuit remanent magnetization or remanence
M_s	saturation magnetization
$M_{s,theo}$	theoretical saturation magnetization
μ, μ_0	permeability, vacuum permeability
N	number of coil windings
$\mathcal{N}$	demagnetization factor
$\mathcal{N}_{eff}$	effective demagnetization factor
Φ	magnetic flux

ϕ, $\tau 1$	$Nd_2Fe_{14}B$ phase
r_{crit}	critical radius
s	segregation factor
T	temperature (quantity) / Tesla (unit)
t	time
η, $\tau 2$	$Nd_{1.1}Fe_4B_4$ phase
T_a	annealing temperature
T_c	Curie - temperature
T_m	melting temperature
U	voltage
V_i	volume of slice i
V_{tot}	total volume
x	diffusion length, lateral distance
x_{bulk}	bulk diffusion length

1. Introduction

When in the late 70's the price of Co increased drastically due to a politically unstable supply situation in the Democratic Republic of the Congo, it spurred the research community to replace Sm-Co based permanent magnets, which showed the highest energy product at the time. After only a few years, a permanent magnet material based on Nd-Fe-B was developed in 1984 almost in parallel by M. Sagawa at Sumitomo Special Metals, who used a powder metallurgic production route [Sagawa1984] and J.J. Croat at the General Motors Research Laboratories, who produced the magnets via rapid solidification [Croat1984]. Already one year before, Hadjipanayis et al. produced a compound similar to $Nd_2Fe_{14}B$ with small Si additions, also via rapid solidification [Hadjipanayis1983]. Of the three, M. Sagawa gained commercial success by upscaling the magnet production to 10.000 t/year in 2000 [Sagawa2012]. In 2008 the worldwide production volume was already 63.000 t with an estimated growth rate of 12 % per year [Gutfleisch2011]. A detailed description of the early research on Nd-Fe-B with numerous references can be found in the review of Herbst [Herbst1991]. The newly developed Nd-Fe-B magnets surpass the energy product of all previously known magnetic materials by almost a factor of two until the present day [Gutfleisch2011].

Critical key components of the Nd-Fe-B based magnets are rare earth (RE) elements, especially Nd, Pr, Dy and Tb. While the former two are classified as light RE (LRE), the latter two are heavy RE (HRE) and are added in small quantities to increase the high temperature stability of the compound. The RE never occur in pure form but chemically bound in minerals [Bauer2010]. Because of their chemical similarity, the overall process of RE production is extremely complex and expensive, especially for the HRE. The waste products of the production process include radionuclides and strong acids, which pose a significant environmental threat. In the last 30 years these problems lead to the shift of RE production almost exclusively to China, because of its lower ecological standards. Nowadays the country produces 98% of the RE worldwide [Reller2013, Weber2012]. This monopolistic market situation can lead to severe problems, as was experienced recently in the so - called "rare earth crisis" caused by Chinese trade restrictions. It started in September 2010 when China suspended shipments of the minerals to Japan over territory disputes, followed by a stepwise reduction in maximum worldwide export quotas. As a consequence, the prices for several RE rose considerably, in the middle of 2011 even dramatically, up to almost 3000 % compared to the price in 2008 (Figure 1-1). This development led to the (re-)opening of

RE mines outside of China [Hatch2011]. The two biggest and most prominent examples are the Mountain Pass mine in California, owned by Molycorp, Inc. and is the Mount Weld mine in Australia, owned by Lynas Corporation, Ltd (see price chart in Figure 1-1). After it became clear in late 2011 that the RE shortage was not as critical as previously believed [EU Commission2010], prices began to decrease again. This led to the shutdown of the Mountain Pass mine in late August 2015 and Molycorp's bankruptcy [Molycorp Inc.2015]. Similarly, Lynas stock price is very low today. These two cases show that the establishment of RE sources outside of China, especially for HRE, is difficult, expensive and very much dependant on Chinese politics.

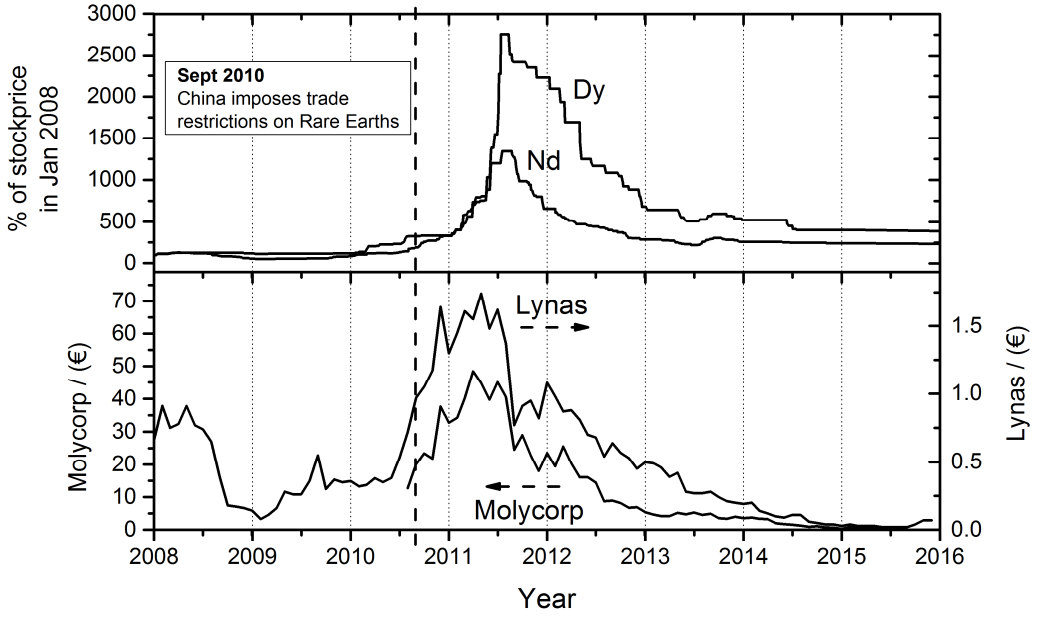

Figure 1-1: Dy and Nd price development [www.metal-pages.com] correlated with stock prices of the mining companies Lynas Corporation, Ltd and Molycorp, Inc. [www.nasdaq.com]

To counteract the dependency on China and the resulting supply risk as well as because of environmental concerns of RE mining, increased research efforts have been undertaken to either develop substitutes for HRE or reduce the amount of needed material, as well as the improvement of recycling. While the latter is still in its infancy, a lot of recent research projects focus on the former [Gauß2016]. Two examples, and the topics of this thesis, are the reduction of HRE in Nd-Fe-B sintered magnets via the grain boundary diffusion process (GBDP) as well as novel production technique involving the blending of two or more powders with different HRE contents.

The GBDP was developed in 2000 [Park2000] and is nowadays an industrially established technique to magnetically upgrade Nd-Fe-B sintered magnets for demanding applications, where high requirements on coercivity and temperature stability justify the somewhat increased price. It involves the coating of the magnets with HRE and a subsequent annealing, during which the HRE diffuse into the bulk of the material and enhance its magnetic properties. In the last decade a lot of research was dedicated to the optimization of the process (a short literature review can be found in chapter 2.2.2). Despite these research efforts, some fundamental phenomena have not been addressed yet. Neither an accurate determination of the temperature dependent HRE diffusion coefficients along the grain boundary phase, nor a direct correlation between the overall coercivity and HRE concentration gradients occurring in diffusion processed Nd-Fe-B magnets has been established. In the first part of chapter 4 the influence of the annealing temperature on the magnetic properties and microstructure of Nd-Fe-B sintered magnets after a Dy diffusion process is evaluated and possible diffusion mechanisms elucidated. The second part expands the focus to other RE, namely Tb, Gd and Ce.

One of the drawbacks of the GBDP is that it is limited to thin magnets of not more than about 5 mm thickness in diffusion direction. This limitation is overcome by the mentioned novel powder blending technique, which creates a favorable microstructure similar to the one realized with the GBDP, but without size restrictions. As a fundamental difference to the GBDP, it is applied already during sintering by mixing powders with different HRE contents. To this day, HRE are introduced into Nd-Fe-B magnets only through binary Dy - rich compounds, which have been investigated as blending powders (Chapter 2.3 gives a review on the existing literature). These approaches suffer from a number of drawbacks, of which one is a relatively high required sintering temperature leading to a reduced coercivity. To overcome this problem the blending process with ternary and quaternary (Nd,Dy)-Fe-B based compounds is investigated in chapter 5.

2. Basics

2.1. The Nd-Fe-B system

The following chapter is divided into three parts: First, the crystal structure and intrinsic properties of the $Nd_2Fe_{14}B$ phase are described [Coey2010, Graham2009, Hubert2014]. Where necessary, a brief explanation of basic concepts of magnetism is given. A detailed description of these concepts can be found in textbooks and is not repeated here. The second part deals with the magnetization reversal mechanism and microstructure of sintered Nd-Fe-B permanent magnets. The focus of the microstructural description lies on Nd-Fe-B magnets produced by sintering. Other production routes, e.g. HDDR processing or hot-deformation, are discussed elsewhere [Gutfleisch2000]. Finally, the industrial production process of sintered Nd-Fe-B magnets is described in detail.

2.1.1. Crystal structure and intrinsic properties of $Nd_2Fe_{14}B$ and related structures

$Nd_2Fe_{14}B$ ("ϕ - phase") crystallizes in the *$P4_2/mnm$* space group and has a tetragonal symmetry [Herbst1991]. Each unit cell contains 4 formula units with a total of 68 atoms (Figure 2-1). There are 2 distinct crystallographic sites for Nd, 6 for Fe and 1 for B. The unit cell parameters are a = 8.80 Å and c = 12.20 Å. Characteristic for the structure are double layered Fe rings, which are sandwiched between Nd and B atoms. These rings are visible in high-resolution transmission electron microscopic images [Woodcock, Ramasse, 2014]. In the unit cell, the Nd with 4f electron states is responsible for the high magnetic anisotropy, whereas the Fe with 3d electron bands is responsible for the large magnetic moment and the ferromagnetic coupling which ensures a high Curie temperature [Fahnle1993]. B contributes to the thermodynamic stability of the structure [Herbst1991]. Through substitution of Nd with other rare earth (RE) elements the intrinsic properties of the structure change dramatically. The change of the properties scales approximately linearly with the ratio of replaced RE [Hirosawa1986]. A selection of the most relevant candidates for the present work are listed in Table 2-1. The replacement of Nd with the heavy RE Dy and Tb increases the anisotropy field H_a by a factor of 2 and 3, respectively. The Nd replacement with Ce and Gd reduces it almost by a factor of 3. For Nd and all the other light rare earths (LRE) the total magnetic moment couples ferromagnetically to the total magnetic moment of Fe. For the heavy rare earths (HRE), including Dy, Tb and Gd, it couples antiferromagnetically.

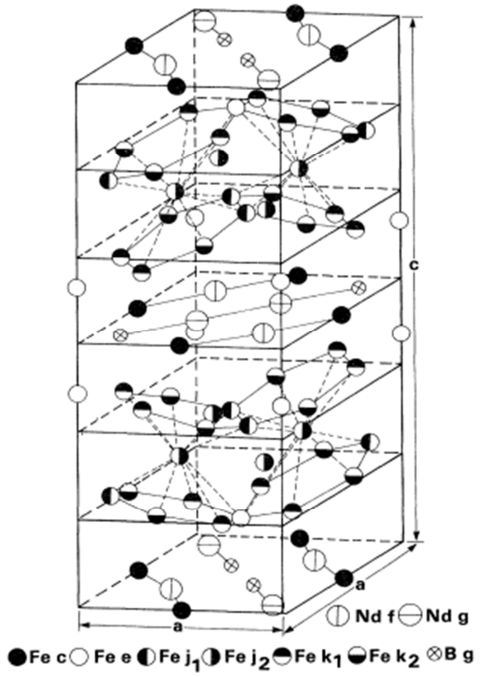

Figure 2-1: Crystal structure of $Nd_2Fe_{14}B$ [Herbst1991].

In the $R_2Fe_{14}B$ compounds with R = La, Ce, Lu, Th and Y in first approximation the RE does not contribute to the total magnetic moment at T = 4 K, leaving only the magnetic moment of the Fe sublattices [Herbst1991]. In other words, the saturation magnetization μ_0*M_s of e.g. $Ce_2Fe_{14}B$ is blank with respect to the RE and can be regarded approximately as only caused by Fe. In $(LRE)_2Fe_{14}B$, with the most prominent $Nd_2Fe_{14}B$, μ_0*M_s is increased and in $(HRE)_2Fe_{14}B$ it is decreased because of ferromagnetic / antiferromagnetic coupling of the different magnetic moments. The Curie temperatures of $R_2Fe_{14}B$ (R = Nd, Dy, Tb) lie close together at 585 - 620 K. For $Gd_2Fe_{14}B$ it is a bit higher at 661 K and for $Ce_2Fe_{14}B$ it is decreased to 424 K.

Table 2-1: Intrinsic magnetic properties of selected RE-Fe-B compounds [Herbst1991].

(T=295 K)	μ_0*M_s / (T)	μ_0*H_a / (T)	T_c / (K)
$Nd_2Fe_{14}B$	1.60	7.30	585
$Ce_2Fe_{14}B$	1.17	2.60	424
$Dy_2Fe_{14}B$	0.71	≈15	598
$Tb_2Fe_{14}B$	0.70	≈22	620
$Gd_2Fe_{14}B$	0.89	2.40	661

Other substitutional elements are e.g. Co, Al, Ga, Cu for Fe and C for B. A detailed description of their effects can be found in the literature [Herbst1991]. A list of additives which primarily influence the microstructure of Nd-Fe-B permanent magnets is given in chapter 2.1.3. In the following, the most important characteristic micromagnetic length scales and parameters are briefly introduced.

The magnetic exchange energy in the continuum picture is described as

$$\epsilon_{ex} = \int A(\nabla e_M)^2 dV \qquad \textbf{2-1}$$

where A is the exchange stiffness, describing the energy of the ferromagnetic coupling and e_M is a unit vector in the direction of the magnetization. A has the unit of *energy/length* and can be approximated by the relation

$$A \approx \frac{k_B T_c}{2a_0} \qquad \textbf{2-2}$$

where T_c is the Curie temperature and a_0 the lattice parameter in a simple structure. The competition between the exchange energy ϵ_{ex} and the dipolar energy ϵ_d is characterized by the *exchange length*:

$$l_{ex} = \sqrt{\frac{A}{\mu_0 M_s^2}} \qquad \textbf{2-3}$$

It is the shortest length on which the magnetization can be twisted in order to minimize the dipolar interaction.

The crystalline anisotropy energy E_a is related to the difference in energy of the magnetization with respect to the crystallographic axes of a given structure. The direction in which the energy is minimized is called the easy direction. In a uniaxial crystallographic system E_a is defined as

$$E_a = K_1 \sin^2\theta + K_2 \sin^4\theta + \cdots \qquad \textbf{2-4}$$

where K_1 and K_2 are anisotropy constants and θ is the angle between the easy axis and the direction of magnetization. For Nd-Fe-B in first approximation K_2 can be set to 0. Between two magnetic domains of different orientation the magnetization vector has to change its direction. It rotates continuously over many interatomic distances under the combined influence of exchange and anisotropy. The transition length, the so-called *domain wall width*, can be approximated by

$$\delta_W \approx \sqrt{A/K_1} \qquad \textbf{2-5}$$

The associated *domain wall energy* can be expressed as

$$\gamma_W \approx \sqrt{AK}_1 \qquad \textbf{2-6}$$

Selected values of the described parameters for the $Nd_2Fe_{14}B$ compound can be found in Table 2-2.

Table 2-2: Micromagnetic parameters and characteristic length scales for $Nd_2Fe_{14}B$ [Coey2010]. exchange stiffness A, anisotropy constant K_1, exchange length l_{ex}, domain wall width δ_W, domain wall energy γ_W.

A [pJ/m]	K_1 [MJ/m^3]	l_{ex} [nm]	δ_W [nm]	γ_W [mJ/m^2]
8.0	4.9	1.9	3.9	25

2.1.2. Magnetization reversal mechanism and microstructure of sintered Nd-Fe-B permanent magnets

The excellent intrinsic properties of the $Nd_2Fe_{14}B$ phase have to be “translated” into extrinsic properties of permanent magnets. Most important are the remanence M_r and the coercivity H_c. M_r is the remaining magnetization of the permanent magnet without an external field H_a. It is directly proportional to the saturation magnetization M_s, reduced by the percentage of non - magnetic secondary phases and the degree of alignment of the easy axes of the single particles with respect to the macroscopic easy axis of the magnet. The alignment can be expressed as degree of texture (DOT), which is the ratio of M_r/M_s [Eckert1991]. DOT is 0.5 for an isotropic magnet and 1.0 for an ideal texture. H_c is defined as the internal magnetic field, which is needed to reduce the magnetization of a previously magnetized magnet to 0. It is denoted as $H_{c,M}$ or $H_{c,B}$ for M(H) or B(H) curves, respectively. In this work, H_c is always $H_{c,M}$, unless otherwise specified. H_c scales with H_a and is very much dependent on the microstructure of the magnet.

H_c in permanent magnets is usually expressed by the inequality

$$H_c \geq \left(\frac{2K_1}{\mu_0 M_s}\right) - \mathcal{N} M_s \qquad \textbf{2-7}$$

based on the famous Stoner - Wohlfarth model, where magnetization reversal happens by coherent rotation in a uniformly magnetized ellipsoid [Stoner1948]. K_1 denotes the anisotropy constant, M_s the saturation magnetization and $\mathcal{N}$ the demagnetization factor of the magnet geometry [Coey2010]. In practice however, H_c is only about 20 - 30% of the theoretical maximum, the anisotropy field H_a (with $H_a = \frac{2K_1}{\mu_0 M_s}$). This discrepancy is known as Brown's paradox [Brown1945] and is displayed in Figure 2-2, where an actual hysteresis loop of a permanent magnet is displayed against the theoretical one.

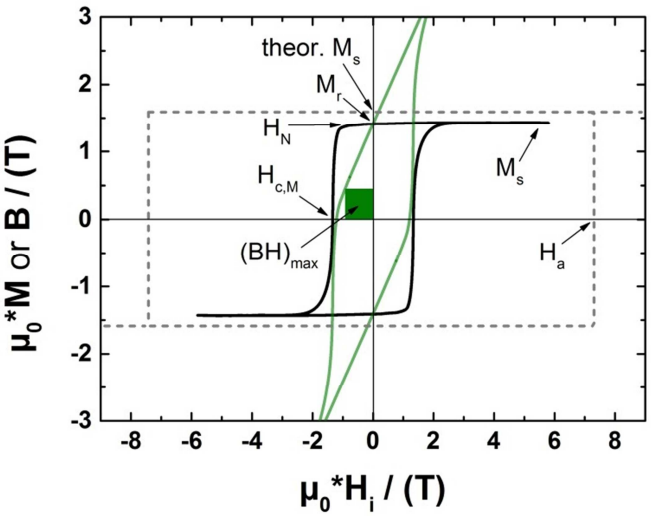

Figure 2-2: Comparison of an experimental hysteresis loop μ_0*M(H_i) (full black line) of an sintered Nd-Fe-B magnet with the theoretical hysteresis loop (blacked dashed line) after equation 2-7. Also shown is B(H_i) (full green line). The values for the theoretical M_s and H_a can be found in Table 2-1. H_a … anisotropy field, M_r … remanence, M_s … saturation magnetization, H_N … nucleation field, $H_{c,M}$ … coercivity of the M(H) curve, $(BH)_{max}$ … maximum energy product.

The reason for the huge discrepancy between H_a and H_c is attributed to randomly occurring structural defects at the surface of the grains, where the magnetocrystalline anisotropy is locally reduced [Woodcock2012]. Here, reversed domains can nucleate at fields much smaller than H_a , making Nd-Fe-B a so - called nucleation - based permanent magnet [Kronmüller1987]. Once the reversal started, the

energy needed to progress the created domain wall through the volume of the grain is very small [Kronmüller1987, Kronmüller1988]. To create a nucleus of reversed magnetization in a homogeneously magnetized grain, the nucleation field H_N has to be applied, which should ideally be as close as possible to H_c. Kronmüller has formulated a relation based on equation 2-7 that approximates H_c of permanent magnets:

$$H_c = \alpha_K \alpha_\psi * H_a - N_{eff} * M_s \qquad \textbf{2-8}$$

H_a denotes the anisotropy field and M_s the saturation magnetization, α_K, α_ψ and N_{eff} are empirical parameters, to be determined from experiment [Kronmüller1987]. α_ψ describes the effect of misalignment of the $Nd_2Fe_{14}B$ grains, and α_K the decrease in the magnetocrystalline anisotropy of the grain surface, which is attributed to the effect of magnetic inhomogeneities with a radius r_{crit}. N_{eff} is an effective demagnetizing factor, which is influenced by the grain size and shape as well as the amount of non - magnetic impurities in the microstructure. Through temperature dependent measurements of H_a, M_s and H_c the described parameters can be obtained. With a simple geometric description Kronmüller links the α_K parameter to the size r_{crit} of the magnetic inhomogeneities and conclude that magnetization reversal happens through coherent rotation within the defects [Kronmüller1987]. They calculate that in order to eliminate the deteriorating effects of magnetic inhomogeneities their size should be smaller than $r_{crit} < 5$ nm. An alternative approach to explain the magnetization reversal was developed by Givord et al. [Givord1988]. It is based on the hypothesis that the reversal starts in an “activation volume” at the grain surfaces, in which a domain wall forms, as opposed to the coherent rotation in the Kronmüller model. In their work they calculate that in a sintered Nd-Fe-B magnet at 300 K, the activation volume is about 500 nm^3. If one assumes a spherical volume this corresponds to a radius of 4 nm.

The increase in computational power in recent years made it possible to use micromagnetic simulations to obtain physical properties of the defect regions. With atomistic calculations Hrkac et al. [Hrkac2010] determined the thickness of distortions in the $Nd_2Fe_{14}B$ structure at the grain surface due to a lattice mismatch with the grain boundary phase and found values varying between 0.4 nm and 1.6 nm. These distorted regions show a reduced local magnetic anisotropy and are reasoned to cause the decrease in H_c. Using finite element micromagnetics, Bance et al. [Bance, Oezelt, 2014] calculated the angular dependency of coercivity in hot - deformed nano - crystalline NdFeB magnets. Assuming defect thicknesses at the grain surface of 1.2 - 2.8 nm they were able to achieve very good agreement with

experimental data. The calculated values for the defect layer thicknesses in both works are consistent with the characteristic micromagnetic length scales given in Table 2-2.

To counteract the magnetic reversal, a special microstructure has been developed (Figure 2-3). It consists of single crystalline $Nd_2Fe_{14}B$ grains with a size of 3 -10 µm, which are surrounded by a continuous layer of amorphous Nd - rich phase with a thickness of only a few nm and larger Nd - rich phases in the grain junctions [Woodcock2012]. Each grain acts as an independent small magnet. The thin grain boundary smoothes the grain surfaces and eliminates to an extent the number of the described structural defects, which decreases the probability of nucleation of reversed domains. Furthermore, the grain boundary phase (GBP) magnetically decouples the grains, which prevents reversal "avalanches" within the magnet. The GBP is generally believed to be paramagnetic, although newer studies claim to have found a significant amount of Fe inside, rendering the phase weakly ferromagnetic [Sepehri-Amin, Ohkubo, Nagashima, 2013].

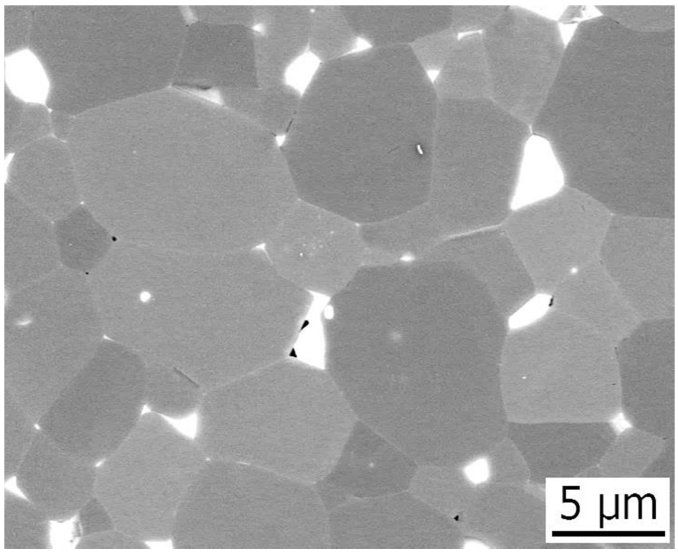

Figure 2-3: BSE SEM image of a typical microstructure of a sintered Nd-Fe-B permanent magnet. In grey are the $Nd_2Fe_{14}B$ singly crystalline grains and the white regions are Nd - rich phase. The faint bright contrast between the grains stems from the nanometer sized grain boundary phase.

2.1.3. Industrial production process of sintered Nd-Fe-B magnets

The industrial sintering process of Nd-Fe-B permanent magnets is divided into 8 main parts (A-H), which are schematically depicted in Figure 2-4: The alloy with the desired composition (A) is produced via a

rapid solidification technique called „strip casting“ (B), which is similar to melt - spinning, with less rapid cooling rates. Afterwards, the ingot is hydrogen - decrepitated (C), crushed and milled into a fine powder (D). This powder consists now of single crystalline Nd-Fe-B particles with a size of 5 - 10 µm, which are filled in a press form, aligned in a magnetic field and pressed to the desired shape (E). The green compact is finally sintered (F) and annealed (G) at lower temperatures. A coating is applied to protect the magnet against corrosion (H).

In the following the individual steps are described in more detail.

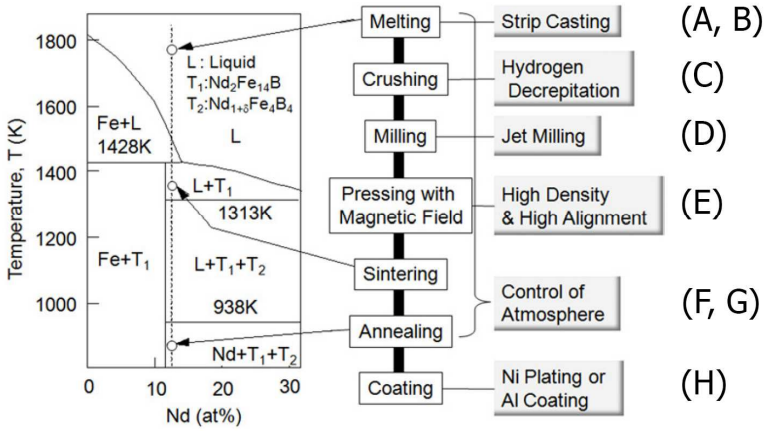

Figure 2-4: Production route of NdFeB sintered permanent magnets [Sugimoto2011]

A. Production of the pre - alloy

In the final magnet a maximum amount of the main $Nd_2Fe_{14}B$ phase (“ϕ” or “τ1”) is desirable. Also, a certain amount of liquid Nd - rich phase (“L”) needs to be present during the sintering process to ensure a rapid densification of the magnets and therefore limited grain growth. Shown in Figure 2-5 is an Isothermal section through the Nd-Fe-B phase diagram at 1000 °C, i.e. approximately sintering temperature [Malfliet2008]. Following the two requirements the sintering should take place in the “ϕ + L” phase region. If the composition shifts, e.g. by oxidation of Nd during the production process, a number of other secondary phases will appear, among them $Nd_{1.1}Fe_4B_4$ (“η” or “τ2”), γ - Fe, Fe_2B and Nd_2Fe_{17}. The η - phase is paramagnetic at room temperature and will decrease the magnetization of the final magnet (because it is “dead space”). The other phases are all ferromagnetic at room temperature

and considered to be very harmful to the coercivity [Schneider1990] (marked in red in Figure 2-5). Their formation needs to be strictly avoided.

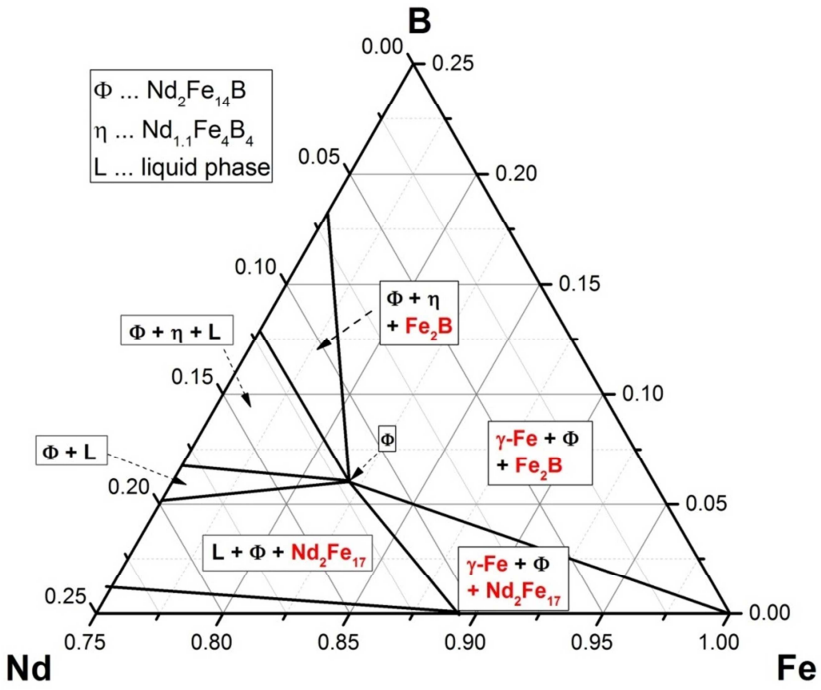

Figure 2-5: Isothermal section through the Fe - rich corner of the ternary Nd-Fe-B phase diagram at 1000 °C [Malfliet2008]. Phases which are softmagnetic at room temperature are marked in red.

The section through the phase diagram for a fixed ratio of Nd:B = 2:1 (as in the ϕ - phase) is shown in Figure 2-6. The Nd - rich liquid phase "L" melts eutectically at 685 °C. In the phase region "L + ϕ" its amount is increasing with higher temperatures. To ensure the presence of enough "L", sintering usually takes place between 1000 °C and 1100 °C. It should be noted that the eutectic temperature of "L" can be drastically lowered to well below 500 °C through the addition of small amounts of additional elements, e.g. Cu. This is important for the post - sinter annealing (PSA) and will be discussed under point G).

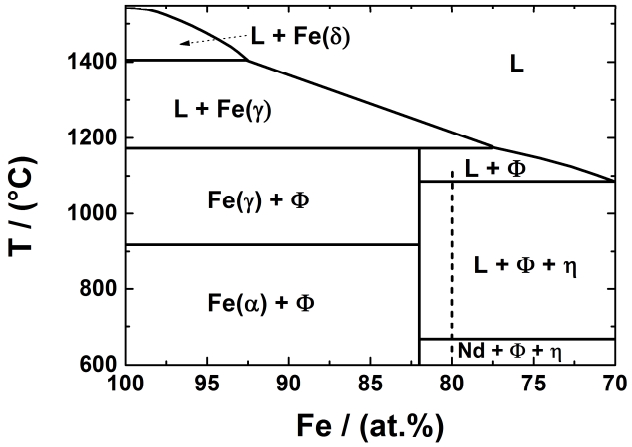

Figure 2-6: Fe - rich part of the quasi-binary phase diagram for a fixed Nd:B ratio of 2:1 (after Schneider et al. [Schneider1986]). ϕ marks the $Nd_2Fe_{14}B_1$ phase, η the $Nd_1Fe_4B_4$ phase. The sintering of magnets usually takes place along the dashed line at a temperature of 1000 - 1100 °C.

The stoichiometric ratio of Nd in the $Nd_2Fe_{14}B$ phase is 11.76 at.%, corresponding to a total formula of $Nd_2Fe_{14}B_1$ / $Nd_{11.76}Fe_{82.35}B_{5.88}$ (at.%) or $Nd_{26.68}Fe_{72.32}B_{1.00}$ (wt.%). To this value a certain surplus of Nd has to be added for the following reasons: a) as mentioned before, to create the Nd - rich liquid phase during sintering b) as magnetic decoupling layer between the grains and c) as a surplus of Nd and B to account for the formation of secondary Nd - boride phases and phases formed with Nd and impurities (C, O, N), which are always picked up during the production process. If one assumes the formation of Nd_2O_3, Nd_1N_1 and Nd_1C_1 [Sasaki2015], the according mass - ratios are approximately Nd : O = 6.0 : 1, Nd : N = 10.3 : 1 and Nd : C = 12.0 : 1, respectively. For the boride phase η a composition of $Nd_{1.1}Fe_4B_4$ is assumed [Malfliet2008], which gives a mass ratio of Nd : boride = 0.60 : 1.

An example: A commercially available sintered Nd-Fe-B magnet typically has the following characteristics:

0.2 wt.% O, 0.03 wt.% N, 0.09 wt.% C, 0.5 wt.% borides [Li2009],

which amounts to a total of 0.2 * 6.0 + 0.03 * 10.3 + 0.09 * 12.0 + 0.5 * 0.60 = 2.89 wt.% of Nd that is used up by impurities and borides. Additionally, the amount of Nd - rich secondary phase which forms the grain boundaries is ideally at least 2 wt.% [Rodewald2002]. The total percentage of Nd in the magnet should therefore be at least 26.68 wt.% (the stoichiometric ratio of the $Nd_2Fe_{14}B$ phase) + 2.89 wt.% + 2

wt.% = 31.57 wt.%. If one assumes a ratio of Fe : B = 14 : 1.05 at.%; (i.e. a surplus of 5% B), this corresponds to a final formula of $Nd_{31.57}Fe_{67.45}B_{0.98}$ (wt.%) or $Nd_{14.43}Fe_{79.60}B_{5.97}$ (at.%).

On the laboratory scale the amount of Nd can be further reduced by also reducing the amount of impurities and at an expense of coercivity, which decreases to a certain extent when there is not enough Nd to magnetically decouple the individual grains. The most extreme example of compositional optimization was reported by Harimoto et al. in 2007 [Harimoto2007]. They produced a Nd-Fe-B sintered magnet with the highest energy product so far, 474 kJ/m^3 (B_r = 1.555 T, $H_{c,M}$ = 653 kA/m) and a composition of $Nd_{27.56}Fe_{71.46}B_{0.99}$ (wt.%) or $Nd_{12.3}Fe_{82.35}B_{5.88}$ (at.%). They claim to have no borides and an oxygen concentration below 0.1 wt.% in the magnet.
To improve the sintering behavior and/or the magnetic and mechanical properties of the final magnets a variety of additives are added [Herbst1991]. They can be classified into 3 categories: **Type 1** are refractory metals that form mostly borides, e.g. V, Ti, Nb, Mo, Zr. These form precipitates and inhibit the grain growth during sintering [Herbst1991]. **Type 2** are low - melting metals which form eutectic compositions with the Nd - rich intergranular phase, e.g. Cu, Al, Ga, Sn. They improve the sintering behavior through increased wettability and were also shown to have a beneficial effect on the post - sinter annealing (PSA) parameters [Herbst1991]. Type 2 elements are only beneficial at the grain boundaries. A substitution of these elements for Fe in the $Nd_2Fe_{14}B$ needs to be avoided, since it will deteriorate its intrinsic magnetic properties. As already described in the previous chapter, **Type 3** are elements that substitute for either Nd or Fe in the $Nd_2Fe_{14}B$ - phase. They improve intrinsic parameters like anisotropy field H_a or Curie-temperature T_c. Most important here are other rare earths, e.g. Dy or Tb for Nd, and Co for Fe. The latter also greatly improves the corrosion resistance of the material by forming more noble Nd-Co intermetallic phases at the grain boundaries [de Groot1998].

B. Strip casting

The relatively slow cooling rates during conventional casting methods lead to a major problem: as seen in the phase diagram in Figure 2-6 the system passes through the „L + γ - Fe“ phase region during solidification and precipitates of γ - Fe (which transforms to α - Fe at RT) are formed, which remain in the solidified ingot. They are considered to be very harmful to the coercivity of the final magnet since the α - Fe is ferromagnetic at the working temperature of the magnet and hinders the magnetic decoupling of the grains. Also it poses as a nucleation site for the demagnetization. The amount of α - Fe in the ingot

can be reduced by a homogenization annealing after the casting. This process is costly and usually not all the α - Fe can be removed. Also large Nd - rich regions remain in the ingot, which are sensitive to oxidation. A way to overcome these problems is the so - called strip casting (SC) process. It is a rapid cooling technique similar to melt - spinning, albeit with lower copper wheel speeds. During SC the Nd-Fe-B is formed into platelike flakes. For example, Bernardi et al. report flakes with a thickness of 250 - 350 µm and a width of several cm for a wheel speed of 1 m/s [Bernardi1998]. The microstructure of the flakes consists of columns of ϕ - phase with a diameter of 5 - 60 µm and a length of several 100 µm. Through optimization of the composition of the melt and process parameters the width of the columns can be reduced to several µm, which is in the range of the final particle size after milling [Kaneko2004]. Within the large dendritic columns of the ϕ - phase a thin Nd - rich phase is formed parallel to the growth direction. The interlamellar spacing between the Nd - rich platelets is about 3 µm and is dependent on cooling rate and composition of the melt [Bernardi1998]. This optimized microstructure has several advantages over cast material: as mentioned, the fine distribution of Nd - rich phase hinders oxidation of large Nd - rich reservoirs and no harmful α - Fe is found in the material. Also, the fine distribution of Nd - rich phase leads to a very fine powder particle size after hydrogen decrepitation and an optimized distribution of Nd - rich grain boundary phase in the final magnets. The method enables a substantial reduction of RE content in the magnets and is industrial standard for some years now [Sugimoto2011].

C. Hydrogen decrepitation and desorption

As already mentioned, after the strip casting the flakes are subjected to the so - called „hydrogen decrepitation“ (HD) process, during which the material is exposed to hydrogen at slight overpressure in a reaction chamber [Harris1985]. The different phases pick up hydrogen and expand drastically. Decrepitation, i.e. the formation of micro - cracks, occurs due to the large difference in volume change during the hydrogen pickup: 4.8 vol.% for $Nd_2Fe_{14}B_1H_{2.7}$ [Oesterreicher1984] and 16.4 vol.% for NdH_3 [ICSD2014]. The temperature needed to start the decrepitation depends on the surplus of Nd: a near stoichiometric compound needs to be heated to about 150 °C [Harris1987], whereas a Nd - rich alloy like $Nd_{15}Fe_{79}B_6$ (at.%) decrepitates at room temperature in a few minutes. Because the hydrogen in the ϕ - phase reduces its H_a , it is desorbed again by a heat treatment in vacuum after the decrepitation [Oesterreicher1984]. The material is extremely brittle afterwards and can be milled easily.

D. Jet milling

It is generally known that a smaller grain size leads to an increased coercivity of Nd-Fe-B magnets, since smaller grains have a lower probability of critical surface defects and therefore show higher coercivities [Li2009, Uestuener2006]. However, smaller particles pick up more impurities, like oxygen, during the sintering process. This leads to a critical particle diameter d_{crit} below which the coercivity breaks down [Nothnagel1991]. This parameter is dependent on the composition of the magnet and the amount of impurities picked up during the sintering process. Furthermore, very fine grained powder is harder to align in a magnetic field. Considering all this, an industrially common value of the particle size is about 5 µm [Hilzinger2013]. However, there is a trend towards the production of magnets with ultra - fine grain sizes ≈1 µm [Goto2010].

After crushing, the coarse powder is fed into a jet mill (JM). Among the different forms the fluidized - bed jet mill with opposed jets is the most used type for permanent magnet material [Chamayou2007]. The powder is continuously fed into a milling vessel, where it is picked up by high velocity gas jets created by Laval nozzles operating at overpressures of up to 6 bar. The comminution is exclusively the result of interparticle collision in the gas jets. During the process the powder is not in contact with machine components, therefore no contamination occurs. A classifier integrated into the mill housing picks up particles with the desired size and feeds bigger particles back into the process. Compared to the conventional techniques, like ball or attritor milling, JM has some clear advantages. First, it is a fast process, i.e. reaching the same particle size takes shorter times compared to conventional milling techniques. Secondly, as already mentioned, it introduces very little contaminations into the powder because there are no particle - wall interactions and the milling media are inert gasses, e.g. N, Ar or He. The energy contained in the gas jet is governed by the speed of sound, which is inversely proportional to the square root of the molecular weight of the used gas. Thus, replacing nitrogen (molecular weight 28) with helium (atomic weight 4) results in about 2.5 times higher energy [Chamayou2007]. Consequently, the finest particles sizes nowadays are achieved with He JM. All the listed advantages led to the fact that JM is industry standard nowadays.

Jet milling of HD powder was tried already in 1989 by Mcguiness et al. [McGuiness1989]. The authors compared attritor milled and jet milled powder and found a more uniform particle size distribution for the latter, together with low impurity values. Hattori et al. [Hattori2009] investigated jet - milled powder from single crystalline (SC) Nd-Fe-B with particle sizes ranging from 1 - 5 µm. They show that if the milled particles become smaller than the distance between the Nd - rich lamellae of the SC alloy, they are less

likely to contain Nd - rich phase. This would lead to a worse distribution of Nd - rich phase in the final magnet which might be one reason for the decrease in coercivity as the grain size gets below a certain value.

E. Pressing and alignment

After milling, the fine powder is consolidated into a mechanically stable green body. A common value for the pressing pressure is 200 MPa. For achieving a high degree of texture, or a macroscopic easy axis, the particles need to be aligned with their crystallographic c - axes (easy axis of magnetization) in the same direction. This orientation is achieved by applying a magnetic field before or during the pressing. The smaller a particle is, the harder it is to align it due to particle - particle friction and the higher the required magnetic fields. For the production of anisotropic magnets there are a number of different processing routes, which determine the properties and the processing costs [Hilzinger2013]. In the following, the four mainly used pressing techniques are presented in detail:

During *die pressing* the powder is fed into the cavity of a die and compacted uniaxially. Accompanying the compaction a static magnetic field is either applied parallel (axial field pressing, AP) or perpendicular (transverse field pressing, TP) to the pressing direction. With AP a large variety of different geometries can be produced as net - shaped parts, e.g. for motor applications. As a drawback, the alignment of the powder particles is disturbed severely during the compaction. Therefore the remanence is about 8% lower compared to isostatically pressed magnets [Vacuumschmelze GmbH & Co KG2014]. During TP the alignment of the powder - particles is not disturbed so strongly, which results in remanences similar to isostatically pressed magnets. However, TP is inferior to AP from the viewpoint of net - shape manufacturing [Hilzinger2013], i.e. TP parts require some contour - grinding afterwards, hence the machining costs are increased. With TP it is also possible to press relatively large rectangular blocks. After sintering the blocks are machined into smaller magnets with the wanted net - shape geometries.

During *cold isostatic pressing* (CIP) big blocks of powder are sealed in a rubber mould and aligned in a magnetic field. The pressing pressure is mediated through a liquid medium and applied homogeneously from all directions. In the course of such pressing the particle alignment is not disturbed significantly. Therefore, it enables the possibility to only apply magnetic fields during the filling of the mould; during pressing no fields are needed. The fields can be pulsed and are therefore much higher than the stationary fields, which leads to a better alignment, even for smaller particles. A common value is 1.5 T for stationary fields and 6 - 8 T for pulsed fields [Hilzinger2013, Popov2015]. It has been found that so -

called „alternate“ pulsing leads to a further increase in particle alignment. Here, the field pulses are applied in the easy axis of the magnet, and each time the magnetic field direction is alternated by 180°. For sintered magnets compacted this way a maximum degree of texture of over 98% is achieved with a remanence of 1.52 T [Hilzinger2013]. Applying gradient pulsed magnetic fields to the mould leads to even higher values. Here the magnetic field strength decreases by 50% over the length of the mould. A maximum degree of texture of 99% is achieved with a remanence of 1.55 T [Kaneko2004]. Because of the relatively high costs and slow processing only large magnetic blocks are produced with CIP. The final parts manufactured from these blocks need a lot of machining and therefore the processing costs are higher.

The problem is overcome with *rubber isostatic pressing* (RIP). Here, particles are filled in a rubber mould which is placed in a die press [Sagawa2000]. The uniaxial pressure is converted to an isostatic pressure through the deformation of the rubber mould. This way, near net - shape parts with a very high degree of texture comparable to isostatic pressing can be produced, albeit much cheaper and in shorter times.

A relatively new way of compacting powder is the so - called *pressless process*, which is excluding the pressing step [Sagawa2008]. The technique relies on very fine powder with a particle size in the range of 1 µm, for which the sintering activity is high enough to be consolidated without pressure. The powder is place in a container with a lid and densities of about 3 g/cm^3 are realized [Popov2015]. Afterwards it is aligned in a pulsed field and finally placed in a sintering furnace. The process has several advantages: the omitted pressing step simplifies the technology, making it faster and cheaper. Without large size pressing equipment it is easier to keep the powder in a protective atmosphere during compaction, which decreases overall impurity levels. A disadvantage is the relatively high shrinkage rate during sintering, which makes net - shape forming difficult [Popov2015]. Also, the handling of the very fine powder is demanding and expensive.

F. Sintering

The oriented green body, produced with the pressing methods described above, is consolidated by liquid phase sintering. During this process the outer parts of the Nd-Fe-B grains melt and together with the Nd - rich phase form a liquid phase, which enables and accelerates the formation of a fully dense magnet. During the process it is crucial to work in an inert gas athmosphere to minimize the uptake of atmospheric impurities, e.g. O or N. The sintering atmosphere can be either vacuum or, if closed porosity is reached, an inert gas like Ar. The sintering temperature to achieve fully dense magnets depends on the

composition of the system, the powder particle size and the amount of impurities. It should be high enough to allow the formation of enough liquid Nd - rich phase to produce dense the magnets but low enough to prevent (abnormal) grain growth. Both effects, low density and grain growth, will lead to a decrease in coercivity. Therefore, depending on the composition an optimal sintering temperature exists where the coercivity is highest. The finer the powder and the lower the impurity contents, the higher the sintering activity and therefore the lower the required optimal sintering temperature. Furthermore, finer powders show a higher tendency for abnormal grain growth compared to coarser powders when the sintering temperature is too high [Uestuener2006]. If the sintering conditions are optimal, the grain size in the final magnets is roughly double the initial powder particle size [Uestuener2006].

There are only a few publications on sintered Nd-Fe-B disclosing the used sintering temperatures, which makes it difficult to determine a precise particle size - temperature dependence. However, in Figure 2-7 four publications were evaluated and a rough linear dependence could be found. The upper and lower boundaries are 7.3 µm / 1040 °C [Uestuener2006] and 1.3 µm / 920 °C [Sasaki2015], respectively. The spread is due to different impurity contents and compositions of the samples.

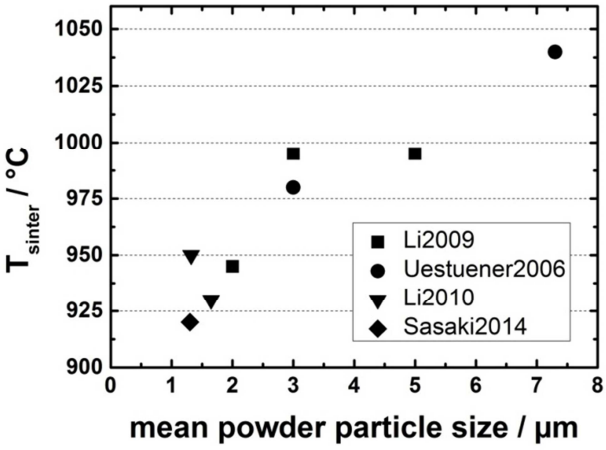

Figure 2-7: Dependence of sintering temperature on the mean particle size of sintered Nd-Fe-B permanent magnets.

G. Post - sinter annealing (PSA)

It has been known since the invention of Nd-Fe-B magnets that a post - sinter annealing (PSA) at relatively low temperatures leads to a tremendous increase in coercivity. For example, in the original work by Sagawa et al. a sintered $Nd_{15}Fe_{77}B_8$ magnet showed optimal properties after annealing at 610 °C [Sagawa1984]. The PSA temperatures vary strongly with the composition of the magnets and can be as

low as 480 °C [Yan2006]. Especially the addition of Cu decreases the PSA temperature. Also two - stage PSA are possible to finetune the magnetic properties, e.g. 800 °C followed by 500 °C [Shinba2005]. The most prominent findings and theories regarding the mechanism of the PSA are presented in the following.

Schneider et al. suggested the presence of a metastable, magnetically soft phase with a T_c of 245 °C in sintered magnets, which may increase internal demagnetizing fields or reduce intergranular coupling [Schneider1990]. This phase is dissolved during the PSA at 600 °C and consequently H_c increases. Among many others before Shinba et al. suggested that PSA at temperatures above the Nd-Fe-B eutectic temperature of 665 °C leads to the formation of a small amount of liquid phase and in turn to a uniform distribution of Nd - rich phase around each grain forming a nm - thick grain boundary phase [Shinba2005]. A second PSA step at 500 °C, below said eutectic point, smoothes the grain boundaries of the $Nd_2Fe_{14}B$ grains. This decreases the defect density and therefore the probability of nucleation of reversal domains. Kim et al. investigated Nd - rich triple junction points and grain boundaries and found a change of crystal structure from a hexagonal to a cubic Nd_2O_3 phase after PSA [Kim2012]. They calculated a reduced lattice misfit to the $Nd_2Fe_{14}B$ phase and therefore a reduced mechanical stress at the interface. With STEM EDX they found a significant amount of Cu segregated at the grain boundaries after PSA and speculate that this could stabilize the different crystal structure. The Cu segregation was confirmed by Sepehri-Amin et al. by means of 3 - dimensional atom probe tomography [Sepehri-Amin2012]. The interfaces of Nd and Nd - oxide with different crystal structures have been investigated by STEM and modelled on the atomistic scale by Hrkac et al. [Hrkac2014]. It was shown that the different crystal structures lead to different lattice distortions and therefore different coercivities. Woodcock et al. compared PSA in Dy - free, Dy - containing and low Cu - containing samples [Woodcock, Bittner, 2014]. They found the coercivity increase to be fully reversible for at least 3 times by annealing the magnet at the sintering temperature of 1050 °C (low coercivity state) and subsequently repeating the PSA at 500 °C on the same magnet (high coercivity state). The PSA effect was completed after only 5 min, ruling out all theories based on long - range diffusion, like e.g. Kim et al. suggested [Kim2012]. Finally, the PSA was also successful in the samples with low amount of Cu, ruling out the necessity of a low melting Nd-Cu eutectic phase. From these findings they propose a rather simple mechanism, that during PSA a low melting Nd - rich phase penetrates the gaps between the $Nd_2Fe_{14}B$ grains through capillary forces, which leads to an optimum distribution. During the resetting the magnet is annealed above the eutectic point of 660 °C in the Nd-Fe-B system, leading to the partial melting of the $Nd_2Fe_{14}B$ grains. Upon rapid cooling the melt quickly crystallizes on the grains. Where the grains converge the liquid Nd - rich phase is driven

out of the grain boundaries and into the triple points. This leads to grain boundaries without Nd - rich phase, i.e. non - decoupled $Nd_2Fe_{14}B$ grains.
All in all, the variety of results and theories shows that although the PSA has been studied extensively in the past, the reasons for the H_c increase are not completely understood yet.

H. Coating

Neodymium belongs to the ignoble metals with a strong negative electrochemical standard potential of E_0 = -2.2 to -2.5 V. On air it slowly reacts with oxygen and water vapor under the formation of hydroxides and hydrides. Therefore, Nd-Fe-B magnets have to be protected by alloying with suitable elements, e.g. Co and, if necessary, by a surface coating [Vacuumschmelze GmbH & Co KG2014]. The type and thickness of the coating depends on the environmental conditions during application. The most used coatings are metallic (e.g. Ni, Sn, Ni-Sn, Al) or organic (epoxy resins) [Vacuumschmelze GmbH & Co KG2014]. The latter are cost efficient and offer a high corrosion resistance while the former offer a better mechanical stability. The minimum required film thickness ranges from 5 µm for Al, 10 µm for epoxy resin to 15 µm for Sn. The maximum application temperature of the coated magnets lies in the range of 160 °C to 200 °C.

2.2. The GBDP

2.2.1. Theory of diffusion in polycrystals

In the following the diffusion in polycrystalline materials is described, based on the textbook “Diffusion in Solids” by H. Mehrer [Mehrer2007]. The thermodynamic basics of diffusion and the derivation of Fick’s laws can be found in numerous other textbooks and is not included here.

In contrast to single crystals, polycrystalline materials exhibit grain boundaries, which pose as high diffusivity paths. In metals the diffusion along these paths is typically four to six orders of magnitude faster than lattice diffusion [Mehrer2007]. Figure 2-8 shows a schematic of the different diffusion coefficients in metals and their relative magnitude.

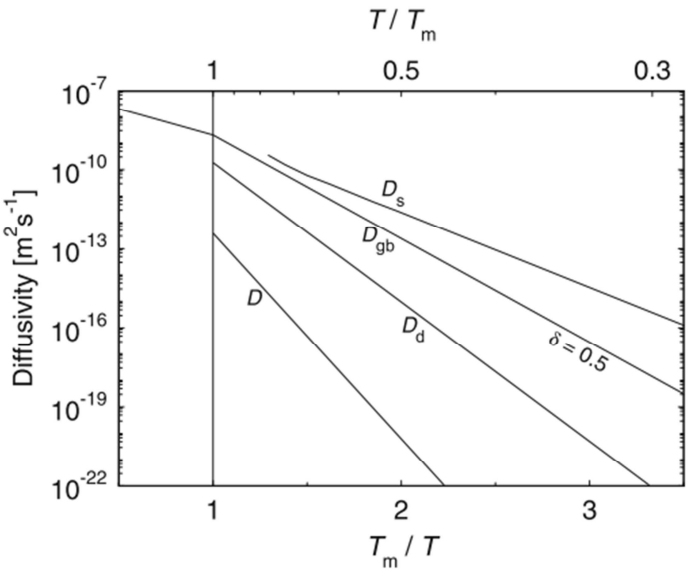

Figure 2-8: Schematic depiction of different diffusivities in metals depending on the reduced temperature. D … bulk diffusion coefficient, D_d … dislocation pipe diffusivity D_{gb} … grain boundary diffusion coefficient, D_s … surface diffusion coefficient, T_m … melting temperature [Mehrer2007].

Most of the mathematical treatment of grain boundary diffusion is based on the so - called Fisher model [Fisher1951]. It quantifies the coupled diffusion in a crystal and over its grain boundaries and was derived for a bicrystal. Here, the grain boundary is described by two parameters: the grain boundary width δ and the grain boundary diffusion coefficient D_{gb}. In the model, three simultaneous processes occur: direct diffusion from the source into the lattice, diffusion from the source along the grain boundaries and diffusion from the grain boundaries into the lattice. Depending on the importance and speed of each process three different kinetic regimes can be observed. Each regime is dominant under certain conditions, depending e.g. on annealing temperatures and times, grain sizes as well as lattice and grain boundary parameters. Figure 2-9 shows a schematic of the different kinetic regimes, classified after *Harrison* [Harrison1961]. While more sophisticated classifications are proposed, it is still the most widely used for polycrystals. In the following the different types are described in more detail.

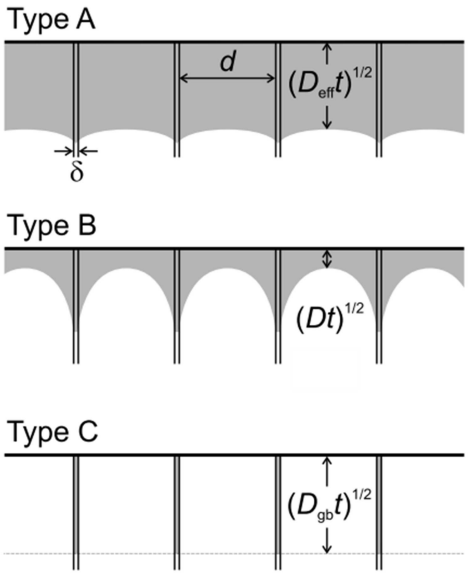

Figure 2-9: Classification of diffusion kinetics in polycrystals [Harrison1961].

Type A

This regime is dominant when the lattice diffusion length $\sqrt{Dt}$ is in the order of the grain size d:

$$\sqrt{Dt} \geq \frac{d}{0.8} \qquad \textbf{2-9}$$

It is characterized by an almost linear diffusion front where the diffusing species has penetrated deep into the grains of the core material. It is observed after annealings at high temperatures and with long annealing times as well as in materials with small grain size. Macroscopically, the concentration of the diffusing element obeys Fick's law for a homogeneous medium with an effective diffusion coefficient D_{eff} being the weighted average of the lattice and the grain boundary diffusivity [Mehrer2007]:

$$D_{eff} = gD_{gb} + (1-g)D \qquad \textbf{2-10}$$

Here g is the volumetric ratio of grain boundaries to bulk material. Since $D_{gb} \gg D$ D_{eff} will always be larger than D. The one - dimensional concentration profile c(x,t) in diffusion direction follows either a Gaussian function:

$$c(x,t) = c_{surf} - \left(c_{surf} - c_{bulk}\right) \cdot exp\left(-\frac{x^2}{\sqrt{4D_{eff}t}}\right) \quad \textbf{2-11}$$

for an instantaneous source or an error function for a constant source:

$$c(x,t) = c_{surf} - \left(c_{surf} - c_{bulk}\right) \cdot erf\left(\frac{x}{\sqrt{4D_{eff}t}}\right) \quad \textbf{2-12}$$

where c_{surf} and c_{bulk} are the surface and bulk concentrations and D_{eff} is the effective diffusion coefficient.

Type B

For a type B diffusion kinetic the lattice diffusion length $\sqrt{Dt}$ must be between the grain boundary width and the grain size:

$$s\delta \ll \sqrt{Dt} \ll d \quad \textbf{2-13}$$

Where s is the segregation factor, which describes the segregation of foreign atoms in the grain boundaries. s > 1 for enrichment and s < 1 for depletion of foreign atoms. Type B kinetics emerge after annealings at intermediate temperatures or short annealing times of materials with sufficiently large grain sizes. In this diffusion regime, grain boundary fringes develop through out - diffusion from the grain boundaries. The concentration profile of the diffusing species consists of two parts: a near - surface part formed by lattice diffusion from the surface, which extends to about 3-4 $\sqrt{Dt}$ and where the profile follows either a Gaussian or an error function, depending on the type of source. And a so - called grain boundary tail (GBT) region, which is formed through the coupled grain boundary diffusion and out - diffusion from the grain boundaries. The concentration profile in the GBT follows a linear relationship between log(c(x)) and $x^{6/5}$, as illustrated in Figure 2-10. The exponent 6/5 has no physical meaning and cannot be derived analytically, it simply delivers reasonably good fit results.

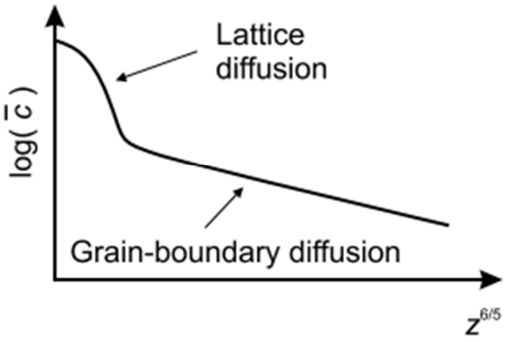

Figure 2-10: Concentration profile for a type B diffusion kinetic.

Only the triple product $s\delta D_{gb}$ can be determined from type B diffusion experiments via the formula

$$s\delta D_{gb} = a\sqrt{\frac{D}{t}}\left(\frac{\partial c}{\partial z^{\frac{6}{5}}}\right)^{-5/3} \qquad \textbf{2-14}$$

where *a* is a constant depending on the type of source.

Type C

For type C diffusion kinetics the lattice diffusion length must be significantly smaller than the grain boundary width:

$$\sqrt{Dt} \ll s\delta \qquad \textbf{2-15}$$

In this regime pure grain boundary diffusion is dominant without significant leakage into the grains. As in type A kinetics the concentration profiles follow either a Gaussian or an error function for instantaneous or constant sources, respectively. Different from type B, D_{gb} does not stand in a triple product and can therefore be directly determined from data fits.

2.2.2. The grain boundary diffusion process in Nd-Fe-B magnets

As described in chapter 2.1.2, the demagnetization behavior in Nd-Fe-B based permanent magnets is dominated by nucleation of reversed domains at the grain surfaces. There, the magnetocrystalline anisotropy is reduced due to lattice distortion and atomic defects [Hrkac2014]. Among elements like Cu, Al or Ga, conventionally heavy rare earths (HRE) are added to the pre - alloy prior to the sintering process in order to increase the magnetocrystalline anisotropy field of the matrix phase and increase coercivity [Gutfleisch2011]. As a disadvantage, the HRE in the center of the grains is not as effective, since it does not contribute to the magnetic hardening of the grain surface. Moreover, the addition of HRE decreases the saturation magnetization of the ϕ - phase [Herbst1991]. An alternative way to introduce HRE into Nd-Fe-B magnets was found already in 2000 by Park et al. [Park2000]. They covered a Nd-Fe-B sintered magnet with a thin Dy layer and applied intermediate temperatures of 800 °C. The samples showed a remarkable increase in coercivity, which was attributed to the substitution of Nd by Dy atoms in the $Nd_2Fe_{14}B$ structure. The Dy diffused over the grain boundaries into the magnet and after cooling was incorporated in the immediate surrounding volume of the grain boundaries. This process was termed *Grain Boundary Diffusion Process* (GBDP). It selectively deposits HRE only in the vicinity of the grain boundaries and eliminates the detrimental effects of HRE in the grain centers. As a consequence, significantly less HRE are needed to achieve desired coercivities, and simultaneously the remanence remains almost unchanged through the diffusion treatment. The GBDP was studied extensively in the ensuing years. There are numerous studies with other heavy rare earth (HRE) compounds as diffusion medium to increase coercivity, such as Tb [Samardzija2012], Dy - and Tb - fluorides [Komuro2010, Nakamura2011] and eutectic compositions like DyNiAl [Oono2011], which found that the diffusion occurs mainly over the grain boundaries and leads to a microstructure with grains exhibiting a HRE - rich $(Nd,RE)_2Fe_{14}B$ shell and a HRE - poor core [Samardzija2012, Sepehri-Amin, Ohkubo and Hono2013]. Also the HRE diffusion in hot deformed Nd-Fe-B magnets has received a lot of attention in the last years [Sawatzki2014, Sepehri-Amin, Ohkubo, Nagashima, 2013, Watanabe2013]. The precise determination of the HRE element distribution in Nd-Fe-B sintered magnets after a GBDP is crucial for the optimization of overall magnetic properties and the geometric design of final magnets. The topic has been addressed in recent publications. Samardžija et al. used Tb as diffusing HRE and found a linearly decreasing Tb concentration up to a diffusion length of 200 µm [Samardzija2012]. Sepehri-Amin et al. have investigated the Dy concentration in Nd-Fe-B magnets after a GBDP using 3 - dimensional atom probe (3DAP) tomography. They investigated a spot 2.7 mm away from the surface and found a

significantly enhanced Dy concentration near the grain boundaries [Sepehri-Amin, Ohkubo and Hono2013].

As a difference to the presented diffusion theory, a liquid phase is present in Nd-Fe-B magnets above 600 - 700 °C, depending on the total composition (Figure 2-6) [Malfliet2008]. The liquid phase surrounds the grains as a thin layer and enables an even faster diffusion compared to conventional grain boundary diffusion (Figure 2-8). If one assumes a linear relation between the Dy concentration difference $\Delta c(Dy)$ and the coercivity change ΔH_c equation 2-12 becomes

$$\Delta \mathrm{H_c}(\mathrm{x},\mathrm{t}) = \Delta \mathrm{H_{c,surf}} - \left(\Delta \mathrm{H_{c,surf}} - \Delta \mathrm{H_{c,bulk}}\right) \cdot \mathrm{erf}\left(\frac{\mathrm{x}}{\sqrt{4\mathrm{D_{Dy}t}}}\right) \qquad \textbf{2-16}$$

2.3. Production of (Nd,Dy)-Fe-B via powder blending

In industrial practice it is common to produce sintered Nd-Fe-B magnets by blending two or more powders with different compositions in order to even out compositional fluctuations of the pre - alloys. After the sintering process, which usually takes several hours, the chemical differences in the powders are completely or nearly completely evened out, resulting in grains consisting of homogeneous ϕ - phase.

However, it has been found that under certain conditions of the sintering process the blending leads to the formation of a chemically inhomogeneous ϕ - phase, similar to the core - shell structures developed in the surface region of GBDP magnets. This is reasoned to be a favorable microstructure that enhances the coercivity, because it magnetically hardens only the grain surface. In the following the working principle and terminology of the blending process is introduced (Figure 2-11). The “Base Powder” (BP) is made of a conventional Nd-Fe-B magnet composition, generally with relatively low amounts of additives, especially HRE. The BP is mixed with an “Anisotropy Powder” (AP), which is a HRE - rich compound with the aim of selectively introducing the HRE into the magnet. Ideally, the AP particles should completely melt during sintering, in contrast to the BP particles, which should not melt. This way a HRE - rich liquid phase is created that, after solidification, surrounds the BP grains and forms a core - shell microstructure. However, in real materials surface of the BP particles also melts to a certain extent.

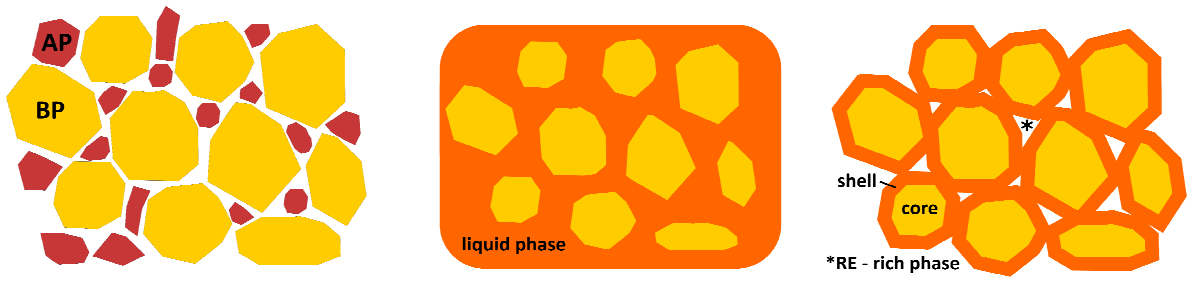

Figure 2-11: Schematic of the Nd-Fe-B sintered magnet production via powder blending. (left) mixed base powder (BP) and anisotropy powder (AP). (middle) during sintering a liquid phase is created rich with the elements from the AP. (right) After solidification a core - shell microstructure is created.

So far the powder blending process has been investigated for a variety of Dy - rich AP. The most important ones are: Pure Dy in form of DyH_x [Yan2010], Dy_2O_3 [Ghandehari1986], $(Nd,Dy)_3Co_x$ [Velicescu1995], DyGa [de Groot1998], DyF_3 [Xu2011] and Dy_2S_3 [Gabay2011]. For all compounds a faint heterogeneous (Nd,Dy)-Fe-B ϕ - phase is found, with an increased Dy content in the outer regions of the grain and a more or less Dy - free grain core. However, the experimental evidence in form of micrographs is often of poor quality owing to the very minor compositional difference of the core and shell regions. All the listed examples suffer from high to very high required sintering temperatures and / or very long sintering times. This leads to grain growth (up to >50 µm [Yan2010]) with a detrimental effect on coercivity. Also, the higher the sintering temperature, the more liquid phase is formed during sintering which reduces the overall Dy content in the shells. The reason for the increased sintering temperature are the usually very high melting points of the used Dy compounds or the compounds formed during sintering (e.g.: $T_m(Dy)$ > 1400 °C; $T_m(DyFe_x)$ > 1250 °C; $T_m(Dy_2O_3)$ > 2400 °C; $T_m(DyF_3)$ > 1360 °C; $T_m(Dy_2S_3)$ > 1400 °C). The introduction of the elements F, S or O in the microstructure leads to the formation of Nd-X compounds that are essentially undesired, paramagnetic “ballast” and reduce the magnetization. Also these compounds potentially decrease the corrosion resistance of the magnets [Herbst1991]. For Dy_2O_3 it was found that only a fraction of the Dy atoms separate from the oxygen and are introduced into the ϕ - phase [Doser1988]. Another problem of the addition of pure Dy or DyH_x compounds is, that it shifts the overall composition of the magnet to higher RE contents, which lowers the remanence. To produce sintered magnets with “modern” compositions (RE content ≤ 14.5 at.%) one therefore needs to start with an almost ternary Nd-Fe-B as Base Powder and add the Dy compound. It is problematic to sinter compositions with such low RE content because only a small amount of liquid phase will form during sintering.

3. Sample preparation and experimental methods

The first part of the following chapter describes the commercial sintered magnets and the experimental setup used in the diffusion experiments in chapter 4. Afterwards, the production process of Nd-Fe-B magnets, developed for the powder blending studies in chapter 5, is explained in detail. The second part of the chapter gives a brief overview of the employed magnetic characterization techniques.

3.1. Sample preparation

3.1.1. Commercial sintered magnets for diffusion experiments

For the studies concerning the GBDP commercial sintered magnets were provided by Vacuumschmelze GmbH & Co. KG. Two magnet grades were chosen: grade 1 is nearly Dy - free ("VD722") and grade 2 contains about 1 at.% / 2.6 wt.% of Dy ("VD837"). The exact compositions and the approximate impurity concentrations can be found in Table 3-1.

Table 3-1: Composition and impurity concentrations of sample magnets, data provided by Vacuumschmelze GmbH & Co. KG (all values in wt.%).

	Nd	Dy	Tb	B	Fe	Co	Cu	C	O	N
grade 1	29.2	0.5	0.3	1.0	bal	2.0	traces	0.052	0.15	0.013
grade 2	29.0	2.6	-	1.0	bal	1.0	0.1	0.052	0.15	0.013

Figure 3-1 shows the typical demagnetization curves for both magnet grades, together with H_c and M_r.

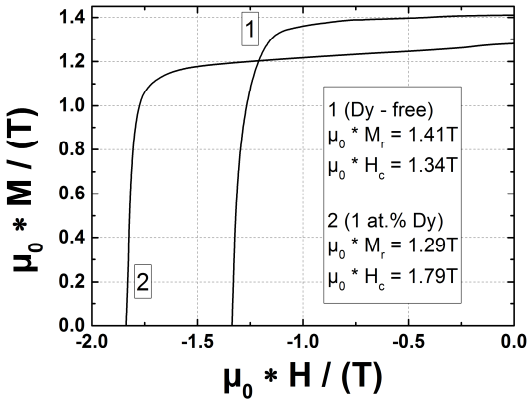

Figure 3-1: Demagnetization curves of the two commercial sintered magnet grades used in the GBDP experiments. grade 1 is nearly Dy - free and grade 2 contains about 1 at.% / 2.6 wt.% of Dy.

For the diffusion experiments in chapter 4.1 samples of grade 1 with a size of 10 x 10 x 3 mm were used. A slurry of Dy powder in alcohol was either applied to one lateral surface with the dimensions of 10 mm x 3 mm or to both pole surfaces with the dimensions of 10 x 10 mm. The total amount of applied Dy was about 0.6 wt.% of the magnets. The coated samples were individually wrapped in Molybdenum foil and annealed at elevated temperatures T_a ranging from 600 °C ≤ T_a ≤ 1050 °C for 6 h followed by a low temperature annealing around 500 °C for 2 h.

The samples for most experiments in chapter 4.2 were grade 2. For comparison, the Dy diffusion was also investigated in grade 1. The sample geometry for the diffusion experiments was 8 (length) x 5 (width) x 5 (depth) mm. The RE source material for the diffusion treatment are Dy, Tb, Gd and Ce thin film foils (Alfa Aesar) with 99,9% purity and a thickness of 25 µm, which were attached to the magnets. A force was applied with a clamp to hold the samples together. The diffusion occurred along the length side, i.e. always with an 8 mm distance. The samples were protected with Molybdenum foil and the diffusion heat treatment was conducted in protective Argon atmosphere. It consisted of a step at 900 °C with varied length and a post-sinter annealing (PSA) step at 500 °C for 2 h. A schematic of the experimental setup is shown in Figure 3-2. After the treatment the magnets were cut into slices of about 500 µm thickness using a wire saw.

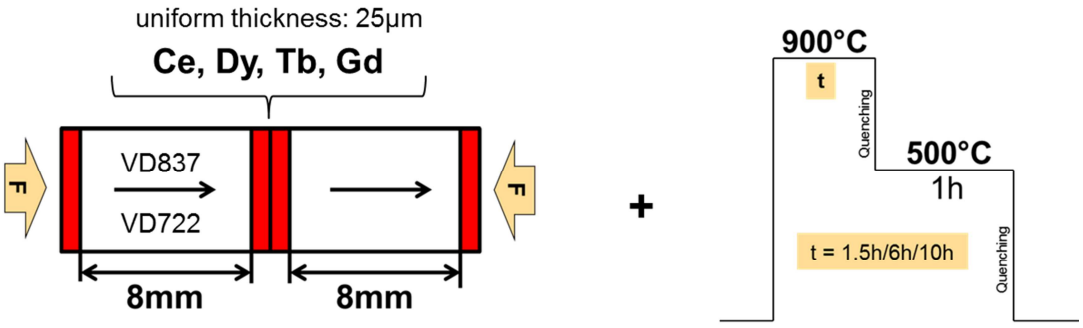

Figure 3-2: Schematic setup for diffusion experiments with RE thin foils (left) and heat treatment regime of the samples (right).

3.1.2. Laboratory production process for ternary Nd-Fe-B sintered magnets

A process route to produce sintered Nd-Fe-B magnets has been established on the laboratory scale. In terms of coercivity the obtained magnets can be qualitatively compared to industrial ones. the remanence, however, is slightly lower due to the used transversal pressing. In contrast to commercial magnets none of the usual secondary elements (e.g. Cu, Ga, Al, Co) or other RE (Pr) are added in order to exclude all possible influences of said elements and focus solely on the reactions in the ternary system. In the following the production steps are described in detail. The numbering from A - G follows chapter 2.1.3 on the production of commercial sintered Nd-Fe-B magnets.

As differences, the pre-alloy is not strip-casted, but cast and solidified in an induction melter. To eliminate remaining α - Fe in the microstructure the obtained ingots are homogenized in a furnace (step B). The material is milled in a planetary ball and not a jet mill (step B), and no coating is applied to the final magnets (step H).

A. Production of the Nd-Fe-B pre - alloy

The composition of the pre - alloy was optimized over the course of 10 different sample batches, with the aim of reducing the Nd and B content as much as possible. The experiments started from $Nd_{16}Fe_{76}B_8$ (at.%) and ended at $Nd_{15}Fe_{79}B_6$ (at.%) or $Nd_{32.58}Fe_{66.45}B_{0.98}$ (wt.%). In Figure 3-3 a detailed section of the ternary Nd-Fe-B phase diagram is given, in which the compositions of the different batches are marked. The final composition was chosen because it proved to be the optimum between high remanence and ease of production. It lies in the "ϕ + L" phase region, where there are no harmful soft magnetic phases

present. The surplus of Nd is about 8 wt.%, which leaves plenty for the formation of the Nd - rich phases (and Nd containing impurity phases and borides) to ensure a good magnetic decoupling of the individual grains. Compared to commercial magnets the composition is rather Nd - rich. This surplus is needed for two reasons, which will be discussed in detail later: a) The pre - alloy is produced by induction melting. Compared to strip casting this leads to a worse distribution of Nd with no fine lamellae, making HD less effective. b) The powder is produced by ball milling in heptane. This introduces a lot more impurities, as compared to jet milling. As a result of the higher Nd content the remanence is reduced by about 5% compared to commercial magnets.

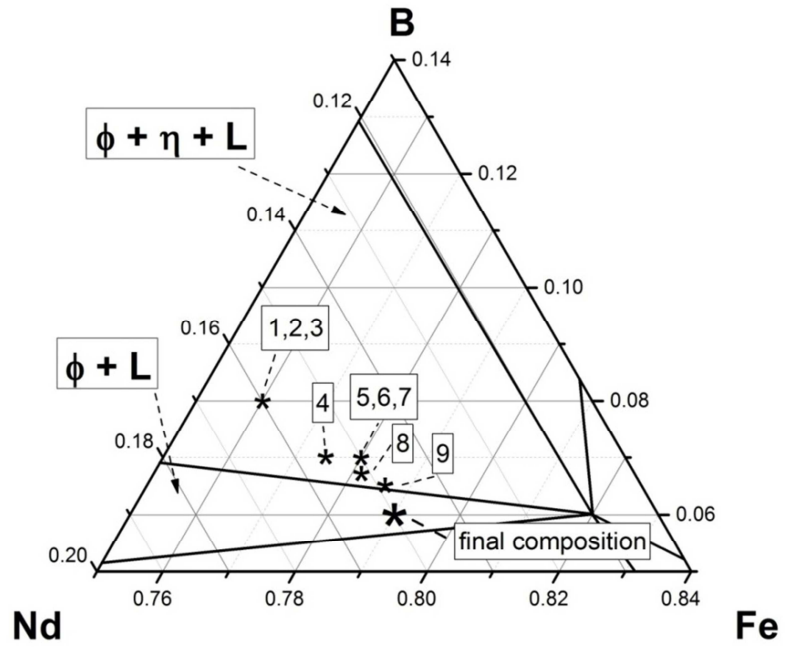

Figure 3-3: Detailed section of the phase diagram in Figure 2-5 at 1000 °C [Malfliet2008]. The compositions of the different sample batches 1 - 10 are marked with *.

The pre - alloy ingot was molten inductively in Zirconium oxide crucibles with the following raw materials: Fe (99.9% pure, Chempur), Fe_1B_1 (produced inductively from Fe and B [99% pure, Chempur]) and Nd (99.9% pure, Chempur). The total mass of each ingot was about 25 g, which is enough for 3 - 4 magnets. After melting, the ingot contained mainly the $Nd_2Fe_{14}B$ phase and secondary phases of Nd and α - Fe, as was determined by EDX (Figure 3-4, left). In order to enable the slow peritectic forming reaction of the $Nd_2Fe_{14}B$ phase under the consumption of Fe and Nd the ingot was homogenized at 1120 °C for 2 days. The obtained microstructure contains no more α - Fe (Figure 3-4, right).

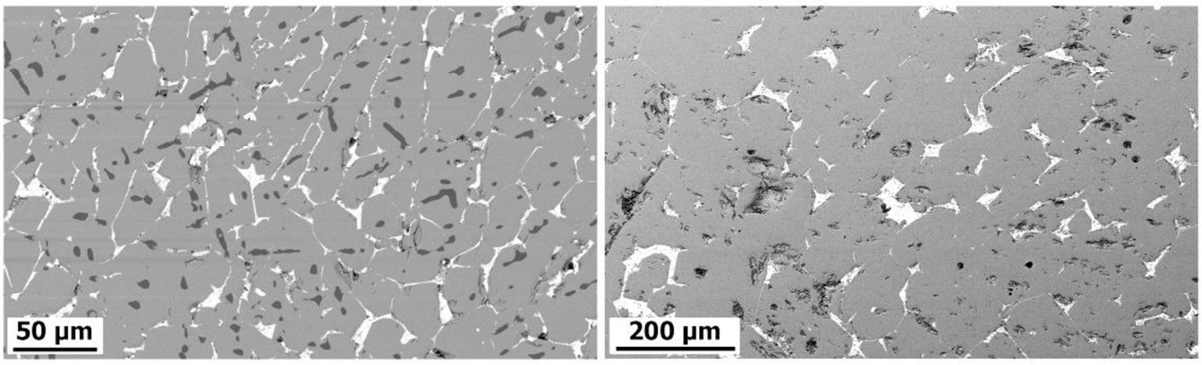

Figure 3-4: $Nd_{15}Fe_{79}B_6$ pre - alloy after induction melting (left) and homogenization at 1120 °C for 48 h (right). The grey main phase is $Nd_2Fe_{14}B$, in white is the Nd - rich phase and in dark grey is α - Fe.

C/D. Hydrogen decrepitation and milling

After the homogenization the ingots were hydrogen decrepitated under 1 bar hydrogen at room temperature, followed by crushing under protective atmosphere in a mortar and sieving to particle sizes <160 µm. The powder is then milled in a planetary ball mill (Fritsch *Pulverisette 6*) at 350 rpm. The ball:powder ratio is kept at 10:1 by weight. The described parameters were determined in previous unpublished works by Konstantin Skokov and kept constant for all experiments, since an elaborate optimization of the milling process is outside the scope of this thesis. The powder is wet - milled in heptane (p.a., Chempur) for the following reasons: First, to an extent the heptane film protects the particles from reactions with the atmosphere. This is an important point, since even a short exposure to air would cause a rapid oxidation of the material and therefore make sintering impossible. Secondly, due to reduced particle - particle friction the orientability of the powder in the matrix is increased. Lastly, with wet powder a higher and more homogeneous density of the green body can be achieved during pressing [Schatt2007]. As a drawback, wet milling in hydrocarbons is more likely to introduce impurities like C or O (soluted in the solvent) into the powder [Suryanarayana2001].

Particle size distributions of Nd-Fe-B powder after different milling times up to 60 min are shown in Figure 3-5. The mean particle diameter d_{50} decreases from 8.16 µm after 15 min to 4.98 µm after 60 min.

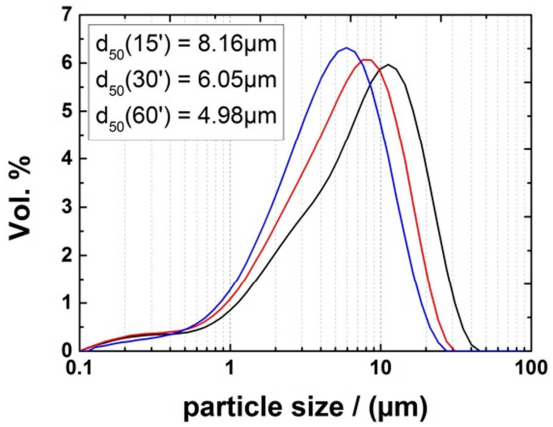

Figure 3-5: Particle size distributions in dependence of ball milling time for 25 g of Nd-Fe-B milled at 350 rpm. *The particle size analysis was conducted by J. Gassmann at the Fraunhofer IWKS, Hanau.*

Figure 3-6 shows the coercivity of sample magnets in dependence of the milling time. A maximum was observed for a 30 min milling and subsequently chosen as standard milling time. It provides the optimum between small grain size (increasing coercivity) and high impurity levels (decreasing coercivity).

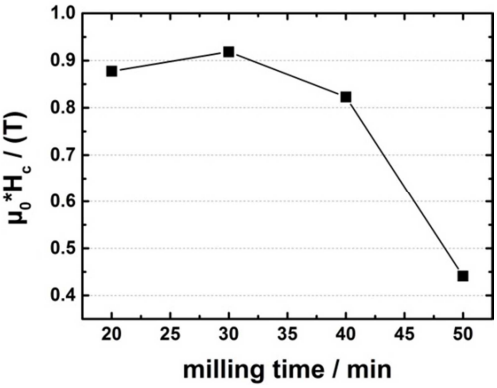

Figure 3-6: Coercivity of magnets with the nominal composition of $Nd_{15.5}Fe_{77.5}B_7$ in dependence of milling time. The magnets were in the as - sintered state and did not receive a PSA treatment, hence the rather low coercivity.

E. Pressing and alignment

After milling the wet powder is extracted from the milling vial under protective N_2 atmosphere in a custom built glove box, filled in a pressform with a base area of 15 x 10 mm and sealed in a plastic bag. It is then transversally pressed (TP) in a magnetic field of approximately 1.7 T with a small pressure of 10 MPa. This low pressure is needed to maintain a high degree of alignment of the powder particles. In the

final magnets after sintering a DOT of about 94% is achieved. This relatively low value is caused by the fact that the powder is still hydrogenated before pressing. Only during sintering the hydrogen is released and further purifies the atmosphere. As a disadvantage, the hydrogen reduces H_a of the Nd-Fe-B particles and therefore the orientability. Finally, the green bodies are cooled with liquid nitrogen before the transfer into the sintering furnace. This provides not only a protective atmosphere but also impedes oxidation.

F. Sintering

During sintering the green bodies are surrounded with coarse grained Nd-Fe-B-H_x powder ("getter powder") as an oxidation barrier and are confined in a box made from Mo foil. The whole setup sits in a quartz glass tube, which is evacuated under constant pumping with a turbomolecular pump to about 10^{-5} mbar (Figure 3-7). Through optimization of pre - alloy production and process parameters the sintering temperature was lowered from 1080 °C to 1050 °C for the final $Nd_{15}Fe_{79}B_6$ magnets.

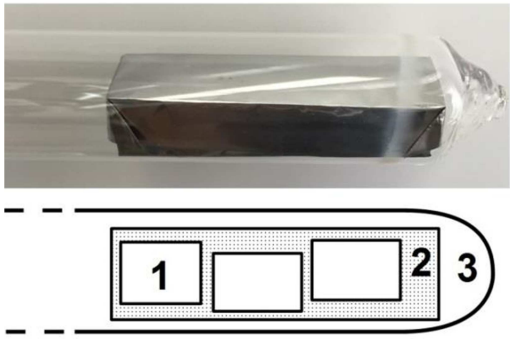

Figure 3-7: Photo and schematic of the sintering setup. The Nd-Fe-B green bodies (1) sit in a box made from Mo foil filled with coarse grained Nd-Fe-B getter powder (2). The box is kept under high vacuum in a quartz glass tube (3).

G. Post - sinter annealing

The post - sinter annealing (PSA) consists of two temperature steps. The first step was optimized for $Nd_{15}Fe_{79}B_6$ and kept for $(Nd_{0.9}Dy_{0.1})_{15}Fe_{79}B_6$ (Figure 3-8). The second step is more important and was optimized for both investigated compositions. The optima for both compositions are 750 °C and 510 °C, respectively.

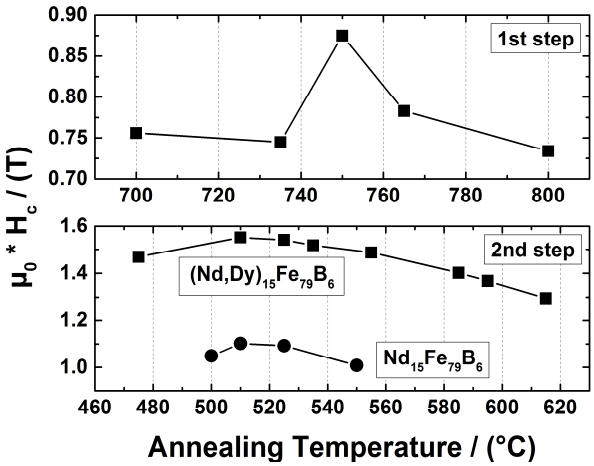

Figure 3-8: Coercivity vs. annealing temperature after post - sinter annealing (PSA) of Nd-Fe-B and (Nd,Dy)-Fe-B magnets. The optimum PSA steps for both magnets are 750 °C followed by 510 °C.

3.2. Experimental methods

In the following an overview of the used magnetic measurement methods is given. The employed characterization methods for microstructure (SEM, TEM), crystal structure (XRD), particle size (Laser Diffraction), thermodynamic properties (DSC) and chemical composition (ICP - OES) are described in the literature and are not repeated here. The overview is based on the textbooks of Fiorillo [Fiorillo2004] and Coey [Coey2010], as well as technical data sheets of the device manufacturers. After a short introduction, first the fluxmetric methods (HCS, VSM, pulsed field magnetometer, hysteresis graph), then the Hall probe and the Kerr microscope are presented. Finally, a short description of the singular point detection (SPD) method is given.

The basic principle behind fluxmetric methods is described by Faraday's law, which states that a voltage U(t) [V] is induced in a coil exposed to a time - variant magnet flux Φ [Vs]:

$$U(t) = -\frac{d\Phi}{dt} * N \qquad \textbf{3-1}$$

where N is the number of coil windings. Integrating over the electric voltage and normalizing over *N* and the area *A* of the coil yields the magnetic flux density B [Vs/m^2 = T]:

$$B = -\frac{1}{A * N}\int_{t1}^{t2} U(t)\, dt \qquad \textbf{3-2}$$

where t denotes the time. The here presented techniques can be classified as closed or open circuit measurements, depending on whether the sample is a part of a complete magnetic circuit or not. Open circuit measurements are generally easier and less demanding on sample shape, but suffer from the inconvenience that the internal field H_i sensed by the sample is the applied external field H_{ext} reduced by the geometry dependent demagnetizing field:

$$H_i = H_{ext} - \mathcal{N} * M \qquad \textbf{3-3}$$

with $\mathcal{N}$ being the demagnetization factor, ranging from 0 to 1. Therefore, a field correction must be undertaken to obtain H_i for which the sample shape has to be known. In closed circuit measurements the demagnetizing field is zero and $H_i = H_{ext}$. Compared to closed circuit conditions, the measurement in an open circuit tends to decrease the so - called rectangularity of the demagnetization curve, i.e. the magnetization reversal is happening over a greater field range (Figure 3-9). The reason for this measurement artifact are inhomogeneous demagnetizing fields at the edges of samples, which can locally by far exceed the average value expressed by the demagnetizing factor $\mathcal{N}$. In the M-H diagrams of this work, H always denotes H_i, unless otherwise specified.

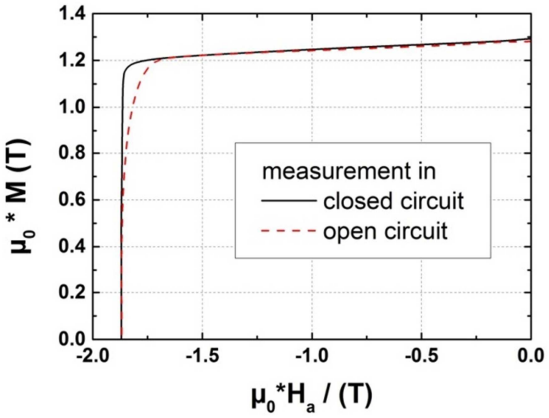

Figure 3-9: Comparison of hysteresis curves of (Nd,Dy)-Fe-B magnets measured in closed and open circuit conditions. The measurements have been conducted with the same sample in a hysteresis graph and an pulsed field magnetometer, respectively.

In the following the different methods are described in more detail.

3.2.1. Helmholtz coil setup

A Helmholtz coil setup (HCS) consists of two identical circular coils placed coaxially and separated by a distance equal to the radius of the coils. The described geometry results in a very low variation of measurement sensitivity in a defined volume inside the setup. The magnetic flux generated by a permanent magnet is measured by applying Faraday's law, as explained before. The remanent magnetic polarization $J_r' = \mu_0 M_r'$ of the sample in open circuit conditions is calculated from *B* with a known correction factor, which contains the coil geometry. There are two ways of measuring J_r': a) the magnet is pulled out of the coils and moved far away. The displayed value will be J_r'. or b) the magnet is flipped by 180° in the coils (i.e. changed the top side to the bottom side). The displayed value will be $2J_r'$. For the determination of the closed circuit J_r the following relation [Trout1988] is used:

$$J_r = J_r' + J_r' * \mathcal{N} * (\mu - 1) \qquad \textbf{3-4}$$

The achievable sensitivity is 10^{-6} A/m and magnets with total dimensions up to 70 x 90 x 90 mm can be characterized. The device used in this work is produced by *Magnet-Physik Dr. Steingroever GmbH*.

3.2.2. Vibrating sample magnetometer

The working principle of the Vibrating Sample Magnetometer (VSM) is similar to the HCS, with the difference that the sample is vibrated periodically between a set of oppositely wound pick - up coils. The time - varying magnetic flux change B generates a sinusoidally alternating voltage in the coils which is proportional to the magnetic moment of the sample. The VSM needs to be calibrated with a reference sample before measurement, typically with a Ni sphere of known dimensions. As with the HCS, a correction for demagnetizing fields needs to be applied. The sample is vibrated in an homogeneous external field, which makes it possible to track $M(H_{ext})$ curves. The external field is created with large water - cooled Cu coils and concentrated in the airgap using tapered Fe or Fe-Co pole pieces. With the used device (*Lake Shore Cryotronics, Inc.*) a maximum field strength of 2 T can be generated. With an integrated heating/cooling unit measurement temperatures ranging from 77 - 1273 K can be realized.

A disadvantage for the characterization of permanent magnets is the relatively small required sample size. Typically the induced magnetic moment should not exceed 20 emu to prevent a bending of the filigree glass rods, on which the samples are mounted. Therefore, a typical sample size of the characterized samples in this work is a cube with dimensions of not more than 2 x 2 x 2 mm.

3.2.3. Pulsed field magnetometer

A very quick way to determine hysteresis curves of permanent magnets is the pulsed field magnetometer. As with the HCS, the magnetized sample is placed inside a pair of pick - up coils. By applying a field pulse of maximum 7 T, which is created by discharging a capacitor bank, a magnetization reversal is induced in the sample. The generated magnetic flux change is used to determine the open circuit magnetic moment of the sample. By applying a subsequent pulse the obtained data can be automatically corrected for the influence of eddy currents. For the device used in this work (*Metis Instruments)* the maximum sample size is about 30 mm (height) x 50 mm (diameter). With an integrated heating unit measurements up to 150 °C are possible.

3.2.4. Hysteresis graph

As opposed to the previous devices, the hysteresis graph measures in closed - circuit conditions. A magnetized sample is placed between two pole pieces, closing a magnetic circuit, and an external field of up to 2.4 T is applied with a conventional electromagnet. The magnetization of the sample is measured with two concentric J - compensated field coils, wound oppositely around the sample. The applied external magnetic field is measured simultaneously with a separate small search coil located in the airgap next to the sample. For the device used in this work (*Magnet-Physik Dr. Steingroever GmbH*) the sample size is comparatively large, up to 42 mm (height) x 59 mm (diameter). Measurement temperatures from RT up to 200 °C can be realized. As a disadvantage to the pulsed field magnetometer, the samples need two absolutely parallel top and bottom planes to enable the magnetic short circuit with the pole pieces. Also, one measurement typically takes several minutes.

3.2.5. Localized Hall probe

A fundamentally different way of determining magnetic fields is by exploiting the Hall effect with a Hall probe. A semiconducting sensor is inserted in a magnetic field and a voltage is generated in the sensor proportional to the magnetic flux density. The measurements a very simple, however, the probe needs to be calibrated and corrected for temperature fluctuations. Additional errors can arise from the facts that the Hall probe has to be aligned truly perpendicular to the magnetic field direction.

The lateral switching field profiles in chapter 4.1 were determined with a localized hall probe setup. For that, the samples were first exposed to a reverse field comparable to the coercivity of the magnet. The regions of the magnet which have a lower coercivity than the applied reverse field were demagnetized, whereas the region close to the surface, where the Dy was applied, remains magnetized in the initial direction. The distance of the transition line between these two regions is then determined by scanning over the area with a hall probe. By increasing the strength of the reverse field and repeating the hall probe scans the switching field was measured as a function of the distance from the surface. The lateral resolution of the used probe is ± 300 µm.

3.2.6. Kerr microscopy

The magneto - optic Kerr effect (MOKE) describes the phenomenon that light reflected from the surface of a magnetized material experiences a rotation of its plane of polarization [Hubert2014]. The rotation is characterized by the Kerr angle, which denotes the angular difference between the initial and the reflected plane of polarization. With an appropriate setting of analyzer and polarizer, the rotation can be visualized in a light microscope. This way it is possible to visualize magnetic domains, magnetization processes and to magneto - optically measure surface hysteresis loops. By utilizing specially designed and geometrically variable aperture diaphragm, it is possible to distinguish between the polar and the longitudinal Kerr effect. The first is sensitive to domains with magnetization pointing out - of - plane, the latter for in - plane magnetization. After careful metallographic polishing of the magnet surface, the device used in this work (*evico magnetics GmbH*) is able to visualize domains down to the limit of optical microscopy, which is about 300 nm with an 100x oil immersion objective.

3.2.7. Singular point detection method

With the singular point detection (SPD) method a direct determination of the anisotropy field H_a is possible. The method is suitable for powders and polycrystalline permanent magnets with a high degree of orientation [Kirchmayr1991]. The method involves the measurement of the M(H) curve in hard direction until the saturation is reached. In the present work samples were measured in fields up to 14 T. The minimum in the second derivative of M(H) curve is then corresponding to H_a. Nishio et al. [Nishio1996] compared several methods for the determination of H_a in Sr - ferrites and (Nd,Dy)-Fe-B permanent magnets and concluded the SPD method is most practical for RE magnets with huge anisotropy.

4. The grain boundary diffusion process of rare earth elements in Nd-Fe-B permanent magnets

In the following chapter, the detailed diffusion mechanisms within the magnets as well as their temperature dependence is investigated. The chapter is divided in two parts:

4.1) First, the temperature dependence of the Dy diffusion in commercial, nearly HRE free sintered Nd-Fe-B magnets is studied. Besides the overall bulk magnetic properties the focus lies on the lateral gradient coercivity profiles created within the magnets. With correlated magnetic characterization and electron microscopy the diffusion mechanisms were investigated on multiple length scales, ranging from millimeters for the grain boundary diffusion into the magnet to nanometers for the bulk diffusion from the GB into the grains.

4.2) Based on these obtained results and optimized annealing temperature regimes, the second part expands the focus to other RE elements, namely Tb, Ce and Gd, and another magnet class with a high content of HRE. Furthermore, the influence of the GBDP on micromagnetic parameters will be investigated.

4.1. Analysis of temperature dependence and diffusion mechanism of Dy in Dy - free permanent magnets

Parts of the results presented in this subchapter were obtained in close cooperation (BMBF PerEMot project) with Vacuumschmelze GmbH & Co. KG [Loewe2015]. Where marked, the samples were prepared at Vacuumschmelze GmbH & Co. KG and the magnetic characterization was performed at Vacuumschmelze GmbH & Co. KG.

4.1.1. The influence of Dy diffusion on the magnetic properties

As was described in chapter 3.1.1, nearly Dy - free commercial magnets (10 x 10 x 3 mm) were heat treated after applying a slurry of Dy powder. The demagnetization curves of samples coated on both pole surfaces (10 x 10 mm) and annealed at T_a = 700 °C, 800 °C, 900 °C and 1000 °C are shown in Figure

4-1 (left), together with a typical demagnetization curve of a sample in the initial state prior to the diffusion treatment. All measurements were performed at 20 °C with a Hysteresis - graph. The increase in coercivity induced by the grain boundary diffusion process can clearly be observed. The squareness of the demagnetization curve is not substantially altered by Dy diffusion, which indicates a rather homogeneous coercivity throughout the complete sample volume. Consequently, the diffusion length of Dy has to be significantly larger than 1.5 mm, which is particularly remarkable for an annealing temperature of 700 °C and suggests the presence of an adequate amount of liquid GB phase even in the low temperature regime.

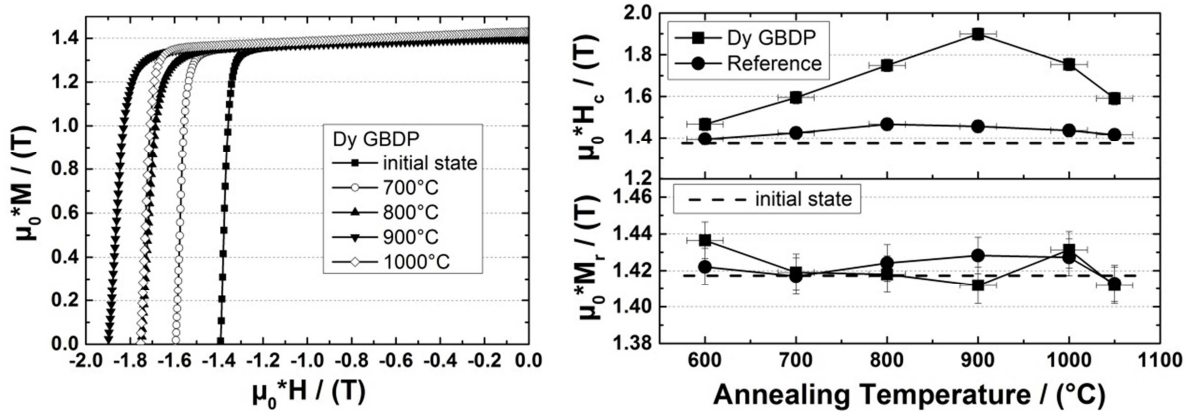

Figure 4-1: Demagnetization curves of Dy - coated samples after grain boundary diffusion processes at 700 °C ≤ T_a ≤ 1000 °C for 6 h and of a reference sample in the initial state (left). Room temperature coercivity $H_{c,M}$ of bulk samples after diffusion treatment for 6 h at 600 °C ≤ T_a ≤ 1050 °C and corresponding remanent polarization B_r (right). *The measurements were performed at Vacuumschmelze GmbH & Co. KG.*

The magnetic properties of coated samples and annealed at 600 °C ≤ T_a ≤ 1050 °C are summarized in Figure 4-1 (right) in comparison with uncoated reference samples which have been subjected to the same annealing treatment and typical properties of samples in the initial state. It can be clearly seen that the diffusion treatment leads to an increase in coercivity with a pronounced maximum at around 900 °C, while the remanent polarization of the samples is not significantly affected by the diffusion process. For T_a = 900 °C, a coercivity of $\mu_0 * H_c$ = 1.90 T was determined which corresponds to an increase in coercivity $\Delta(\mu_0 * H_c)$ of around 0.52 T compared to the initial state. A comparison with uncoated reference samples reveals that about 0.08 T of this coercivity increase can be attributed to an improved annealing treatment and a $\Delta(\mu_0 * H_c)$ of 0.44 T is induced by the Dy diffusion process. Note that the reference sample annealed at T_a = 1050 °C is not showing a reduced coercivity with respect to samples in their initial state indicating that no significant grain growth occurs during the annealing treatment. Thus, the

reduction of $\Delta(\mu_0 * H_c)$ at annealing temperatures higher than 900 °C is very likely an influence of accelerated bulk diffusion which limits the formation of Dy - enriched $(Nd,Dy)_2Fe_{14}B$ grain boundaries. The X and Y error bars in Figure 4-1 (left) mark temperature inhomogeneities in the annealing oven and random statistical errors, respectively.

In the results described above the Dy was applied to both 10 x 10 mm large pole faces and consequently the Dy diffused along the thickness of 3 mm of the sample. In order to investigate the diffusion depth in more detail another set of samples was prepared where the Dy was applied to one of the lateral 10 x 3 mm large faces of the magnets. After the diffusion treatment at 700 °C ≤ T_a ≤ 1000 °C, the dependence of the local magnetization reversal ("switching field" $\mu_0 * H_S$) on the distance to the coated surface was measured with a custom built scanning Hall probe setup after applying appropriate reverse fields at room temperature.

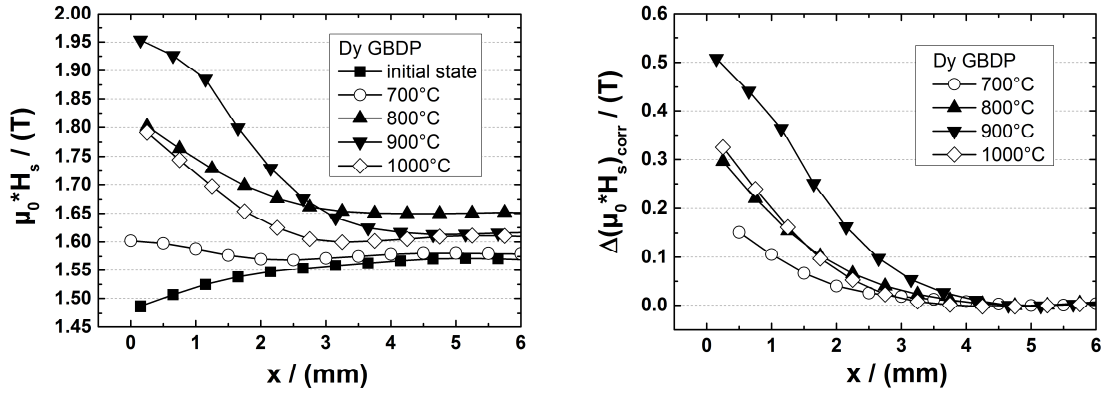

Figure 4-2: Dependence of the switching field variation ΔH_S on the distance x to the Dy coated lateral surface of samples after a grain boundary diffusion process at 700 °C ≤ Ta ≤ 1000 °C for 6 h and of one sample in the initial state without diffusion process. Note that for better visibility, the error bars of Δx = +/- 300 µm (spatial resolution of the Hall probe) and ΔH_S = +/- 40 kA/m are not indicated. *The measurements were performed at Vacuumschmelze GmbH & Co. KG.*

Figure 4-2 (left) shows the dependence of the switching field $\mu_0 * H_S$ for samples after diffusion treatment at different T_a and for a sample in the initial state. For the sample in the initial state a small reduction of $\mu_0 * H_S$ was observed in the vicinity of the surface. This reduction is not related to actual material properties, but can very likely be attributed to edge effects as the measurements have been performed in open circuit conditions. The differences in bulk switching field $\mu_0 * H_S$(x = 6 mm) stem from a spread in coercivity in the initial samples. Shown in Figure 4-2 (right) is the corrected difference in switching field

$\Delta(\mu_0{*}H_S)_{corr}$, which is defined as the difference between $\mu_0{*}H_S$ and the bulk value of $\mu_0{*}H_S$ at 6 mm, subtracted by the switching field of the sample in the initial state:

$$\Delta(\mu_0 * H_S)_{corr} = [\mu_0 * H_S(x) - \mu_0 * H_S(x = 6mm)] - \mu_0 * H_{S,initial\,state}(x) \quad \textbf{4-1}$$

After the diffusion treatment, all samples show an increase of $\Delta(\mu_0{*}H_S)_{corr}$ in the proximity of the coated surface. The largest increase is observed for T_a = 900 °C. For this diffusion temperature, the switching field was increased by about 0.53 T compared with the measurements done on the sample in the initial state and a penetration depth of about 3 mm to 4 mm could be determined. These values correspond well with the previous measurements after T_a = 900 °C, where an increase in coercivity of 0.52 T could be attributed to the diffusion treatment. Temperatures lower or higher than 900 °C lead to a reduction of $\Delta(\mu_0{*}H_S)_{corr}$. Interestingly, the penetration depth also shows a maximum for T_a = 900 °C. Higher annealing temperatures do not lead to larger penetration depths, and the switching field distribution after T_a = 800 °C is very similar to the switching field distribution after T_a = 1000 °C. This peculiar behavior might be explained by an increased bulk diffusion coefficient of Dy at 1000 °C compared to 900 °C. The resulting faster diffusion into the grains might lead to a faster depletion of Dy and therefore to a reduced penetration depth.

4.1.2. Microstructural changes during the grain boundary diffusion process

Figure 4-3 shows SEM images of the near - surface microstructure of Nd-Fe-B permanent magnets after Dy diffusion at various temperatures for 6 h using backscattered electron (BSE) contrast.

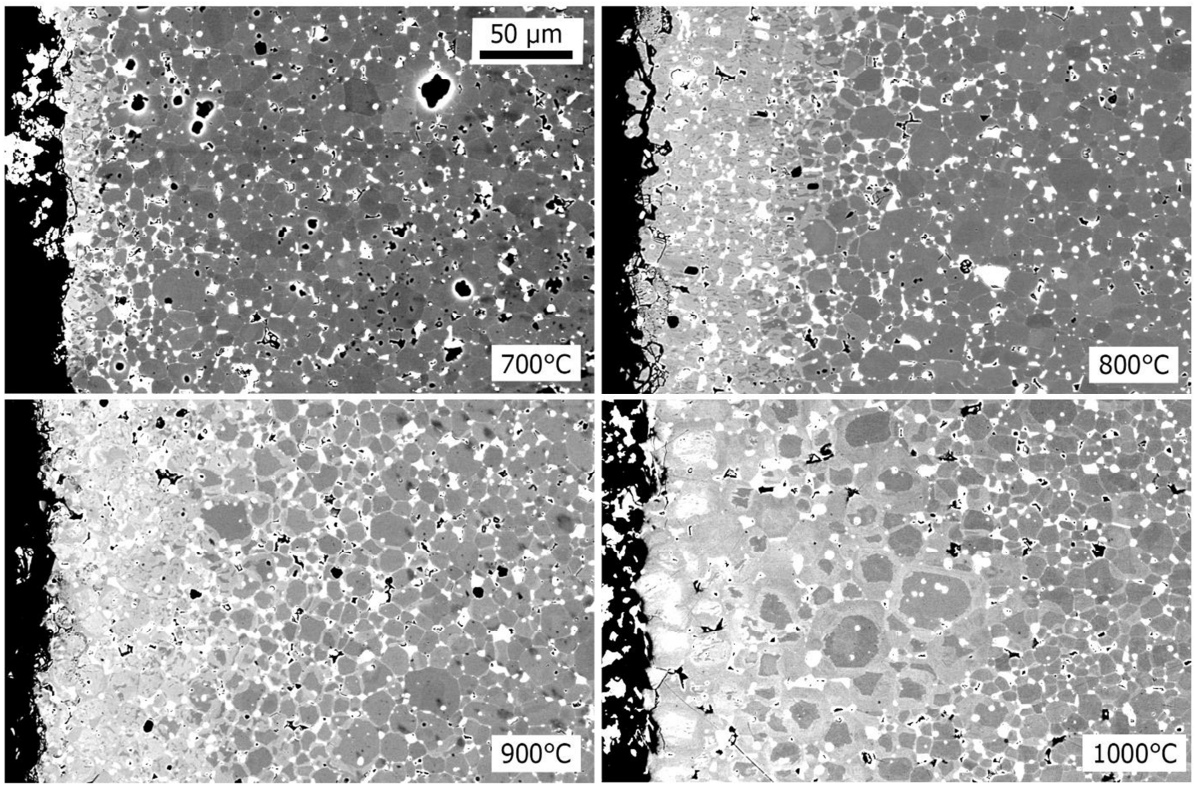

Figure 4-3: Back scattered electron (BSE) SEM images of near surface transverse sections of Dy - coated samples after annealing for 6 h at 700 °C - 1000 °C.

Compared to the microstructure of typical Nd-Fe-B sintered magnets which consist of $(Nd,Dy)_2Fe_{14}B$ grains surrounded by nanometer thick RE - rich grain boundaries [Woodcock2012], the Dy diffusion processed samples exhibit distinct differences. First, the grains in vicinity of the coated surface show an enhanced BSE signal and appear brighter, which indicates a higher average atomic weight as compared with grains further apart from the Dy - coated surface. These grains exist up to a distance of about 10 µm at 700 °C to more than 50 µm at 1000 °C. Secondly, adjacent to this zone a pronounced core - shell structure of the $(Nd,Dy)_2Fe_{14}B$ grains can be observed, as was mentioned in the introduction. The thickness of the shells is decreasing from about 1 µm with increasing distance and is only visible up to a depth of around 500 µm for annealing temperatures of 900 °C to 1000 °C. Further away from the surface the thickness of the Dy - enriched shells is below the resolution of BSE SEM.

Due to the high amount of Dy in the outermost surface grains, the remanent magnetic polarization has to be substantially reduced compared to their initial state prior to the diffusion process. For practical applications one therefore needs to consider the avoidance or removal of such surface layers to retain a high total remanence. In this study, the surface layer has a thickness of around 150 µm after applying an

optimum annealing temperature of 900 °C. Consequently, the impact of a removal of such surface layers on the production costs has to be considered when weighing the economic benefits of the reduced usage of Dy through the GBDP.

EDX maps of Dy, Nd and Fe (Figure 4-4) reveal that the increase in average atomic weight of the $(Nd,Dy)_2Fe_{14}B$ grains and $(Nd,Dy)_2Fe_{14}B$ shells is induced by the replacement of Nd by Dy. While the Fe concentration in the $(Nd,Dy)_2Fe_{14}B$ grains remains independent of the distance to the coated surface (the slight variation of the Fe contrast is most likely an measurement artefact due to the overlap of the Fe K_α peak with the Dy L_α peak), a clear reduction of the Dy concentration with increasing distance to the coated surface can be observed.

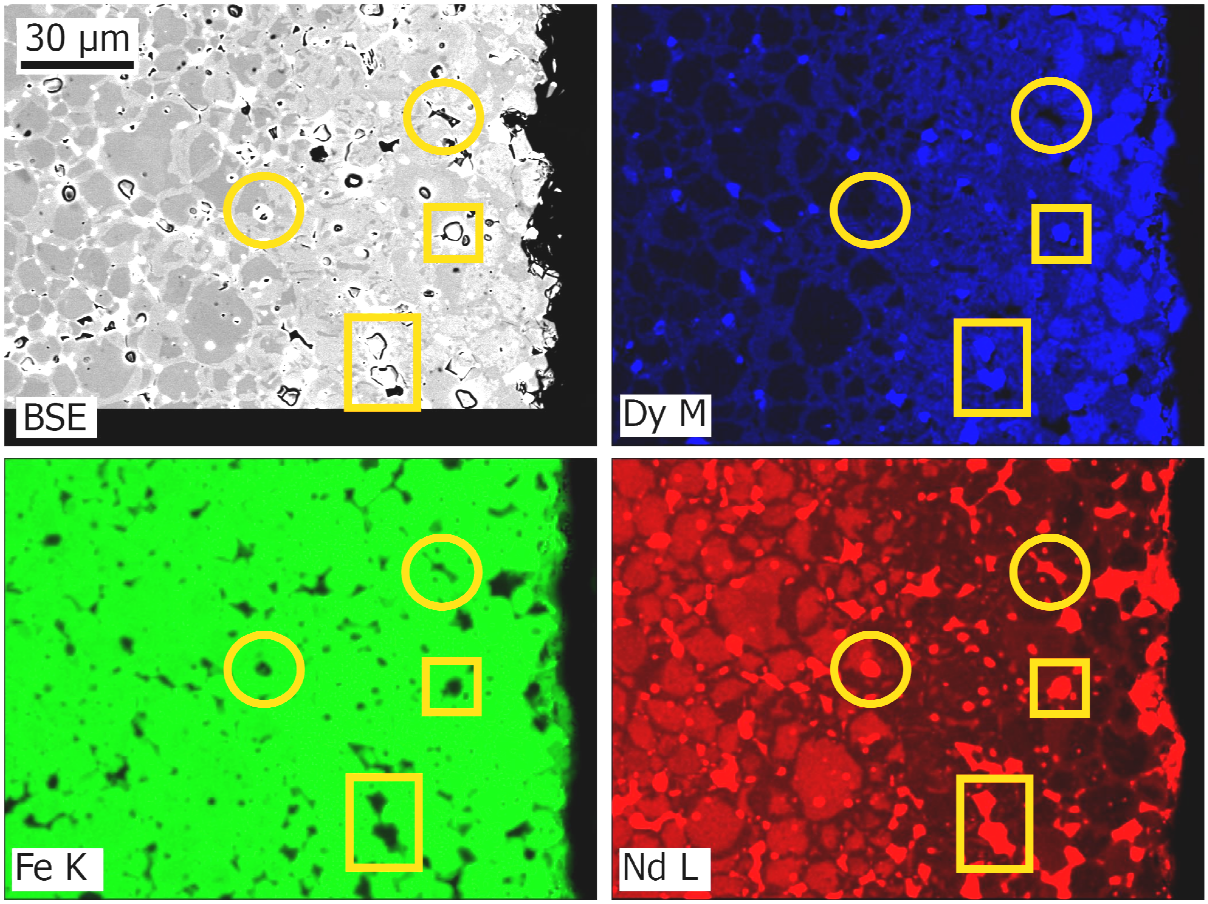

Figure 4-4: BSE SEM image of a near surface transverse section of a Dy - coated sample after annealing at 900 °C for 6 h and corresponding EDX maps of Dy, Nd and Fe. Two examples of Nd - rich grain boundary phase are indicated by circles, two examples of a both Nd and Dy - rich grain boundary phase are indicated by squares.

Beside the formation of Dy - enriched $(Nd,Dy)_2Fe_{14}B$ grains and shells, the diffusion process has also an influence on the RE - rich grain boundary phases. At least two different Dy/Nd ratios can be distinguished in the EDX maps. One grain boundary phase is both Dy and Nd - rich (Figure 4-4, squares) while the other phase is only Nd - rich (Figure 4-4, circles). It seems reasonable that the Dy-poor grain boundary phases consist of Nd-Oxide phases which have been present prior to the diffusion process and remained solid at 900 °C. Thereby, the diffusion coefficient of Dy within the oxide - phase is much smaller as compared to the residual RE - rich grain boundary phase which becomes liquid at about 670 °C [Schneider1986]. The detailed impact of the various Nd - oxide phases on the actual diffusion process was not determined here and needs to be considered in future research activities.

4.1.3. Investigation of the shell formation mechanism

To study the mechanisms involved in the formation of the Dy - enriched shells, WDX line scans (Figure 4-5) and EBSD mapping (Figure 4-6) have been performed. The WDX line scan shows that both the Dy and Nd content remain constant within a shell. Thus, the formation by a conventional bulk diffusion process seems unlikely and the results support a model in which the surface region of the $(Nd,Dy)_2Fe_{14}B$ grains is partially molten at elevated temperatures, as was proposed by Sepehri-Amin et al [Sepehri-Amin, Ohkubo and Hono2013]. Upon cooling the Dy - enriched $(Nd,Dy)_2Fe_{14}B$ phase solidifies and crystallizes on the matrix grains to form the Dy - rich shells.

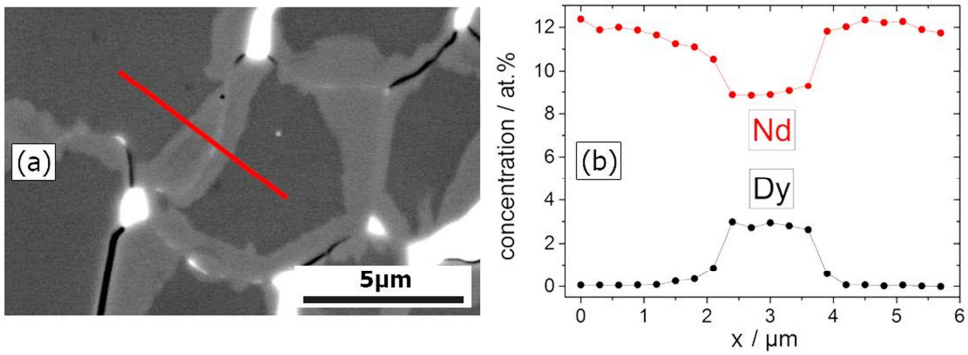

Figure 4-5: (a) BSE SEM image of the transverse section of a Dy - coated magnet after annealing at 900 °C for 6 h and (b) corresponding WDX line scan showing the Dy and Nd concentration. The analyzed area was at a distance of ≈110 µm to the coated surface.

EBSD has been used to study possible orientation differences between the shells and the matrix grains in a sample annealed at 900 °C for 6 h (Figure 4-6). The differences in lattice parameters are small and therefore neglected (c - axis: $Nd_2Fe_{14}B$ = 12.03 Å, $Dy_2Fe_{14}B$ = 11.83 Å [Herbst1991]). As a result, all of the values for the intragranular average misorientation angle are smaller than 1° (which is about the limit of the angular accuracy of EBSD) i.e. all the grains are perfect single crystals. This means that the shells grow epitaxially on the surface of the grains.

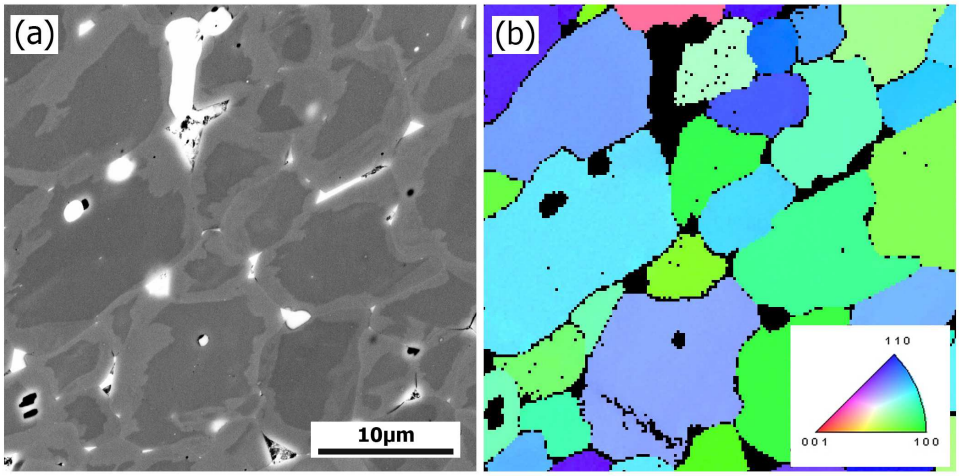

Figure 4-6: (a) BSE SEM image of the transverse section of a Dy - coated magnet after annealing at 900 °C for 6 h and (b) EBSD orientation map of the very same region. The shells show no detectable orientation difference to the inner parts of the grains. The white Nd - rich phase regions in (a) are not indexed and appear black in (b). The map was recorded close to the sample surface. *Help with the EBSD analysis by T.G. Woodcock (IFW Dresden) is gratefully acknowledged.*

Figure 4-7 shows a region with a pronounced core - shell structure in BSE contrast and the Kerr image of the very same region. The nominal easy axis of the material is out - of - plane. The Kerr microscope is used with polar contrast and thereby the sensitivity direction is parallel to the easy axis of magnetization and black and white areas can be referred to domains with magnetization along the easy axis. The pattern shows so - called star - like domains and is characteristic for uniaxial materials in this direction of observation. Due to the presence of a paramagnetic grain boundary phase and consequently a decoupling of the grains, inter - grain magnetostatic interactions are expected to be dominant. However, in a few cases the magnetic domains were found to extend over the grain boundaries into neighboring grains, which can be explained by dipolar interactions at the surface [Khlopkov2004, Khlopkov2007]. In most cases there was no visible difference between shells and grains in the Kerr images (Figure 4-7b). A correspondence of BSE and Kerr contrast with the core - shell structure can only be detected in exceptional cases (e.g. top part of Figure 4-7c). As the majority of domains run uninterrupted through

the core - shell interface a relatively undisturbed transition layer seems likely which corresponds well with the EBSD analysis in Figure 4-6, where no orientation difference between shells and grains could be found.

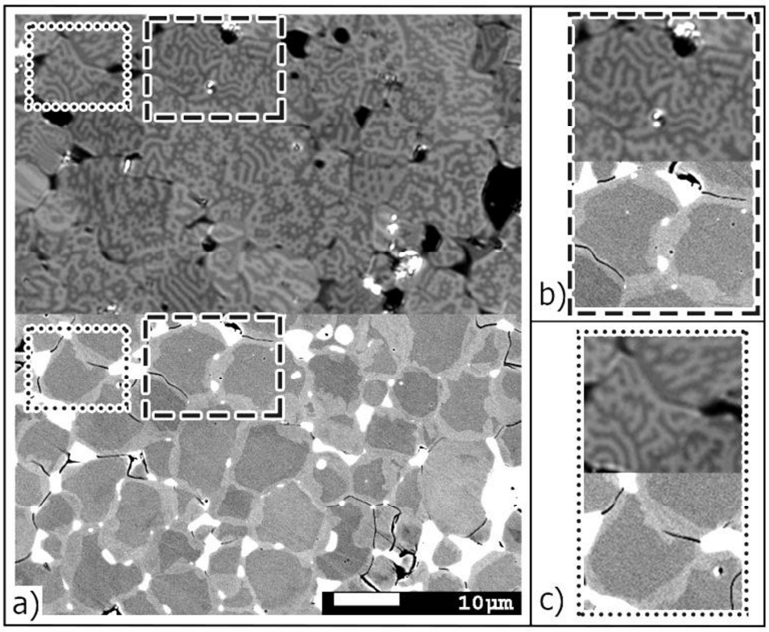

Figure 4-7: Microstructure of a Dy coated magnet after annealing at 900 °C for 6 h. a) Correlation between magneto-optical Kerr (top) and SEM BSE (below) contrast. The respective images show the exact same region of the sample. The easy axis of the material is pointing out - of - plane and the Kerr image is showing polar contrast. b) and c) show magnified views from a).

4.1.4. Analysis of diffusion regimes on different length scales

Concerning the Dy diffusion, two regions can be distinguished in the sample:

1) In the *surface region*, ranging to a few 100 µm into the magnet bulk, the microstructure is heavily enriched with the diffusing Dy, which leads to the formation of µm - thick (Nd,Dy)-Fe-B shells (Figure 4-3). The concentration of Dy can be measured directly in the SEM and quantified with EDX/WDX.
2) Adjacent is the "*grain boundary tail*" (GBT) region [Mehrer2007], ranging up to a few mm into the bulk of the magnet. It is characterized by Dy diffusion over the grain boundaries. An indirect determination of the Dy concentration is possible through coercivity measurements, in analogy to the radio tracer method conventionally used in determining diffusion profiles [Mehrer2007]. In the GBT region also a *bulk*

diffusion from the grain boundaries into the grains can be observed with transmission electron microscopy coupled with EDX/WDX.

A principal difference to the described diffusion theory in chapter 2.2.1 is the occurrence of a liquid phase during the diffusion. Between 600 - 700 °C Nd-rich phases and partly the Nd-Fe-B grains are melting to produce a RE - rich liquid grain boundary phase, over which the diffusion mainly takes place. The amount of liquid phase is increasing not only with temperature, but also with the total concentration of RE [Seelam2014]. In the following sections the diffusion regions are described in more detail.

1) Surface region

As was shown in Figure 4-3 the diffusing RE is highly enriched in the immediate surface region of the sample. The concentration of Dy in dependence of the diffusion length can be directly measured and quantified in the SEM because the shells are sufficiently broad to allow a chemical analysis with EDX/WDX. Figure 4-8 shows the results of WDX analysis performed within the shell regions at various distances d to the Dy - coated surface, performed on a sample annealed at 900 °C for 6 h.

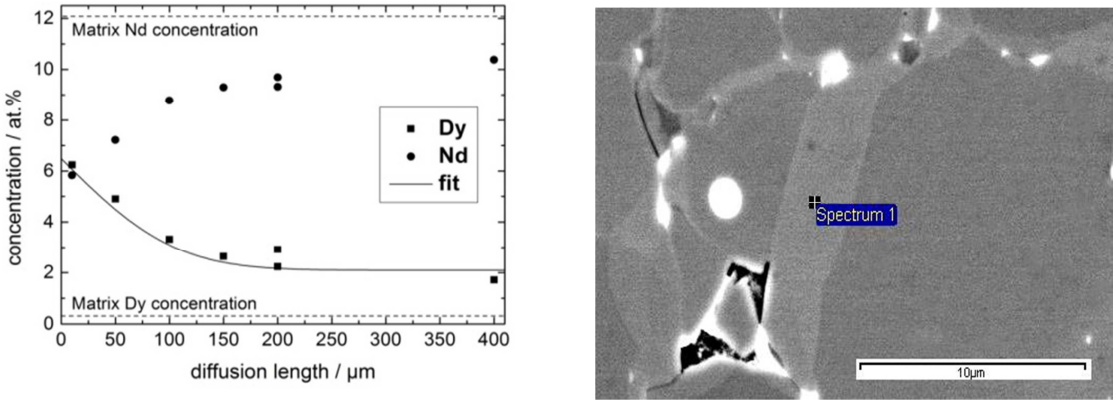

Figure 4-8: Concentration profile of Dy in a Nd-Fe-B magnet after GBDP at 900 °C (left). Example of a measurement spot in a shell 150 µm away from the surface.

The Dy content rapidly decreases from around 6 at.% to values below 2 at.% at diffusion distances larger than 400 µm. The Nd concentration shows the opposite behavior leading to a constant sum of the Nd and Dy concentrations of about 12 at.% which corresponds to the $(Nd,Dy)_2Fe_{14}B$ phase. The concentration profile can be fitted to an error function (equation 2-12). A constant source is assumed

and that the diffusion occurs solely over a rare earth rich liquid eutectic phase along the grain boundaries of the otherwise solid grains. Furthermore, the diffusion coefficients shall be independent of concentration and there are no convective effects within the liquid. From the fit, the diffusion coefficient of Dy within Nd-Fe-B permanent magnets at 900 °C has been determined to be $D_{Dy}(900\ °C) = (2.5 \pm 0.5) \times 10^{-9}\ cm^2/s$. Note that although the absolute values of concentration might include errors due to measurement artifacts, only the slope of the curve is governing D, which improves the reliability of the obtained results.

There have been previous attempts to determine D of Dy in the system Nd-Fe-B. Cook et al. [Cook2001] assembled pairs of cast and annealed single - phase compositions of $R_2(Fe_{0.714}Co_{0.286})_{14}B$ where R = Nd or Dy. After a heat treatment at 1050 °C they measured the concentration gradient of Dy with EDX. Despite the higher annealing temperature, they found a substantially smaller diffusion coefficient $D_{Dy}(1050\ °C)$ of $2.9 \times 10^{-12}\ cm^2/s$. It is likely that the huge difference to the here determined value is originating from the different amounts of liquid phase. As Cook et al. have used a Dy-source which remains solid during the annealing treatment, the obtained average Diffusion coefficient is strongly influenced by bulk diffusion. In the here used experimental setup, the Dy concentration is clearly dominated by diffusion along the liquid phase and consequently a diffusion coefficient which is 3 orders of magnitude higher is not unreasonable.

A classification of the surface region diffusion kinetics into the categories described in chapter 2.2.1 is difficult, since the diffusion theory does not contain a solid - liquid transition, as is it most likely happening during the diffusion (cf. the phase diagram in Figure 2-6). For an adequate description of the diffusion at the surface the material should not be polycrystalline, but rather a homogeneous melt. The diffusion in metallic liquids can also be described by Fick's laws [Horbach2007], just with a higher diffusion constant (cf. Figure 2-8).

2) Grain boundary tail region

The Grain boundary tail (GBT) region is characterized by the diffusion of Dy over the grain boundaries. It is deposited only there and within the first few nm of the grains, resulting in overal Dy concentrations not detectable by SEM EDX. Therefore, the concentration change is measured indirectly with coercivity (or switching field) measurements. The underlying assumption is that the increase in coercivity H_c or switching field H_s is directly proportional to the concentration of diffused Dy. As was described in chapter 2.2.1, the shape of the lateral switching field profiles gives information about the type of diffusion

mechanism. If $\log(\Delta(\mu_0 * H_S))$ plotted against $x^{6/5}$ follows a linear function, it is type B. If $\Delta(\mu_0 * H_S)$ can be fitted to an error function, it is type C. Figure 4-9 exemplary shows the switching field profile of the GBDP sample annealed at 900 °C, plotted according to type B (top) and C (bottom). From the curves it can be safely assumed that the grain boundary diffusion inside the bulk of the magnet occurs via type C.

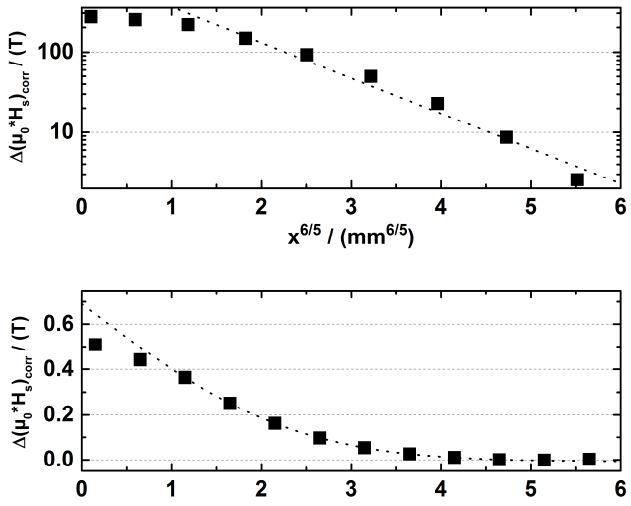

Figure 4-9: Switching field profile of a GBDP sample annealed at 900 °C (cf. Figure 4-2). The data points in the bottom graph were fitted to equation 2-12. For the fit the data points close to the surface have been omitted in order to exclude edge effects. The data for the other investigated temperatures of 700 °C, 800 °C and 1000 °C show the same behavior.

As was stated in chapter 2.2.1, the categorization between type B and C diffusion kinetics is based on the magnitude of the bulk diffusion length $\sqrt{Dt}$ vs the grain boundary width $s\delta$ and the grain size d. In the next paragraph it will be shown that $\sqrt{Dt}$ is larger than the grain boundary width, but of the same magnitude. These findings agree well with the categorization into the type C and the shape of the concentration profile in Figure 4-9.

The least - squares fit of the data presented in Figure 4-2 (left) to equation 4-3 yields temperature dependent values for D_{Dy} (Table 4-1). The values confirm the observation that the diffusion is fastest at 900 °C. The values are more than two orders of magnitude larger than the before determined diffusion coefficient in the surface region (cf. Figure 4-8).

Table 4-1: Grain boundary diffusion coefficients D_{Dy}, determined from diffusion data (Figure 4-2) fitted to equation 4-3. Note that for the fit the data points close to the surface have been omitted in order to exclude effects of bulk diffusion from the surface.

	700 °C	800 °C	900 °C	1000 °C
D_{Dy} in [10^{-7} cm^2/s]	5.15 ± 0.33	7.05 ± 0.21	7.90 ± 0.05	5.91 ± 0.17

3) Bulk diffusion from the grain boundary into the grains

As described before, after a diffusion length of approximately 0.5 mm no Dy - rich shells can be observed anymore by SEM. To overcome these limitations, a grain boundary located about 1.5 mm away from the surface has been investigated with STEM EDX (Figure 4-10).

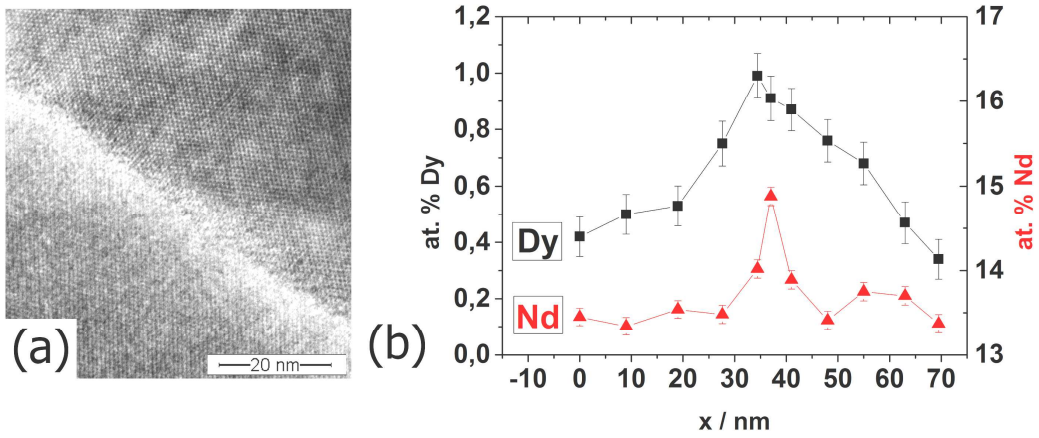

Figure 4-10: (a) STEM image of a grain boundary located 1.5 mm apart from the Dy - coated surface of a magnet annealed at 900 °C for 6 h and (b) corresponding EDX line scan.

The analysis shows that the peak Dy content at the grain boundary is around 1 at.%. The value must be regarded as rough estimation due to the principal errors of the EDX method when evaluating low energy peaks like Dy M_α. Nevertheless, it is significantly higher than the average Dy concentration prior to the diffusion process. Hence, this measurement demonstrates that Dy can easily diffuse more than 1.5 mm into a magnet body which is in good agreement with the magnetic characterization of the switching field distribution revealing a penetration depth in the order of 3 - 4 mm (Figure 4-2). Focusing on the Dy gradient along the line scan, a penetration depth of around 20 - 30 nm into the $(Nd,Dy)_2Fe_{14}B$ grain can

be determined. As micromagnetic model calculations have revealed, a reduced magnetocrystalline anisotropy of a 3 nm thick region around individual Nd-Fe-B grains has significant impact on the coercivity of the bulk magnet [Bance2014]. Therefore, a Dy enrichment up to a penetration depth of 20 nm to 30 nm can adequately explain the coercivity increase induced by the diffusion process.

Compared with the WDX measurements of the Dy - content within the shells of the surface area (Figure 4-5), no plateau of the Dy content can be observed, indicating that the Dy - enriched shell formed through bulk diffusion. Using the approximation for the bulk diffusion length $x_{bulk} = \sqrt{D_{Dy,bulk} t}$ a $D_{Dy,bulk}$(900 °C) ≈ 1 × 10^{-15} cm^2/s can be estimated. It has to be noted that x_{bulk} is subjected to substantial errors due to the thickness of the TEM lamella and unknown orientation of the grain boundary with respect to the beam, as well as the unknown amount of liquid phase during the annealing treatment. The bulk diffusion length is a few dozen nm and therefore in the same order of magnitude as the grain boundary thickness.

With the obtained results it is now possible to estimate the amount of Dy that is actually needed for the magnetic hardening through the GBDP. If one assumes that a 3 nm layer around each grain with a Dy concentration of 1 wt.% is sufficient, and if the grains are cubes with a side length of 7 µm, then only about 0.003 wt.% (compared to the total mass of the magnet) of Dy are necessary. In other words, the 0.6 wt.% Dy that were applied in the experiments are a 200 - fold waste of resources. The problem still unsolved is that the HRE are deposited mainly in the oversaturated surface regions, where they are not as effective as in the bulk. Even worse is that in industrial practice the surfaces of the magnets are grinded off in order to maintain a high remanence and the HRE are lost.

4.2. Grain boundary diffusion of Dy, Tb, Gd and Ce in Dy - rich permanent magnets

In the following several RE elements as diffusion media are investigated: the “traditional” HRE Dy and Tb used in industry, as well as Ce and Gd. Two Nd-Fe-B sample materials were chosen: one with Dy addition for high temperature applications and for comparison the nearly Dy - free material from the previous chapter. So far only a single study exists, which also investigates the diffusion of Dy in Nd-Fe-B magnets with high Dy contents [Kim2016].

Gd - rich grain boundaries are of interest because they relate to the concept of increasing coercivity by adding a ferrimagnetically exchange - coupled surface layer to the Nd-Fe-B grains. This

superferrimagnetism concept was suggested by Akdogan et al in 2014 [Akdogan2014]. In their thin film approach a GdFe layer was deposited on NdFeB, which leads to an antiferrimagnetic (i.e. antiparallel) coupling of the magnetic moment of Gd to the moments of Fe and Nd in the $Nd_2Fe_{14}B$ phase. Under an applied field that tends to reverse the magnetization of the grain, the surface layer, with a magnetization parallel to the applied field, works against reversal and impedes the nucleation of reverse domains. The magnetism of $Ce_2Fe_{14}B$ shows distinct differences to $Nd_2Fe_{14}B$ as a result of different valence states of Nd in $Nd_2Fe_{14}B$ and Ce in $Ce_2Fe_{14}B$ (3 vs. 3.44, [Capehart1993]). At room temperature, the saturation magnetization of $Ce_2Fe_{14}B$ is 26% lower than of $Nd_2Fe_{14}B$, and the anisotropy field is 3 times lower [Herbst1991]. Consequently, Ce substitution leads to deterioration of the intrinsic properties of the $Nd_2Fe_{14}B$ phase and grain boundaries enriched by Ce should give an adverse effect on coercivity. A quantitative analysis of this effect in our experiments can provide a comprehensive view on the GBDP.
Macroscopically and microscopically, the GBDP creates an inhomogeneous distribution of diffusing RE, and therefore coercivity, within Nd-Fe-B sintered magnets [Sepehri-Amin, Ohkubo and Hono2013]. The diffusion depth is only several mm, which geometrically limits the maximum size a diffusion treated magnet can have if a relatively homogeneous coercivity is desired. The question arises, whether it is necessary to magnetically harden the whole magnet or if for some applications a surface hardening is sufficient. To answer the question different lateral coercivity profiles are created through varied annealing time and the above described choice in RE, and are then compared to overall magnetic properties. Diffusion constants are determined from these profiles. They help to evaluate necessary heat treatment times to achieve wanted diffusion depths.

4.2.1. Influence on magnetic properties

Figure 4-11 shows the demagnetization curves of the Dy - rich sample magnets, which were diffusion treated with Dy, Tb, Ce and Gd, respectively (the detailed experimental setup is described in chapter 3.1.1). These samples will be labeled “Dy”, “Tb”, ”Ce” or ”Gd” magnets in the following. While the former two rare earths (RE) lead to an increase in coercivity, the latter two decrease it. The striped bars mark the coercivity and magnetization range of 10 reference samples, which underwent the same heat treatment as the respective samples (900 °C, 1.5 - 10 h and 500 °C, 2 h) but without diffusing RE.

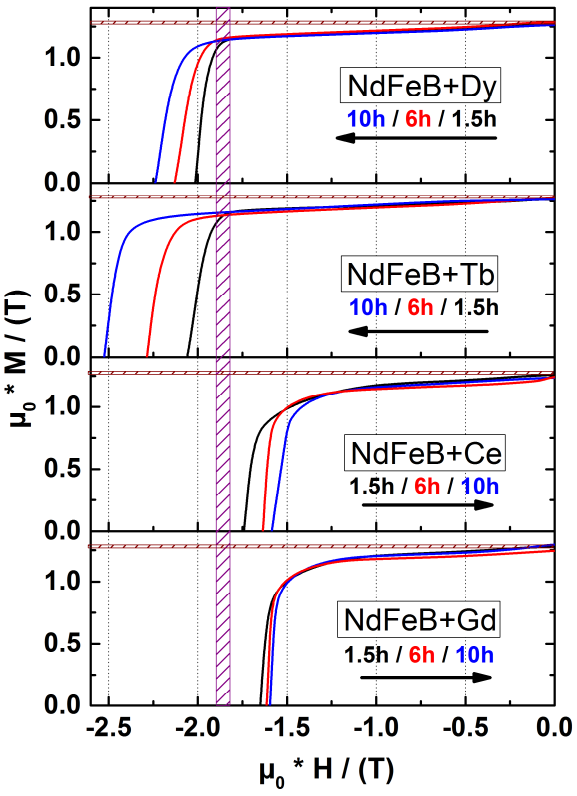

Figure 4-11: Demagnetization curves of the Dy - rich Nd-Fe-B magnets after diffusion for different annealing times at 900 °C. The shaded bars mark the coercivity and remanence range for 10 reference samples heat treated without diffusing RE.

Depending on the heat treatment time the coercivity difference $\mu_0 * \Delta H_c(Dy)$ after the diffusion ranges from 0.15 T to 0.35 T (Figure 4-12). $\mu_0 * \Delta H_c(Tb)$ is almost twice as large with 0.2 T to 0.6 T. The diffusion treatment with Ce leads to a decrease of $\mu_0 * \Delta H_c(Ce)$ from -0.1 T to -0.15 T, which is similar to the Gd values. The magnetization is almost the same for all samples before and after the annealing.

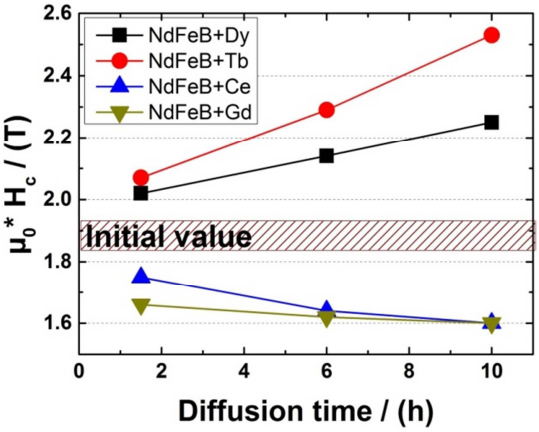

Figure 4-12: Coercivity values vs. diffusion time of the samples shown in figure 1. The coercivity of the magnets treated with Dy and Tb increases over time while the one with Ce and Gd decreases.

The coercivity changes follow the literature values for the anisotropy fields $\mu_0 * H_a$ of the $RE_2Fe_{14}B$ compounds. At room temperature these values for RE = Tb, Dy, Nd, Ce and Gd are 22 T, 15 T, 7.3 T, 2.6 T and 2.4 T, respectively [Herbst1991]. One way to evaluate the effectiveness of the diffusion process is proposed in Figure 4-13.

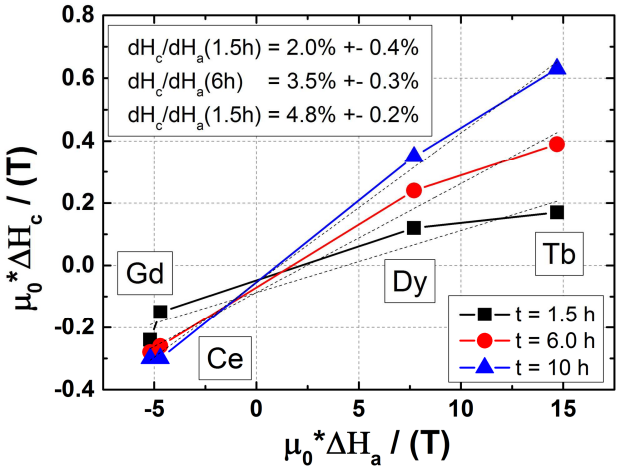

Figure 4-13: Plot of the coercivity changes $\Delta\mu_0 * H_c$ after the GBDP against the difference in the anisotropy fields $\Delta\mu_0 * H_a$. The slope of the curves can be interpreted as effectiveness of the GBDP.

Here, the coercivity changes $\Delta\mu_0 * H_c$ after the GBDP are displayed against the difference in the anisotropy fields $\Delta\mu_0 * H_a$ between the diffusing RE and Nd, for t = 1.5 h, 6 h as well as 10 h. The slope of the curves corresponds to the percentage of H_a difference, which could be translated into coercivity. With a

reasonably good fit result a linear dependence between the two quantities is found, meaning that $\Delta\mu_0*H_c$ is directly related to $\Delta\mu_0*H_a$. The slope is in the order of a few %, and increases with increasing diffusion time, from 2% for 1.5 h to almost 5 % for 10 h. The reason for the increase is most likely, that the RE penetrated deeper into the magnet and are distributed more homogeneously. In other words, the longer the heat treatment for otherwise same parameters, the higher the effectiveness of the GBDP.

Selected samples from Figure 4-11 have been cut into slices perpendicular to the diffusion direction. The coercivity of the slices has been measured and lateral coercivity distributions have been constructed (Figure 4-14a-c). For comparison, the diffusion of Dy and Tb after 1.5 h in the Dy - lean magnets is also shown (Figure 4-14d).

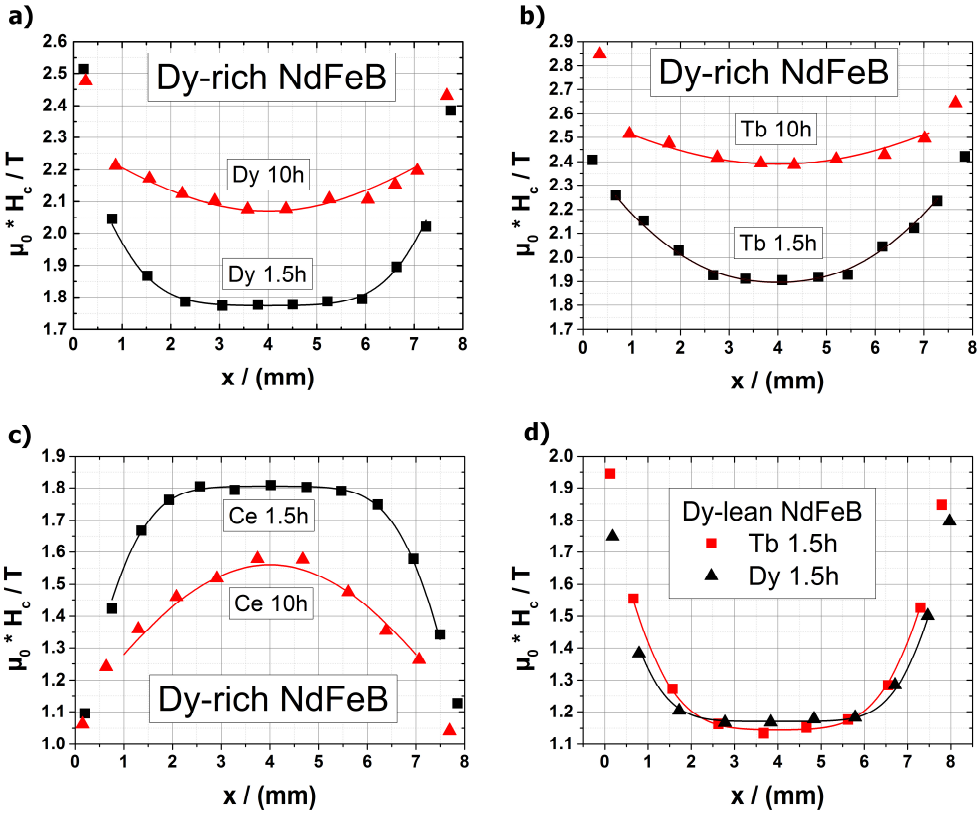

Figure 4-14: Lateral coercivity profiles of selected samples from Figure 4-11. Each data point marks the coercivity of a single slice cut from the whole magnet. The solid lines are data fits according to equation 4-3. a-c) Diffusion of Dy, Tb and Ce in the Dy - rich magnets. d) Dy and Tb diffusion in the Dy - lean magnets.

It can be seen that the coercivity difference is highest at the edges of the magnet at 0 and 8 mm, where the diffusion source, i.e. the RE foil, was located and becomes smaller towards the center of the magnet

at 4 mm. As shown before, the change is positive for Dy and Tb and negative for Ce. It is interesting to compare the measured coercivity of a gradient magnet H_c with the volume average of the coercivity of its slices. This average calculates to

$$\sum_i (V_i * H_{ci}) / V_{tot} \qquad \textbf{4-2}$$

where V_i is the volume of slice i, V_{tot} is the total volume of the sample and H_{ci} is the coercivity of slice i. The measured value is always higher for Dy and Tb and lower for Ce than the average (Table 4-2). This shows that in a gradient magnet the coercivity, i.e. the amount of diffusing RE, is used more efficiently than in homogeneous magnets.

Table 4-2: Comparison between the measured coercivity from Figure 4-11 with the volume average of the cut slices from Figure 4-14.

$\mu_0 * H_c$ / (T) measured / Vol. average	Diffused RE		
	Dy	Tb	Ce
1.5 h	2.02 / 1.92	2.08 / 2.07	1.75 / 1.65
10 h	2.25 / 2.17	2.53 / 2.48	1.60 / 1.49

The two distinct diffusion regions stated in chapter 4.1.4 can also be found in Figure 4-14: A surface region with very high values of H_c and a thickness of about 500 µm, and adjacent the bulk of the magnet with intermediate H_c values. As an observation, the diffusion processes seem to be very much dependent on surface quality and the nature of the contact between diffusion source and magnet. This is why the amount of RE at the surface, and therefore the coercivity, is hard to control precisely. Also, the amount of diffusing RE, in this case the foil thickness, is heavily influencing the coercivity at the surface, as was shown before [Nakamura2011]. Finally, it is difficult to measure the coercivity or RE concentration at the immediate surface. Because of these reasons the data points at the edges of the magnet have been omitted from the following diffusion constant calculations.

For the chosen experimental setup the diffusion occurs from both sides. Therefore equation 2-16 has to be modified with a second term to include the diffusion in the opposite direction. It starts at x = 8 mm (the sample length):

$$H_c(x,t) = 2H_{c,surf} - \left(H_{c,surf} - H_{c,bulk}\right) \cdot \left[erf\left(\frac{x}{\sqrt{4D_{Dy}t}}\right) + erf\left(\frac{-x+0.8}{\sqrt{4D_{Dy}t}}\right)\right] - H_{c,bulk} \qquad \textbf{4-3}$$

To determine the diffusion coefficients, each 1.5 h profile in Figure 4-14 has been fitted to equation 4-3. The least - squares fit gives values for D_{gb} (Table 4-3). D_{gb} for Dy in the Dy - lean magnet agrees well with the previous chapter, where a value of $7.90 \cdot 10^{-7}$ cm^2/s was obtained for 900 °C.

Table 4-3: Grain boundary diffusion coefficients D_{gb} for Dy, Tb and Ce at 900 °C, obtained from fit curves in Figure 4-14. Note that for the fit the data points close to the surface have been omitted in order to exclude effects of bulk diffusion from the surface.

[T = 900 °C]	Dy - lean Nd-Fe-B		Dy - rich Nd-Fe-B		
Rare Earth	Dy	Tb	Dy	Tb	Ce
D_{gb} in [cm^2/s]	8.45 ± 1.10 $\cdot 10^{-7}$	1.23 ± 0.84 $\cdot 10^{-6}$	1.11 ± 0.15 $\cdot 10^{-6}$	2.92 ± 0.70 $\cdot 10^{-6}$	9.00 ± 0.71 $\cdot 10^{-7}$

When comparing the two different magnet classes one observes that Dy and Tb diffuse slower in the Dy - lean than in the Dy - rich samples. This could be an effect of the different chemistry, i.e. a different composition of the grain boundary phase with a different melting point. Also, the grain size of both magnets was evaluated geometrically with a line intersection method under a light microscope and found to be slightly smaller in the Dy - lean magnets (Figure 4-15). This will have an effect on the diffusion speed, although further studies are needed to determine the exact influence.

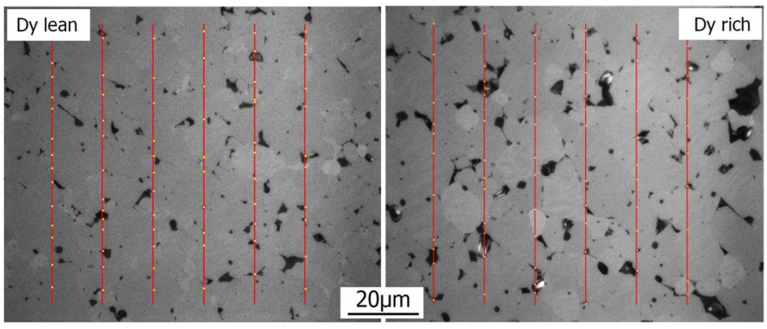

Figure 4-15: Grain size determination in Dy lean and Dy rich sample magnets with a line intersection method in the light microscope according to ASTM E 122. The average line intersection length, i.e. the grain size, is 8.3 µm and 9.1 µm, respectively.

In both magnet classes Tb diffuses significantly faster than Dy. One reason might be the lower melting temperature of the former (Tb: 1356 °C; Dy: 1407 °C), which also leads to lower melting temperatures of a Tb-Nd mixed phase, compared to Dy-Nd (Figure 4-16).

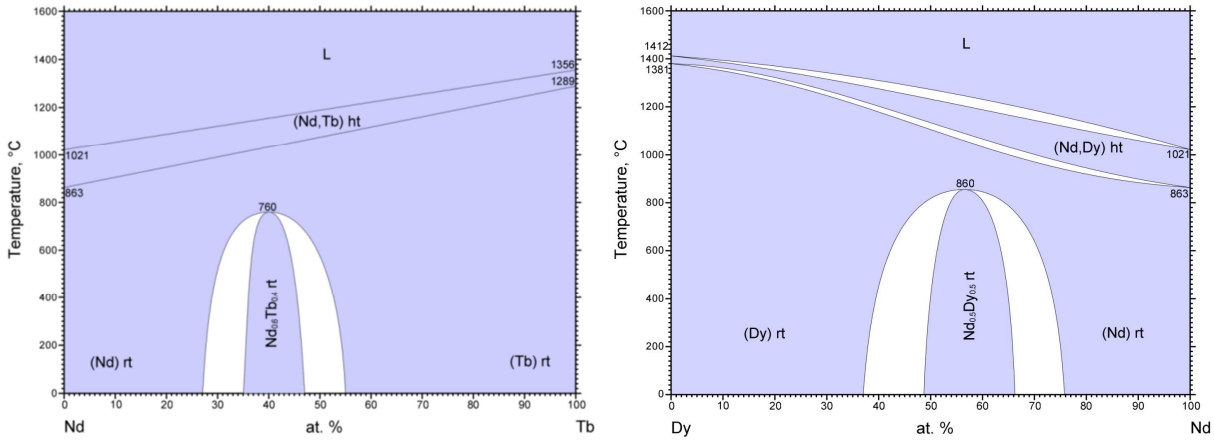

Figure 4-16: Phase diagrams for Nd-Tb and Nd-Dy [Predel1995, Predel1996]

This fact might accelerate the formation of a liquid grain boundary phase and therefore the diffusion. The described difference in diffusion speed between Dy and Tb is higher in the Dy - rich samples, which indicates the important influence of the magnets chemistry. On the other hand, Ce diffuses slower than Dy, although it has by far the lowest melting point (795 °C). However, previous publications [Herbst2012, Huang2015] and own uncited works suggest that the addition of Ce is drastically changing the phase relations in the Nd(+Ce)-Fe-B system. This assumption is supported by the lack of (Nd,Ce)-Fe-B shells on the surface of Ce diffused magnets (Figure 4-17).

Finally, the 10 h coercivity profiles in Figure 4-14a-c) were fitted with equation 4-3 and the D_{gb} determined from the 1.5 h profiles. The fit shows a very good match with the measured data points. The fact that Tb diffuses faster than Dy has direct practical consequences for the GBDP, because it enables the production of thicker diffusion - treated magnets. For example, when comparing Figure 4-14 b) and c), after only 1.5 h Tb has already reached the center of the magnet at x = 4 mm, whereas Dy has not yet affected the coercivity there.

4.2.2. Microstructural analysis

High resolution BSE SEM images of microstructures 50 µm away from the surface of the samples are presented in Figure 4-17. For all HRE, including Gd, the well - known core - shell structures are clearly visible [Loewe2015, Samardzija2012]. These structures form in the first few 100 µm and comprise a $(RE,Nd)_2Fe_{14}B$ mixed phase surrounding $Nd_2Fe_{14}B$ grain cores. In contrast, no shells are visible for the Ce sample with dimensions resolvable by SEM.

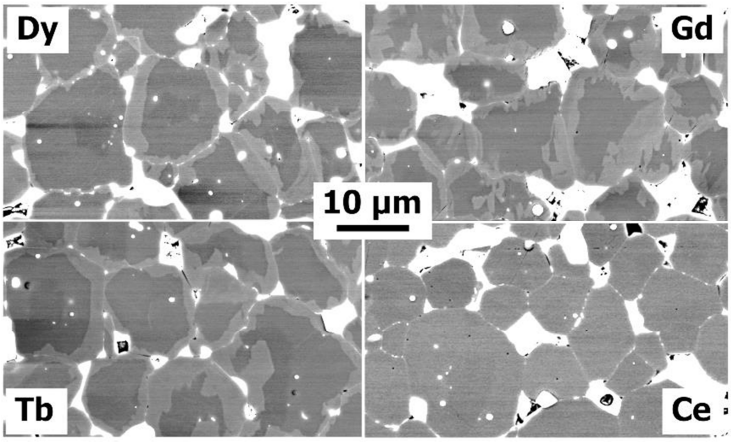

Figure 4-17: BSE SEM images in backscattered electron contrast of the immediate surface regions of the diffusion treated samples. The formation of HRE rich "shells" around the Nd-Fe-B grains is clearly visible for the Gd, Dy and Tb. Ce shows no shell formation, and therefore no formation of a (Nd,Ce)-Fe-B phase.

This finding was confirmed with EDX mapping of the surface of the Ce sample (Figure 4-18). Shown are elemental distributions for Ce, Nd and O. In the Ce L_α map one can clearly see the Ce source (i.e. foil) on the right and Ce accumulation between the grains. The circles indicate a phase with high Nd and O / low Ce content and the boxes a phase with high Ce / low Nd content. This shows that Ce can be preferably found mixed with Nd, but not in the Nd - oxides. Within the grains no Ce can be detected. This was confirmed with two point scans (Figure 4-18, bottom left), one on the pure Ce foil (A) and one on the grain next to the foil (B). Highlighted in the respective EDX spectra are the two prominent Ce L_α and Nd L_α lines (Figure 4-18, bottom right). No Ce L_α peak was observed in the grain.

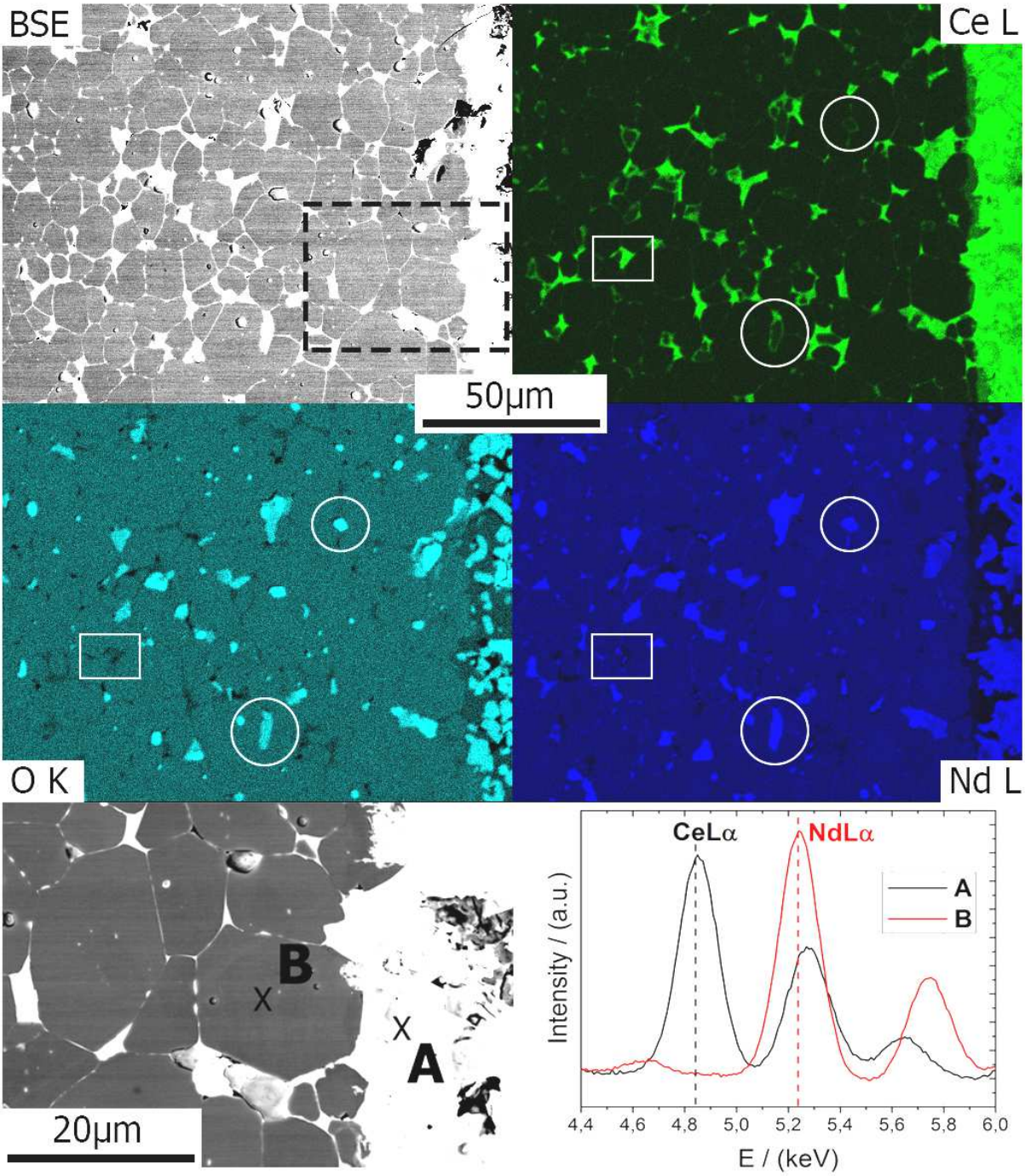

Figure 4-18: EDX maps and point scans from the surface region of the Ce sample. Shown are the investigated region (top left BSE SEM image) and the respective elemental distributions for Ce, Nd and O. The Ce source is on the right. Indicated with a dashed box in the BSE image is the magnified region (bottom left), where two point scans (bottom right) were taken. The circles and boxes indicate different phases.

The formation of the shells was explained before by Seelam *et al.* as partial melting of the surface due to a surplus of RE, in accordance with published Nd-Fe-B phase diagrams [Malfliet2008, Seelam2014]. An assumption made here for the thermodynamic calculations is the equivalency of all the RE present in the magnet, in this case Nd, Pr, Dy. Since Ce - rich shells (i.e. a $(Nd,Ce)_2Fe_{14}B$ phase) are not observed, it means that this assumption does not hold for Ce. Another explanation could be that the cooling rate of the Nd-Ce-Fe-B melt on the outside of the grains was not high enough (the magnets were cooled from 900 °C to RT in approx. 10 min). This way the Ce had time to segregate in front of the crystallizing Nd-Fe-B and got pushed into the grain boundaries and Nd - rich secondary phases. This seems more plausible, since some degree of interaction of Ce with the $Nd_2Fe_{14}B$ - phase is likely to occur, as evidenced by the much decreased coercivity.

Figure 4-19 shows a grain boundary (GB) in a Tb diffused sample located about 800 µm away from the surface. A STEM EDX map and the corresponding profile across the GB reveals the distribution of the most prominent elements. In the vicinity of the grain boundary an enrichment of Tb, Ga and Cu is clearly visible as well as a depletion of Fe. This evidences the diffusion of Tb along the GB. The lateral spread of the Tb signal is about 25 nm. It cannot be concluded with certainty whether this spread stems from the diffusion of Tb atoms from the GB into the lattice of the $RE_2Fe_{14}B$ phase or if it is due an inclination of the GB with respect to the projection direction. However, since the magnetic properties of the sample did change drastically in the investigated region, a substitution of Tb atoms against Nd in the $RE_2Fe_{14}B$ phase has likely occurred, at least in a thin outer layer. The evaluation of the Dy-L_β peak showed that Dy, which was already present in the initial sample before the GBDP, is fairly homogeneously distributed. In contrast, the evaluation of the Dy-$M_{\beta\alpha}$ peak in the same region indicates a slight enrichment along the GB. However, this might be an artifact due to the heavy overlap with the Tb-M_α peak.

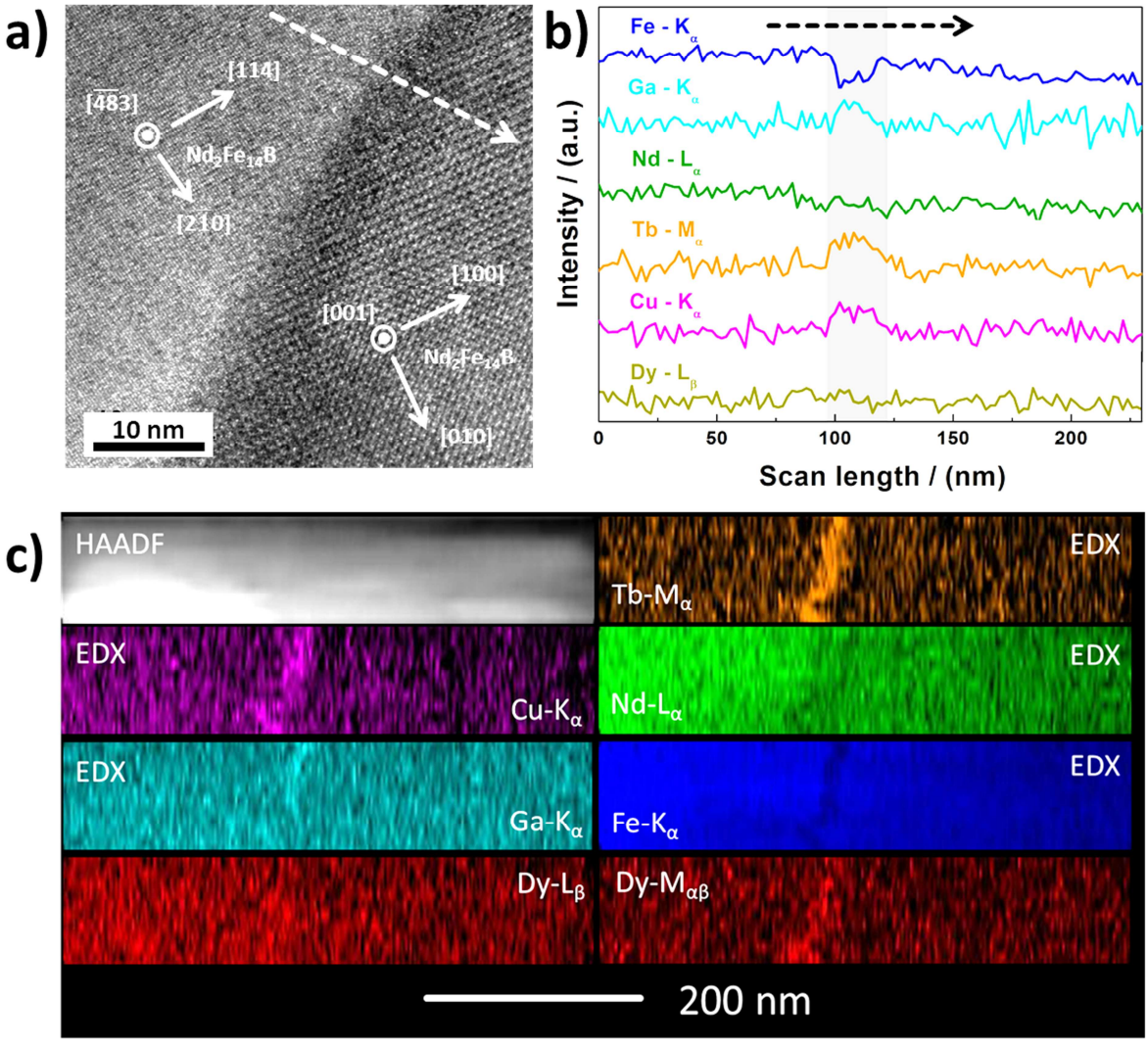

Figure 4-19: A grain boundary (GB) in a sample diffused with Tb, located approximately 800 µm away from the surface. a) HRTEM image. b) STEM EDX line scan with most prominent elements. c) 2D STEM EDX maps of the GB. An enrichment with Tb is clearly visible. *Help with the TEM analysis by C.Kübel (Karlsruhe Institute of Technology) is gratefully acknowledged.*

4.2.3. Micromagnetic analysis of grain boundary diffusion processed samples

The following chapter investigates how the change in coercivity after the GBDP reflects in the phenomenological micromagnetic parameters of the Kronmüller equation (equation 2-8). For simplicity the two parameters α_K and α_ψ were combined in a single "grain surface parameter" α, so that the equation becomes

$$H_c = \alpha * H_a - N_{eff} * M_s \quad \text{4-4}$$

To determine the Kronmüller parameters it is necessary to measure the magnetic properties contained in the equation for various temperatures, plot H_c/M_s vs H_a/M_s and fit the data with a linear function *f*. The slope of *f* gives α and the ordinate intercept y(x=0) gives N_{eff}. For the investigation three magnets were chosen as samples: the untreated Dy - rich reference material and the same material after GBD with Tb as well as Ce (cf. Figure 4-11). All measurements were performed with specimen cut from spots 1 mm away from the surface of the samples. i.e. that no thick (Nd,RE)-Fe-B shells were present in the microstructure. The temperature dependent H_c and M_s were determined in a VSM in fields up to ±2 T (Figure 4-20).

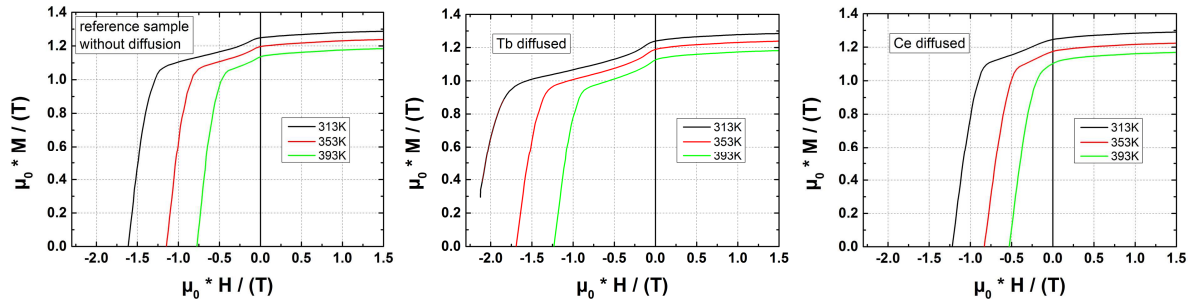

Figure 4-20: Demagnetization curves of VD837 reference magnets before and after GBDP with Ce and Tb. All measurements were performed with a VSM.

The summarized results can be found in Figure 4-21 and Table 4-4.

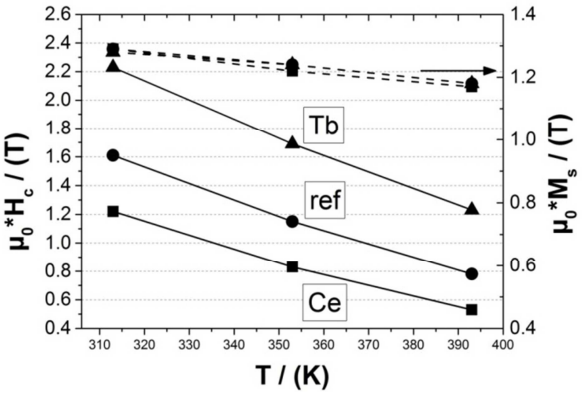

Figure 4-21: Summarized magnetic properties of the VD837 reference magnets before and after GBDP with Ce and Tb. All measurements were performed with a VSM (cf. Figure 4-20).

As expected, the diffusion does not significantly change the saturation magnetization of the samples but is increasing the coercivity for Tb and lowering it for Ce diffusion, respectively. In the chosen temperature interval of 313 - 393 K the decrease in both properties is almost linear.

Table 4-4: Magnetic properties of the Dy - rich reference magnets before and after GBDP with Ce and Tb.

	$\mu_0 * M_s$ / (T)			$\mu_0 * H_c$			$\mu_0 * H_a$		
T / (K)	Ref	Ce	Tb	Ref	Ce	Tb	Ref	Ce	Tb
313	1.29	1.29	1.29	1.61	1.22	2.23	8.92	8.51	8.87
353	1.24	1.22	1.24	1.15	0.84	1.69	7.57	7.33	7.39
393	1.18	1.17	1.18	0.78	0.53	1.23	6.20	6.10	6.18

The anisotropy fields were determined with the singular point detection (SPD) method. Exemplary, the results of the Tb diffused sample are depicted in Figure 4-22, the complete values for H_a can be found in Table 4-4. At 313 K the values for the reference magnet before and after the Tb diffusion are nearly identical at about 8.9 T. The value for the Ce diffused sample is with 8.5 T only 5 % lower. At 393 K all three values are nearly identical, between 6.1 and 6.2 T. The small differences in H_a are very much in opposition to the H_c values. Here, the difference between the Ce and Tb diffused samples are +80 % and +130 % at 313 K and 393 K, respectively.

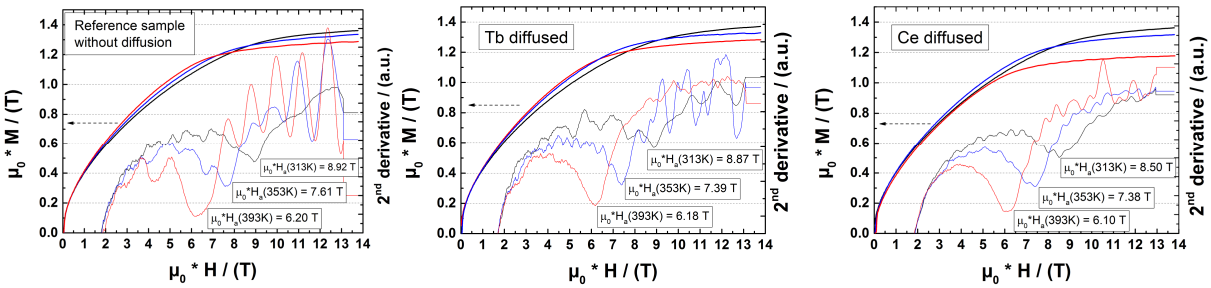

Figure 4-22: Magnetization curves in the hard direction for the reference as well as Ce and Tb diffused Nd-Fe-B magnets (cf. Figure 4-20) for 313 K / 353 K / 393 K. The second derivative of the curves is displayed and from the minima the anisotropy fields $\mu_0 * H_a$ have been determined. The oscillations in the 2nd derivative at higher fields are artifacts that stem from the smoothing algorithm of the digital data plots.

Finally, the Kronmüller plots of the data in Table 4-4 are shown in Figure 4-23. The derived values for α and N_{eff} can be found in Table 4-5.

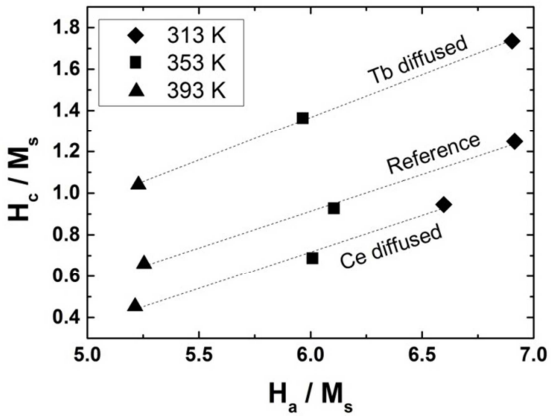

Figure 4-23: Kronmüller plot of the values in Table 4-4. The parameters α and N_{eff} are the slope and the y(x=0) values of the least-squares linear data fits (dashed lines). They can be found in Table 4-5.

As expected, after the Tb GBDP there is a significant increase of the α parameter compared to the reference sample. The reason is likely the magnetic hardening of the grain surface through the Tb-Nd substitution and the impeded nucleation of reversed domains; also a reduction in defect density caused by the diffusion is possible. The situation is different for Ce diffusion. Here, the α parameter is nearly unchanged, which indicates that Ce does not interact with the $Nd_2Fe_{14}B$ - phase as the HRE Tb. This statement is supported by the microstructure observations in Figure 4-17, which showed no thick (Nd,Ce)-Fe-B shells. After Tb diffusion the N_{eff} parameter is not significantly changed, which was expected because in the bulk of the magnet the microstructure before and after the GBDP is rather similar. Neither the grain size or shape did change after the diffusion. After Ce diffusion N_{eff} is slightly increased. Since the grain size did not change significantly, this indicates higher stray fields of nonmagnetic secondary phases. These might be the pure Ce inclusions formed after the GBDP shown in Figure 4-18 (boxes).

Table 4-5: Kronmüller parameters α and N_{eff} derived from Figure 4-22.

	Neff	α
Tb diffused	1.12 ± 0.07	0.41 ± 0.01
Reference	1.21 ± 0.15	0.35 ± 0.02
Ce diffused	1.40 ± 0.23	0.35 ± 0.04

5. Production of sintered (Nd,Dy)-Fe-B magnets with heterogeneous microstructure through powder blending

As described in chapter 2.3, the production of sintered (Nd,Dy)-Fe-B magnets by blending with binary Dy-X based powders has a number of disadvantages, namely high sintering temperatures, the introduction of unwanted elements into the compound as well as a compositional shift of the ϕ - phase. To overcome these problems, in this work the Dy - rich ϕ - phases (Nd,Dy)-Fe-B and Dy-Fe-B-X are used as AP. The advantages of adding ϕ - phase are

- no additional harmful elements like F, O or S introduced into the magnets
- However, if needed one can easily introduce wanted light elements (Co, Ga, Al, Cu…) with the AP
- The composition is not shifted to higher RE contents, because Nd, Fe and B are introduced together with the HRE
- The first AP can be added in large quantities, theoretically up to 100%
- The melting temperature of the (Nd,Dy)-Fe-B ϕ - phase does not increase much with increasing Dy content (Figure 5-1).

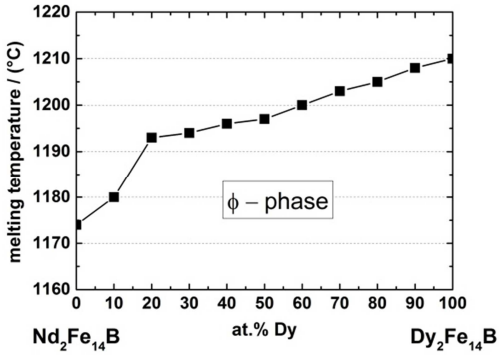

Figure 5-1: Melting temperature of the (Nd,Dy)-Fe-B ϕ - phase in dependence of Dy content [Grieb1989].

A possible way to accelerate the melting of the AP particles is to produce them smaller than the BP. This way the surface to volume ratio is increased, which favors a faster melting. This effect is not explored in the cited literature and will be utilized in the upcoming experiments.

The following chapter is divided into three parts. First, sintered magnets are produced from a single powder (chapter 5.1). This serves to evaluate the sintering process and to produce reference magnets for the blending process. Secondly, the production of sintered Nd-Fe-B magnets by blending two powders is described (chapter 5). In the last part the temperature stability of the Dy - rich shells is investigated (chapter 5.3).

For the here described blending process a patent application has been filed. Grant and internationalization is pending as of October 2016. (file number 10 2015 107 486.9 / PCT file number PCT/EP2016/060633).

5.1. Production of sintered magnets from a single powder

5.1.1. Comparison of commercial magnets with magnets produced from their precursor powder

In order to evaluate the sintering process (without powder production steps) magnets were produced with a commercial Nd-Fe-B powder from Vacuumschmelze GmbH & Co. KG and compared to the industrially produced magnets of the same composition ("VD722"). The powder specifications are listed in Table 5-1. The employed process route is described in chapter 3.1.2.

Table 5-1: Specifications of commercial Nd-Fe-B powder for production of test magnets as provided by Vacuumschmelze GmbH & Co. KG.

d50 / µm	total RE / wt.%	Co / wt.%	B / wt.%	Fe / wt.%	Al / wt.%	Cu / wt.%	Ga / wt.%
5.1	30.2	2.0	0.91	bal	traces	traces	traces

The demagnetization curves of both magnets are shown in Figure 5-2. The coercivities are the same, demonstrating that the proper PSA was applied. The remanence is slightly lower (1.41 T vs. 1.36 T) due to the different compaction methods. The commercial magnet was isostatically and the produced magnet transversally pressed, leading to a reduction of the degree of orientation of the powder particles. The worse rectangularity is most likely due to more impurities being picked up during the production process, leading to a less homogeneous coercivity distribution within the magnet. All in all, the properties of both magnets are qualitatively comparable. This proves that with the established sintering process very good magnets can be produced on a laboratory scale.

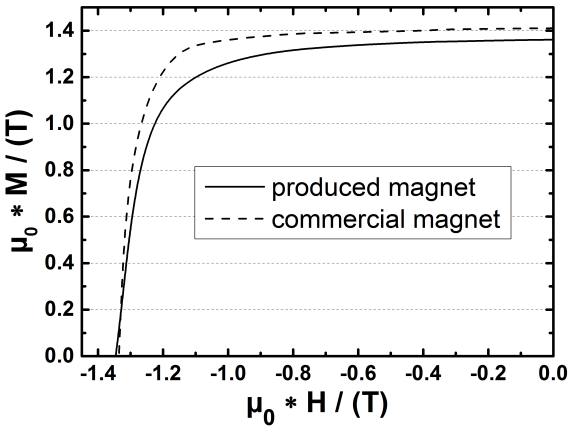

Figure 5-2: Demagnetization curves of a produced magnet prepared from commercial Nd-Fe-B powder and the industrially produced magnet of the same composition.

5.1.2. Production of reference magnets for the powder blending process

Magnets with the nominal compositions $Nd_{15}Fe_{79}B_6$ and $(Nd_{90}Dy_{10})_{15}Fe_{79}B_6$ were produced with the synthesis route described in chapter 3.1.2. The latter serves as reference for magnets with the same composition, but produced by powder blending, and will be called “homogeneous” magnet. Sintering temperature for both compositions is 1050 °C, followed by PSA at 750 °C and 510 °C. The magnetic properties are shown in Figure 5-3 and Table 5-2.

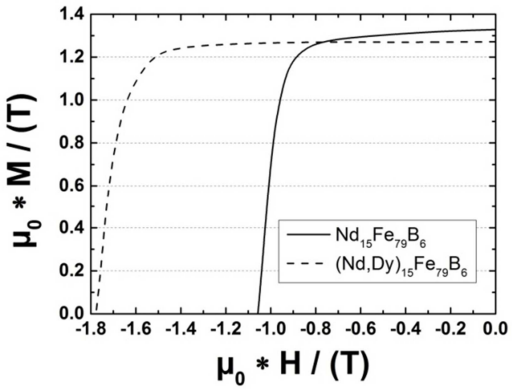

Figure 5-3: Demagnetization curves of the produced magnets with 0 at.% and 1.5 at% Dy addition.

Table 5-2: Properties of the produced sample magnets with 0 at.% and 1.5 at% Dy addition. μ_0*M(H_a=14 T) is the magnetization value measured at external fields of 14 T, $M_{s,theo}$ the theoretical saturation magnetization and DOT the degree of texture.

[T]	$Nd_{15}Fe_{79}B_6$	$(Nd_{90}Dy_{10})_{15}Fe_{79}B_6$
$\mu_0 * H_c$	1.06	1.78
$\mu_0 * M_r$	1.33	1.27
μ_0*M(H_a=14 T)	1.47	1.43
μ_0*$M_{s,theo}$	1.43	1.36
DOT [%]	92.4	93.4

The theoretical saturation magnetization μ_0*$M_{s,theo}$ for $Nd_{15}Fe_{79}B_6$ can be calculated as follows: out of 100 g of $Nd_{15}Fe_{79}B_6$ one can get 91.88 g of pure $Nd_2Fe_{14}B$ phase before running out of Fe (Nd and B are in a surplus), which corresponds to a volume ratio of 90 vol.%. Multiplication with the theoretical saturation magnetization of 1.60 T results in μ_0*$M_{s,theo}$ = 1.44 T for a perfectly oriented polycrystalline $Nd_{15}Fe_{79}B_6$ sample. Accordingly, μ_0*$M_{s,theo}$ = 1.36 T for $(Nd_{90}Dy_{10})_{15}Fe_{79}B_6$, assuming an ideal mixture of anisotropy fields [Herbst1991]. The magnetization in easy direction for both magnet compositions has been measured up to applied fields of μ_0*H_a = 14 T (Figure 5-4). The measured values are μ_0*M(H_a=T) = 1.47 T and 1.43 T for $Nd_{15}Fe_{79}B_6$ and $(Nd_{90}Dy_{10})_{15}Fe_{79}B_6$, respectively. According to literature [Fernengel1996, Kneller1962] the para - effect at room temperature accounts for 2.5% of the measured magnetization. The effect describes the thermal disalignement of ferromagnetically ordered spins at finite temperatures, which are partially aligned again in high magnetic fields. Subtracting the 2.5% from the μ_0*M(H_a=14 T) value one arrives at 1.43 T and 1.39 T, respectively, which are almost exactly the calculated μ_0*$M_{sat,\ theo}$ values.

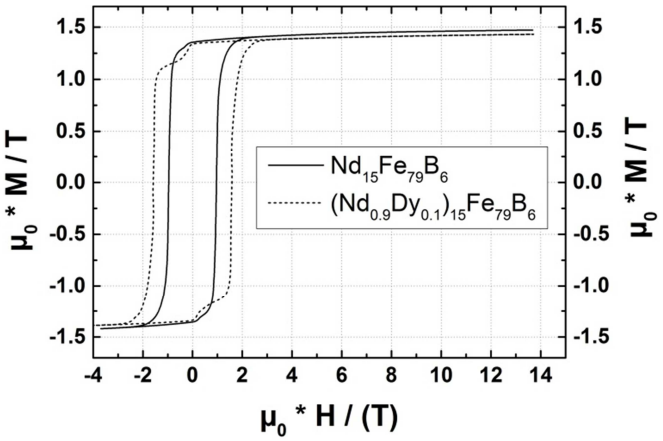

Figure 5-4: Hysteresis loops of the produced magnets with 0 at.% and 1.5 at% Dy addition measured in easy direction up to 14 T. The step in the dashed line is a measurement artifact caused by the small sample size.

In this work the degree of texture (DOT) is defined as the ratio of remanence to saturation magnetization. For both samples it is 92.4% and 93.4%, respectively. The values are typical for transversally pressed Nd-Fe-B sintered magnets.

Impurity levels in the two produced magnets compared to a commercial reference magnet were determined with an ONH836 and an RC612 Elemental Analyzer (LECO Corporation). The absolute concentrations of O, N, H and C can be can be found in Table 5-3. The measurements for ONH and C were each repeated 3 times and the average was determined. The values for all samples are similar, which is an indication of the high quality of the produced magnets.

Table 5-3: Impurity concentrations in the two produced reference magnets compared with a commercial reference magnet (Material 2, "VD837", Vacuumschmelze GmbH & Co. KG). *The CONH analysis was conducted by A. Grünewald at the Fraunhofer IWKS, Hanau.*

[m.%] ± %	**O**	±	**N**	±	**H**	±	**C**	±
VD837 TP	0.25	2	0.009	15	<0.001	N.A.	0.06	15
$Nd_{15}Fe_{79}B_6$	0.18	<1	0.016	11	0.002	27	0.08	3
$(Nd_{0.9}Dy_{0.1})_{15}Fe_{79}B_6$	0.33	3	<0.001	N.A.	<0.001	N.A.	0.10	1

The microstructure of both magnets is displayed in Figure 5-5. The grain size is similar and about 5 - 10 µm. The network of the very thin grain boundaries is nicely developed, as can be seen by the faint white lines between the grains. Several Nd - rich triple point phases can be distinguished by their different contrast.

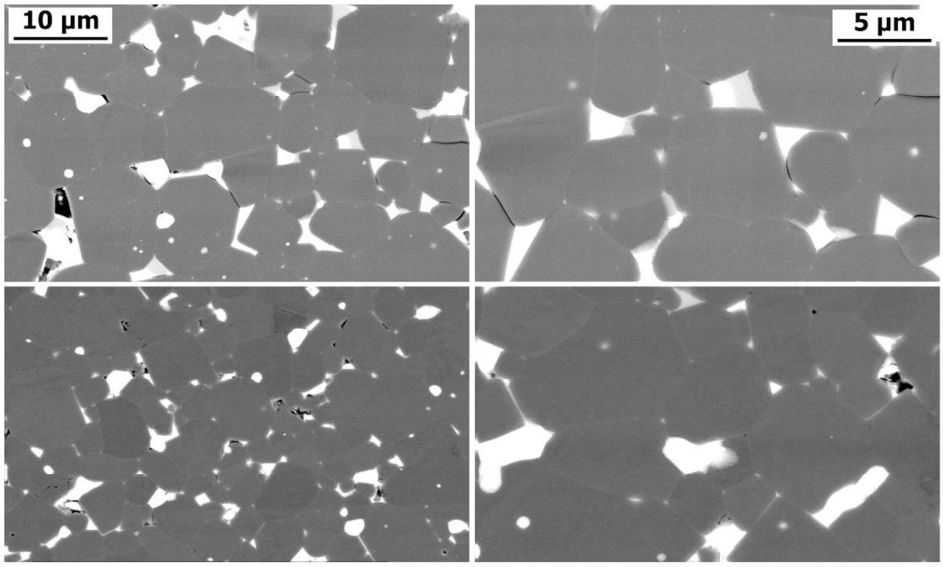

Figure 5-5: BSE SEM images of $Nd_{15}Fe_{79}B_6$ (top) and $(Nd_{0.9}Dy_{0.1})_{15}Fe_{79}B_6$ (bottom) produced from homogeneous pre - alloys.

The composition of the overall magnets and the ϕ - phases were determined by standardless EDX quantification, i.e. the sum of the concentrations of Dy, Nd and Fe is normalized to 100% (Table 5-4). Since other elements like B, Si (from polishing) or O are excluded, the values must only be regarded relative to each other and not as absolute.

Table 5-4: Elemental compositions in the produced magnets determined by standardless EDX.

nominal	$Nd_{15}Fe_{79}B_6$		$(Nd_{0.9}Dy_{0.1})_{15}Fe_{79}B_6$	
[at%]	ϕ - phase	overview	ϕ - phase	overview
Dy M	0.0	0.0	1.8	1.9
Nd L	13.6	16.0	12.5	14.9
Fe K	86.4	84.0	85.7	83.2

5.2. Production process of sintered magnets by blending two powders

5.2.1. Production of the pre - alloys

The goal for the production of the AP is a high purity ϕ - phase and as little as possible undesired secondary phases like e.g. $DyFe_x$. For this reason the following different production methods and compositions were examined:

1) Dy-Fe-B; homogenized, suction - cast and melt - spun
2) Dy-Fe-B-Cu_x
3) (Nd,Dy)-Fe-B

1) Dy-Fe-B

The composition of the AP pre - alloy was chosen to be $Dy_{15}Fe_{79}B_6$. This way, the elemental ratios are the same as in the $Nd_{15}Fe_{79}B_6$ BP, which facilitates the blending process. As a first step, the pre - alloy was inductively molten and homogenized under protective athmosphere. The homogenization temperature of 1120 °C was selected to be in the "L + ϕ" region of the quasi - binary phase diagram in Figure 5-6. The stoichiometry on the right axis of the diagram ($Dy_{18.5}Fe_{75}B_{6.5}$) is close to the actual one, therefore it should allow for qualitative correct phase predictions.

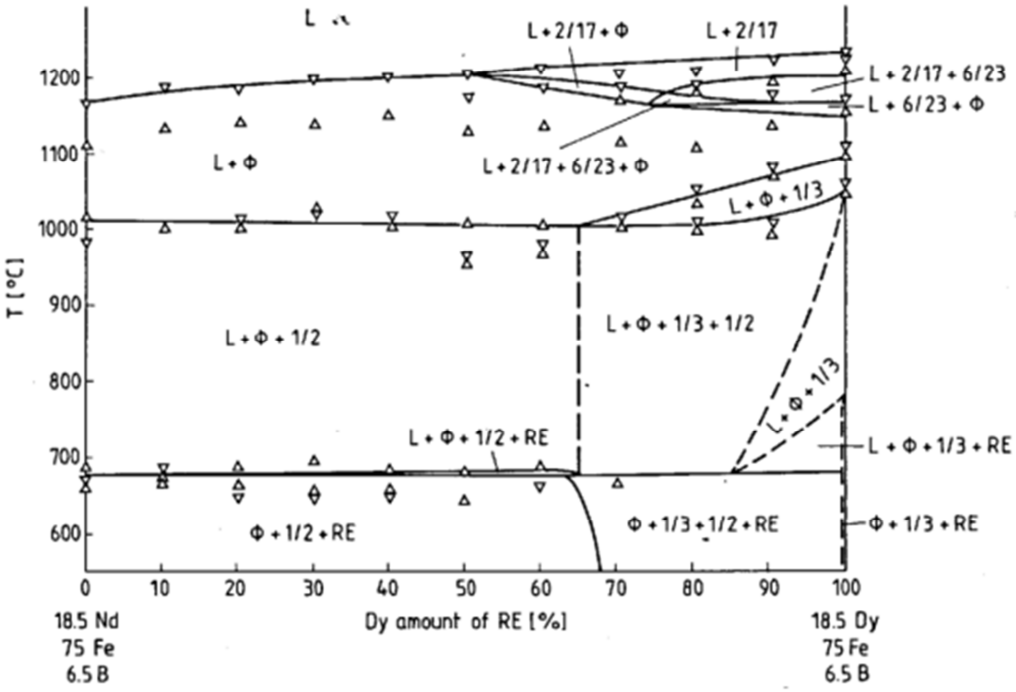

Figure 5-6: Quasi - binary phase diagram of the (Nd,Dy)-Fe-B system [Fritz1992].

Figure 5-7 shows BSE SEM images of the microstructure after the homogenization. Two different homogeneous phases ("Dy","ϕ") and one phase mixture ("$DyFe_x$") can be distinguished.

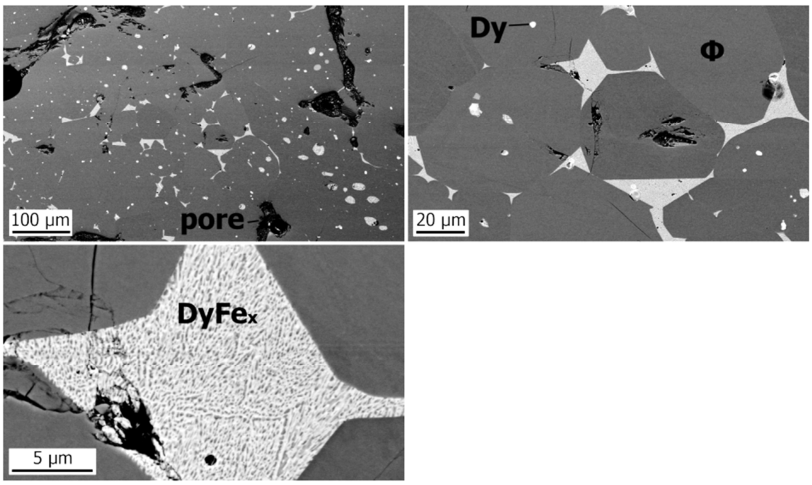

Figure 5-7: BSE SEM images of $Dy_{15}Fe_{79}B_6$, homogenized for 3 days at 1120 °C. The complete EDX results for all phases can be found in Table 5-5.

With EDX (Table 5-5) and XRD (Figure 5-9) the main phase is determined to be the $Dy_2Fe_{14}B$ ϕ - phase. The small white spots contain only Dy. However, with XRD Dy_2O_3 has been identified. It is unclear if the oxide is really present in the magnet or if the oxidation is merely an artifact of the XRD sample preparation. Region "$DyFe_x$" is a mixture of very finely distributed phases, with an average elemental ratio of about Dy : Fe = 4 : 1. Most probably it contains e.g. $DyFe_3$ or Dy_6Fe_{23}. Both phases are ferromagnetic and supposed to have a negative influence on the magnetic properties of (Nd,Dy)-Fe-B sintered permanent magnets [Fritz1992]. In order to suppress the formation of said phases, suction casting and melt - spinning of the same alloy were employed in the following.

Table 5-5: Chemical composition of the different phase in Figure 5-7 and Figure 5-10, as determined by EDX.

composition	phase	Dy	Fe	Cu
$Dy_{15}Fe_{79}B_6$	ϕ	10,0	90,0	N/A
	"$DyFe_x$"	20,1	79,9	N/A
	Dy	100,0	0,0	N/A
$Dy_{15}Fe_{79}B_6Cu_2$	ϕ	11,4	88,3	0,3
	"$DyFe_x$"	94,2	0,0	5,8
$Dy_{15}Fe_{79}B_6Cu_5$	ϕ	10,2	89,2	0,6
	"$DyFe_{x1}$"	27,4	0,0	72,6
	"$DyFe_{x2}$"	25,4	0,0	74,6
$Dy_{15}Fe_{79}B_6Cu_{10}$	ϕ	9,6	88,4	2,0
	grey phase	10,0	87,5	2,5
	"$DyFe_{x1}$"	22,1	0,0	77,9
	"$DyFe_{x2}$"	15,1	0,0	84,9
	Fe	0,0	100,0	0,0

Melt spinning was conducted in a commercial melt - spinner with wheel speeds of 30 m/s. BSE SEM images reveal a homogeneous phase distribution with no secondary phases (Figure 5-8). EDX point scans confirm the composition of the phase to be close to $Dy_{15}Fe_{79}B_6$. The black dots are most likely pores. Suction casting was conducted in a commercial arc melter with vacuum suction option. As was determined by EDX, the microstructure shows Dy-Fe-B ϕ - phase (dark grey) surrounded by white border regions with high Dy content. The microstructure looks similar to strip casted material [Bernardi1998]. In both cases the formation of secondary phases was either suppressed or they are formed in small dimensions which are likely to dissolve fast during sintering.

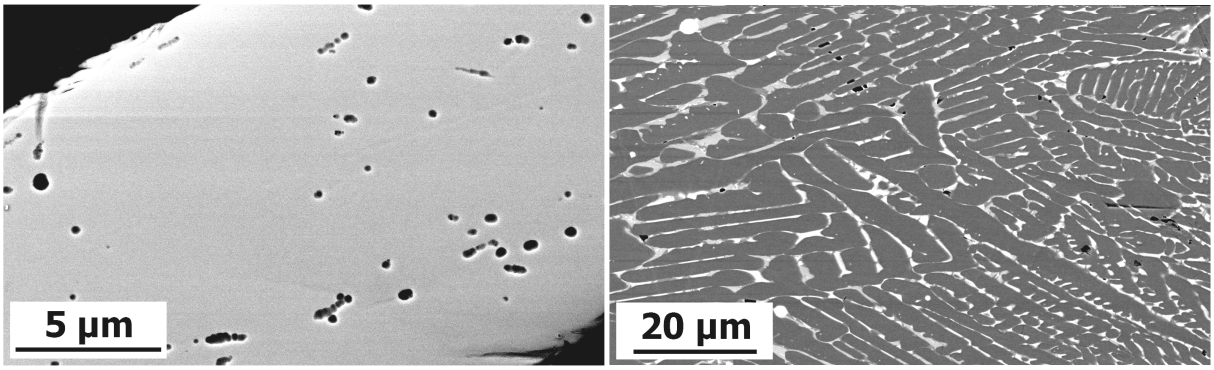

Figure 5-8: BSE SEM images of $Dy_{15}Fe_{79}B_6$ produced by melt spinning (left) and suction casting (right)

XRD spectra of all produced Dy-Fe-B pre - alloys are shown in Figure 5-9. In homogenized and suction - cast samples pronounced peaks of the Dy-Fe-B ϕ - phase appear. As secondary phases $DyFe_x$ compounds and Dy_2O_3 could be identified. The ribbons show only broad and diffuse peaks, indicating that they are amorphous.

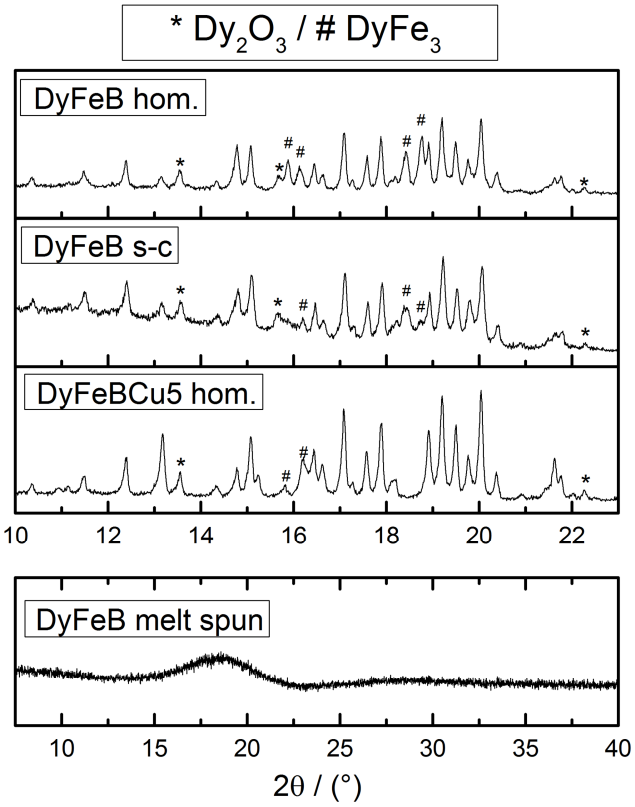

Figure 5-9: XRD spectra of $Dy_{15}Fe_{79}B_6$, either homogenized, suction cast or melt - spun. Also the spectrum of $Dy_{15}Fe_{79}B_6Cu_5$ is shown. All non-marked peaks correspond to the Dy-Fe-B ϕ - phase.

2) Dy-Fe-B-X

To influence the melting behavior of the Dy-Fe-B pre - alloy, common alloying elements were added to produce the following compositions:

- $Dy_{15}Fe_{79}B_6Al_2$
- $Dy_{15}Fe_{79}B_6Ga_2$
- $Dy_{15}Fe_{79}B_6Cu_X$, X = 2, 5, 10

The following paragraph concentrates on the $Dy_{15}Fe_{79}B_6Cu_X$ alloys, and the microstructures for X = 2, 5, 10 are shown in Figure 5-10.

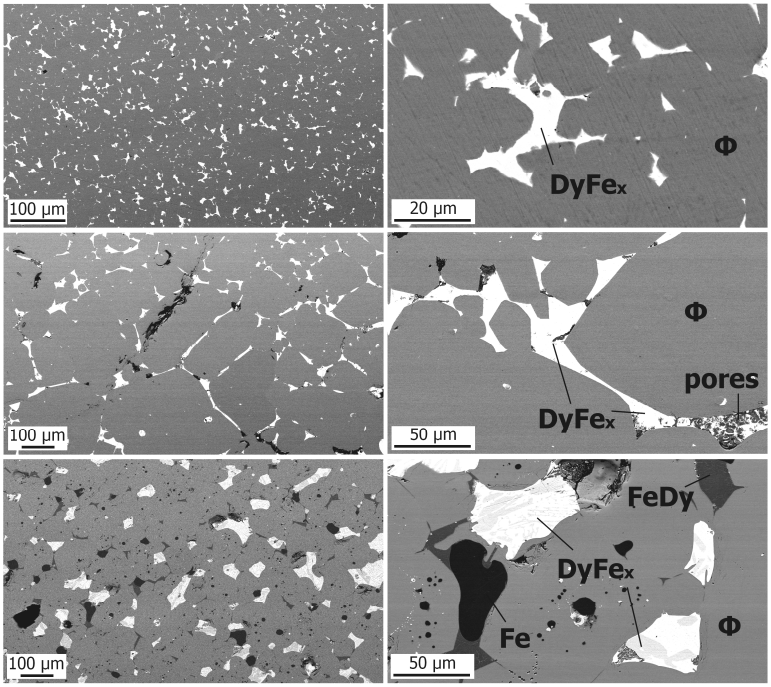

Figure 5-10: BSE SEM images of $Dy_{15}Fe_{79}B_6Cu_2$ (top), $Dy_{15}Fe_{79}B_6Cu_5$ (middle) and $Dy_{15}Fe_{79}B_6Cu_{10}$ (bottom). As determined with EDX, the main phase is the $Dy_2Fe_{14}B$ ϕ - phase with small Cu additions. The complete quantitative EDX results for all phases can be found in Table 5-5.

The microstructures of the compositions with Al and Ga proved to be very inhomogeneous (Figure 5-11), therefore these alloys are not investigated further.

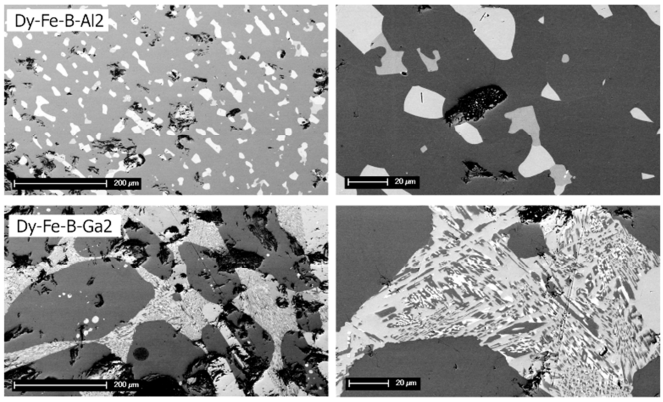

Figure 5-11: BSE SEM images of $Dy_{15}Fe_{79}B_6Al_2$ (top) and $Dy_{15}Fe_{79}B_6Ga_2$ (bottom), homogenized for 3 days at 1120 °C.

With EDX the main phase (grey) of all 3 $Dy_{15}Fe_{79}B_6Cu_X$ alloys was determined to be the $Dy_2Fe_{14}B$ ϕ - phase (Table 5-5), which was confirmed with XRD for the X = 5 sample (Figure 5-9). The Cu content inside the ϕ - phase increased from 0.3 at.% (X = 2) to 2.0 at.% (X = 10). The white secondary phases are all rich in Dy and Cu, and without Fe. In $Dy_{15}Fe_{79}B_6Cu_{10}$ pure Fe and an Fe - rich Dy-Fe-Cu phase appear; the white region consists of pure Dy. The highest phase content of $Dy_2Fe_{14}B$ ϕ - phase is found in $Dy_{15}Fe_{79}B_6Cu_5$, as was determined by image analysis. Regarding these results, $Dy_{15}Fe_{79}B_6Cu_5$ is the most favorable composition of the $Dy_{15}Fe_{79}B_6Cu_X$ alloys and was chosen for further DSC analysis. Selected DSC heating curves of the $Dy_{15}Fe_{79}B_6$ compounds, as well as $Dy_{15}Fe_{79}B_6Cu_5$ are shown in Figure 5-12 and peak positions can be found in Table 5-6. For comparison, the DSC heating curve of $Nd_{15}Fe_{79}B_6$ is also shown.

A peak observed in all alloys is the Curie temperature (T_c) close above 300 °C, except for the melt - spun ribbon, which does not crystallize until above 600 °C. However, in the cooling curve the T_c peak is present (data not shown). $Nd_{15}Fe_{79}B_6$ shows small peaks at 670 and 770 °C (*E* … Eutectic) which are attributed to the melting of Nd - rich phases, possibly also a Nd-Cu eutectic compound with Cu impurities caused by the production process (The Fe was cleaned in an arc melter on a water - cooled Cu plate). The eutectic peak is absent in all Dy-Fe-B compounds, i.e. there is no liquid phase developing during sintering. This supposedly is hindering the formation of a dense magnet body and is therefore increasing the needed sintering temperatures. The eutectic peak is found again in the Dy-Fe-B-Cu alloys, which indicates the formation of a DyCu phase. The $Dy_{60}Cu_{40}$ eutectic composition has a melting temperature of 840 °C, close to the observed peak at 843 - 890 °C [Raghavan2010]. All Dy-Fe-B related phases show peaks close above 1100 °C (*X*), which are attributed to the melting of $DyFe_x$ compounds. Finally, the ϕ - phase is melting above 1200 °C (ϕ). In $Nd_{15}Fe_{79}B_6$ there is a single sharp peak at 1201 °C.

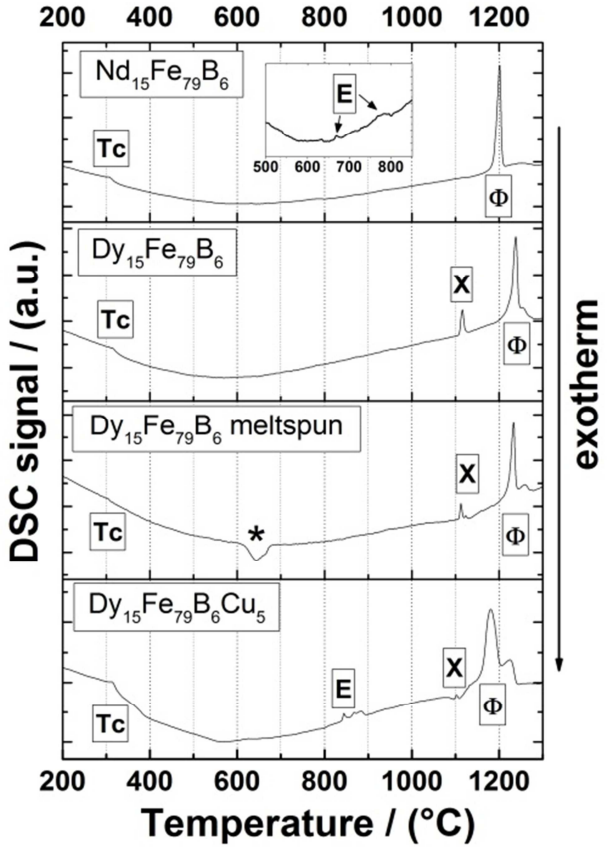

Figure 5-12: DSC heating curves of selected $Dy_{15}Fe_{79}B_6$ compounds, as well as $Dy_{15}Fe_{79}B_6Cu_5$. Nd-Fe-B is shown for comparison. The marked peaks correspond to the Curie-Temperature (Tc), crystallization (*), melting of a Nd - or Dy - rich eutectic phase (E), melting of an unidentified Dy compound, possibly $DyFe_x$ (X), melting of the ϕ - phase (ϕ). *The DSC analysis was conducted by C. Fasel, TU Darmstadt.*

In $Dy_{15}Fe_{79}B_6$ this peak shifts to higher temperatures and also there is a second melting peak observable at 1238 °C and 1255 °C, respectively. Through the addition of Cu the peaks *E* and ϕ are shifted to lower temperatures.

Table 5-6: Position of DSC peaks for different AP in °C, heating regime. All peaks are endothermic, except for the crystallization peak. The peaks correspond to Curie - temperature (Tc), crystallization (*), melting of a Nd- or Dy - rich eutectic phase (E), melting of an unidentified Dy compound, possibly DyFex (X), melting of the ϕ - phase (ϕ).

[°C]	T_c	E	* crystallization	X	ϕ
$Nd_{15}Fe_{79}B_6$	308	667/≈770	-	-	1201
$Dy_{15}Fe_{79}B_6$	314	-	-	1116	1238/1255
$Dy_{15}Fe_{79}B_6$ meltspun	-	-	615-675	1113/1124	1234/1259
$Dy_{15}Fe_{79}B_6Cu_2$	313	854	-	1143	1218/1252
$Dy_{15}Fe_{79}B_6Cu_5$	314	843-890	-	1102	1181/1225

In summary, for Dy-Fe-B compounds, DSC measurements show no sign of a liquid phase transition during heating to sintering temperature. This is likely to hinder the liquid phase sintering process. The melting point of the ϕ - phase is shifted to higher temperatures, compared to Nd-Fe-B. In contrast to Dy-Fe-B compounds, in the Dy-Fe-B-Cu sample a pronounced eutectic melting peak is visible. Also the melting of the ϕ - phase is shifted to significantly lower temperatures.

3) (Nd,Dy)-Fe-B

The composition of the AP was chosen to be $(Nd_{0.725}Dy_{0.275})_{15}Fe_{79}B_6$, because for the given amount of Dy the microstructure of the pre - alloy after homogenization looks very similar to the microstructure of the ternary $Nd_{15}Fe_{79}B_6$ pre - alloy. With EDX it was confirmed that the grey main phase is the ϕ - phase (Dy/Nd = 42.5 at.%; nominal 37.9 at.%) and the white regions consists of $Dy_{5.3}Nd_{69.1}Fe_{25.7}$ (at.%).

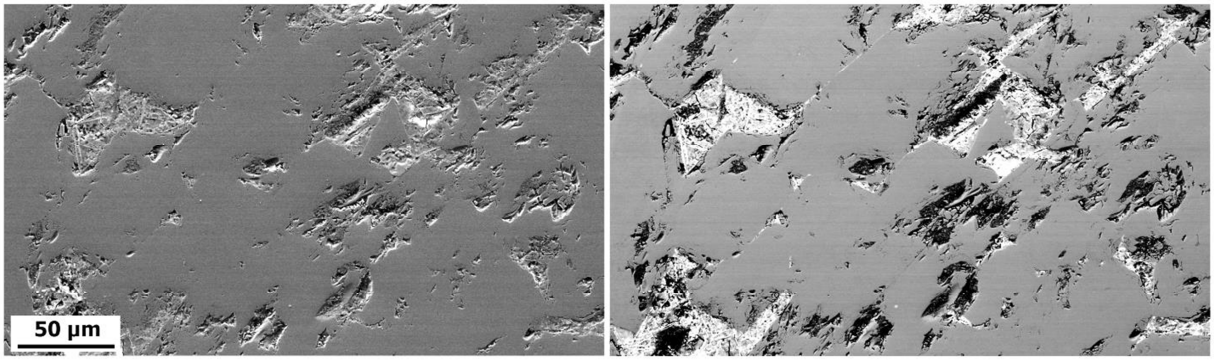

Figure 5-13: SEM images of $(Nd_{0.725}Dy_{0.275})_{15}Fe_{79}B_6$ after homogenization at 1120 °C for 48 h. SE (left) and BSE (right) contrast.

DSC heating curves (Figure 5-14) of $(Nd_{0.725}Dy_{0.275})_{15}Fe_{79}B_6$ show a very pronounced melting peak at 667 °C and 770 °C (Table 5-7), which is attributed to the melting of eutectic Nd,Dy - rich phases. The molten phase is favorable for enabling the liquid phase sintering and is most likely the reason for the later found much decreased sintering temperatures. The melting of the ϕ - phase is shifted up from 1201 °C in $Nd_{15}Fe_{79}B_6$ to 1216 °C in $(Nd_{0.725}Dy_{0.275})_{15}Fe_{79}B_6$.

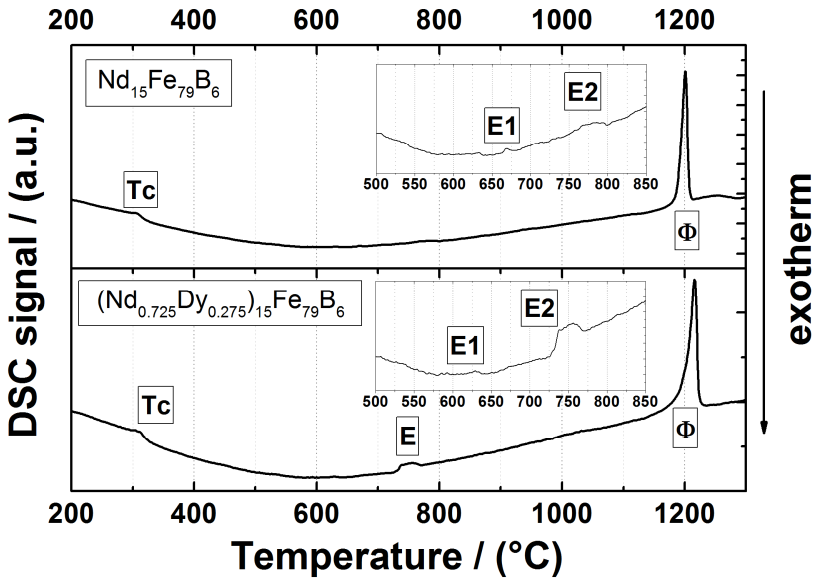

Figure 5-14 DSC heating curves of (Nd,Dy)-Fe-B and Nd-Fe-B, for comparison. The marked peaks correspond to Curie-Temperature (Tc), melting of a Nd - or Dy - rich eutectic phase (E) and melting of the ϕ - phase (ϕ). *The DSC analysis was conducted by C. Fasel, TU Darmstadt.*

Table 5-7: Position of DSC peaks for $Nd_{15}Fe_{79}B_6$ and $(Nd_{0.725}Dy_{0.275})_{15}Fe_{79}B_6$ in °C, heating regime. All peaks are endothermic. The peaks correspond to Curie-Temperature (Tc), melting of a Nd- or Dy - rich eutectic phase (E) and melting of the ϕ - phase (ϕ).

[°C]	T_c	E	ϕ
$Nd_{15}Fe_{79}B_6$	308	667/≈770	1201
$(Nd_{0.725}Dy_{0.275})_{15}Fe_{79}B_6$	311	627/730-770	1216

Chosen compositions as anisotropy powders

For the AP a high phase content of Dy-Fe-B or (Nd,Dy)-Fe-B ϕ - phase, and possibly the presence of a low melting eutectic phase was aimed at. Therefore, the following compounds have been chosen as AP for the powder blending process with $Nd_{15}Fe_{79}B_6$ as BP:

- homogenized $Dy_{15}Fe_{79}B_6$
- melt - spun $Dy_{15}Fe_{79}B_6$
- suction - cast $Dy_{15}Fe_{79}B_6$
- homogenized $Dy_{15}Fe_{79}B_6Cu_5$
- homogenized $(Nd_{0.725}Dy_{0.275})_{15}Fe_{79}B_6$

5.2.2. Production of sintered (Nd,Dy)-Fe-B magnets through powder blending

As overall composition $(Nd_{0.9}Dy_{0.1})_{15}Fe_{79}B_6$ was chosen, i.e. the established „15-79-6“ composition with every 10th Nd atom replaced by Dy. With this ratio, the Dy content is high enough to be able to clearly observe its effects, but low enough to keep the amount of necessary AP small. The different AP were mixed with the $Nd_{15}Fe_{79}B_6$ BP. Typical mass ratios are:

- 25.0 g of $Nd_{15}Fe_{79}B_6$ BP blended with 2.9 g of Dy-Fe-B or Dy-Fe-B-X AP
- 17.5 g of $Nd_{15}Fe_{79}B_6$ BP blended with 10.0 g of (Nd,Dy)-Fe-B AP

To produce the AP with a smaller particle size than the BP, the AP was milled first for 60 min in a ball milling vial. After that the BP was added and the whole mix was milled together for another 30 min. The resulting particle size distributions are shown in Figure 5-15. The AP are milled slightly finer than the BP, with less than one µm difference in the d_{50} value. The d_{50} for the Dy-Fe-B AP is likely measured a bit too high due to agglomeration of extremely fine particles (cf. Figure 3-5). Ideally, the AP should be much finer than the BP, and produced separately in a controlled and precise manner. However, for this purpose more sophisticated equipment, e.g. a jet mill and a tumble mixer under protective atmosphere, is needed. However, the scope of the thesis lies on the qualitative investigation of the used AP as suitable for producing blended magnets. The optimization of the blending process will be the subject of future work.

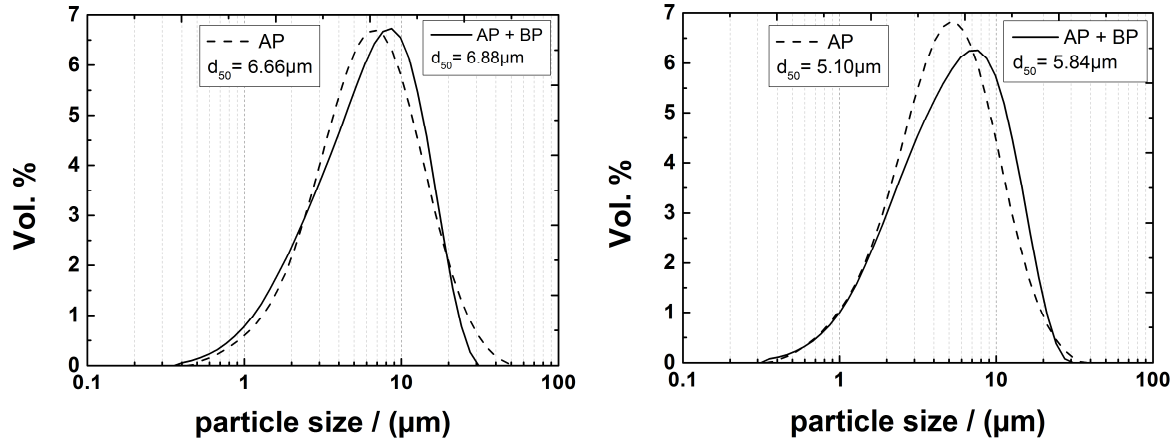

Figure 5-15: Particle size distribution of the AP as well as the mix of AP and BP. AP = Dy-Fe-B-X (left) / (Nd,Dy)-Fe-B (right). *The particle size analysis was conducted by J. Gassmann at the Fraunhofer IWKS, Hanau.*

From the obtained powders magnets were produced as described before. A depiction of the density of the produced magnets vs. the required sintering temperature reveals a huge discrepancy between the magnets made with (Nd,Dy)-Fe-B as AP, compared to Dy-Fe-B and Dy-Fe-B-Cu (Figure 5-16). While the former require a sintering temperature of 1050 °C, the latter are not fully dense even after sintering at 1100 °C. The reason is most likely the presence of secondary phases with high melting temperatures during sintering. The high sintering temperatures will negatively affect the coercivity of the magnets, as will be shown in the next chapter.

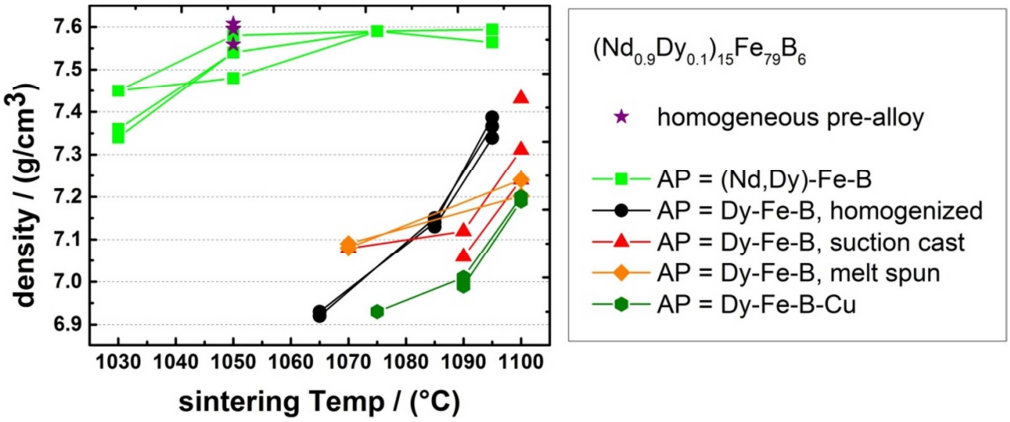

Figure 5-16: Density - sintering temperature chart for $(Nd_{0.9}Dy_{0.1})_{15}Fe_{79}B_6$ magnets produced by powder blending with different anisotropy powders. For comparison the magnets made from the homogeneous pre - alloy are also shown. For each data point the sintering time is 90 min.

The impurity levels in the magnets produced with Dy-Fe-B and (Nd,Dy)-Fe-B as AP are shown in Table 5-8 and are compared to a commercial magnet. The concentrations of all impurity elements are as low as in a commercial magnet (provided by Vacuumschmelze GmbH & Co. KG). Therefore, impurities can be excluded as reason for the increased sintering temperatures.

Table 5-8: Impurity concentrations in the two magnets produced by powder blending with Dy-Fe-B or (Nd,Dy)-Fe-B as AP compared with a commercial magnet (Material 2, "VD837").

[m.%] ± %	**O**	±	**N**	±	**H**	±	**C**	±
Commercial	0.25	2	0.009	15	<0.001	N.A.	0.06	15
AP = DyFeB	0.26	3	0,014	2	0.003	8	0.07	2
AP = (Nd,Dy)-Fe-B	0.26	6	<0,001	N.A.	0.003	13	0.08	<1

In the following, only the two magnets made by blending with homogenized Dy-Fe-B, as well as (Nd,Dy)-Fe-B are further analyzed. This way, the influence of a relatively low and a very high sintering temperature can be compared.

5.2.3. Properties of the produced magnets

Blended magnet produced with Dy-Fe-B as anisotropy powder

The magnet was produced in the above described way and sintered at 1095 °C. The magnetic properties are worse compared to a magnet of the same composition, but produced from a single powder ("homogeneous" magnet, Figure 5-17). While the remanence of both magnets is similar, the coercivity is only 1.28 T, compared to 1.79 T.

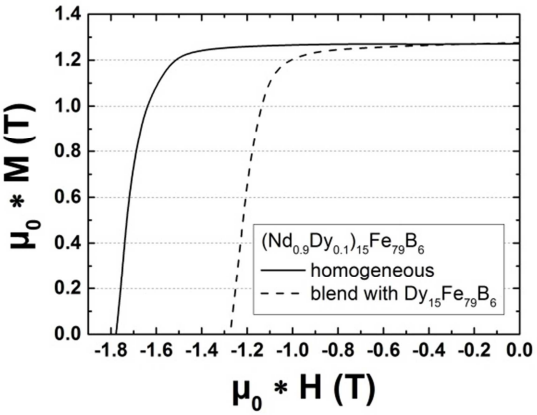

Figure 5-17: Demagnetization curves for a $(Nd_{0.9}Dy_{0.1})_{15}Fe_{79}B_6$ magnet produced with homogenized $Dy_{15}Fe_{79}B_6$ as AP, compared to a magnet with the same composition produced from a homogeneous pre - alloy.

The reason for the low H_c is the required high sintering temperature and the resulting grain growth. BSE SEM images of the microstructure show large grains >20 µm and a faint contrast between core and shell within the grains (Figure 5-18).

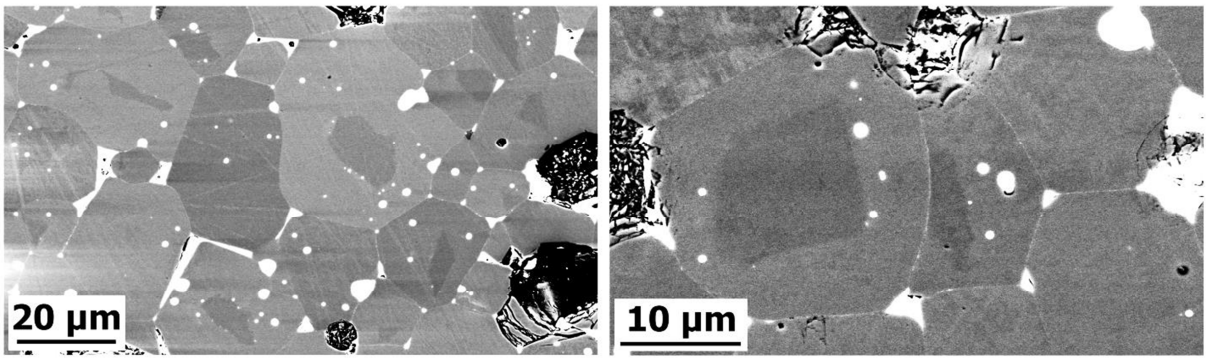

Figure 5-18: BSE SEM images of the microstructure of a $(Nd_{0.9}Dy_{0.1})_{15}Fe_{79}B_6$ magnet produced by blending $Nd_{15}Fe_{79}B_6$ and $Dy_{15}Fe_{79}B_6$ powders and sintering at 1095 °C.

An EDX map of the sample shows the distribution of Dy, Nd and Fe (Figure 5-19). Within most grains a very clear compositional contrast between Dy - free core and Dy - rich shell is visible. For Nd this contrast is reversed but less pronounced because also in the Dy - rich shells a significant amount of Nd is present. In some grains, a Dy - rich core is observed. These grains are AP particles which did not melt during sintering, most probably because they were too large. The Dy in these core is less effective for the coercivity, because it is not magnetically hardening the surface of the grains. As mentioned before, the magnets could likely be improved by more sophisticated milling equipment and smaller AP particle sizes. Fe and Dy show no spatial correlation within the resolution of the EDX, i.e. no $DyFe_x$ could be identified. However, nm - sized phases might still exist, especially at the grain boundaries.

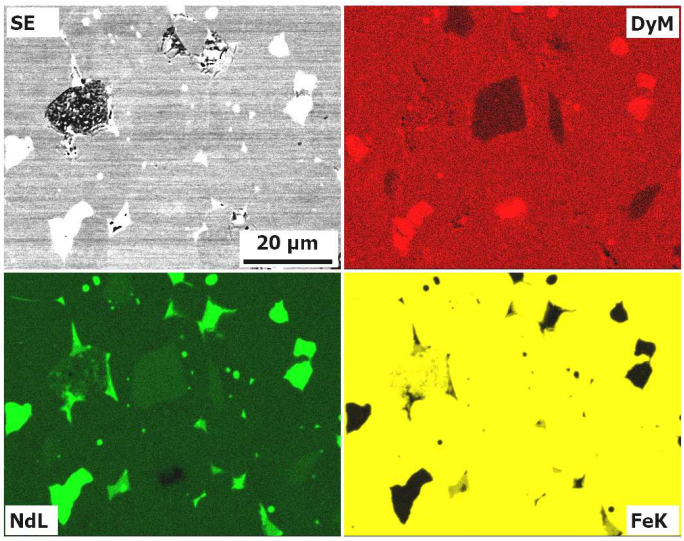

Figure 5-19: EDX map of a $(Nd_{0.9}Dy_{0.1})_{15}Fe_{79}B_6$ magnet produced by blending $Nd_{15}Fe_{79}B_6$ and $Dy_{15}Fe_{79}B_6$ powders and sintering at 1100 °C.

The composition of the phases has been investigated by standardless quantification of EDX point spectra (Table 5-9). As previously stated, the concentration values must be regarded relative to each other and not as absolute. As expected, the cores of the BP and AP show the respective Dy concentration of the pre - alloy powders. The bright cores of the unmolten AP particles contain only Dy and Fe. The shells around the grains contain an intermediate amount of Dy of 1.6 at.%. If all the AP particles had molten during sintering, this concentration would likely have been higher. The concentration of Dy in the ϕ - phase is slightly lower than in the homogeneous magnet (Table 5-4), although the difference is not significant.

Table 5-9: Quantitative EDX results of a $(Nd_{0.9}Dy_{0.1})_{15}Fe_{79}B_6$ magnet produced by blending $Nd_{15}Fe_{79}B_6$ and $Dy_{15}Fe_{79}B_6$ powders and sintering at 1100 °C.

at.%	Dy M	Nd L	Fe K
dark core	0,0	14,2	85,8
shell	1,6	12,7	85,7
bright core	12,5	0,0	87,5
overview	1,7	14,1	84,1

Blended magnet produced with (Nd,Dy)-Fe-B as anisotropy powder

By producing blended magnets with (Nd,Dy)-Fe-B as AP, a drastic reduction in sintering temperature from about 1100 °C to 1030 °C can be achieved. Most likely this is caused by the absence of high melting Dy - Fe_x secondary phases in the pre - alloy. Demagnetization curves of the produced magnets for several sintering temperatures are shown in Figure 5-20. While the magnetization remains nearly constant, the coercivity increases with decreasing sintering temperature from 1.35 T at 1075 °C to 1.63 T at 1030 °C. It is significantly increased compared to the magnets produced with Dy-Fe-B as AP (cf. Figure 5-17), but lower than the coercivity of the homogeneous magnet. The magnets are fully dense until 1050 °C and show 97 % density at 1030 °C (Figure 5-16). For this reason the sample at 1050 °C is chosen for microstructural analysis.

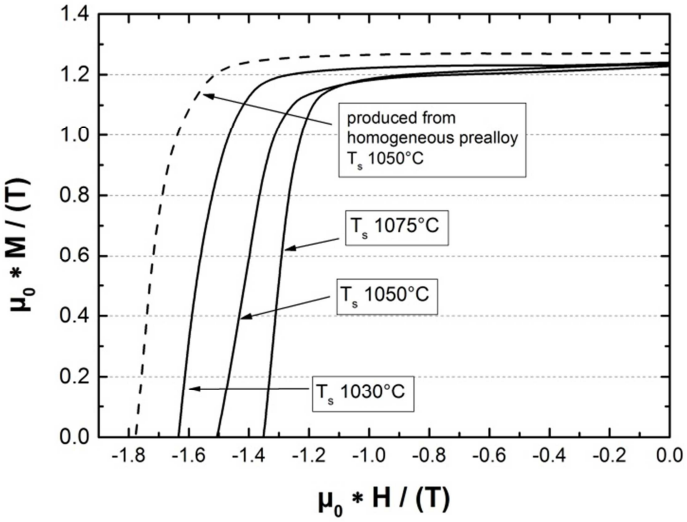

Figure 5-20: Demagnetization curves of $(Nd_{0.9}Dy_{0.1})_{15}Fe_{79}B_6$ produced by blending $Nd_{15}Fe_{79}B_6$ as BP and $(Nd_{0.725}Dy_{0.275})_{15}Fe_{79}B_6$ as AP. The sintering temperature was varied from 1075 °C to 1030 °C. For comparison, the demagnetization curve of a magnet with the same composition, but produced from a single pre - alloy is shown ("homogeneous" magnet, dashed line).

The grains show a similar core - shell structure as the previous experiment with Dy-Fe-B as AP (Figure 5-21). However, due to the low sintering temperature the grain size is significantly smaller (cf. Figure 5-18).

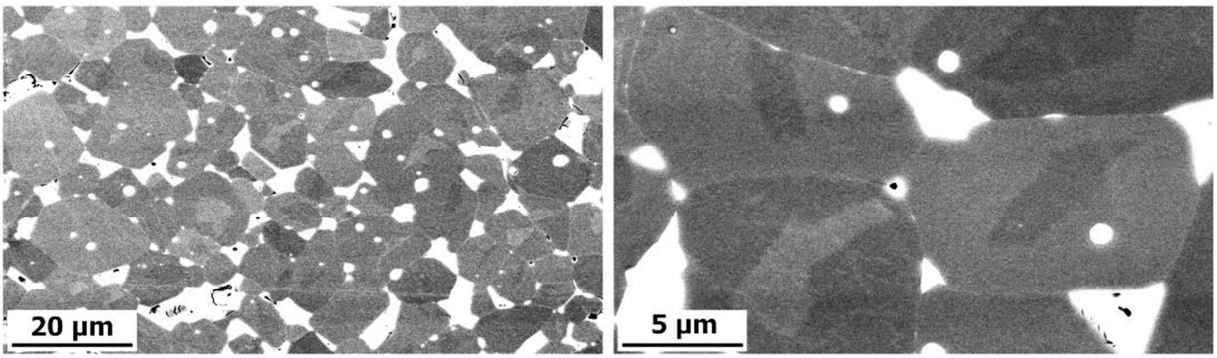

Figure 5-21: BSE SEM images of the microstructure of a $(Nd_{0.9}Dy_{0.1})_{15}Fe_{79}B_6$ magnet produced by blending $Nd_{15}Fe_{79}B_6$ and $(Nd_{0.725}Dy_{0.275})_{15}Fe_{79}B_6$ powders and sintering at 1050 °C.

An EDX map shows the distribution of Dy, Nd and Fe (Figure 5-22). Similar to the map in Figure 5-19, Dy - free grain cores and Dy - rich shells are visible. Again, in some grains a Dy - rich core is observed. As was determined with EDX point scans, the shells show an intermediate amount of Dy, a reduced amount of Nd and a high Fe amount (Table 5-10). In contrast to the magnets with Dy-Fe-B as AP, there a significantly more grains with a bright core, i.e. unmolten AP particles. The Dy in the cores is effectively

lost for the magnetic hardening and is believed to be the reason for the smaller coercivity compared to the magnets made from a homogeneous prealloy.

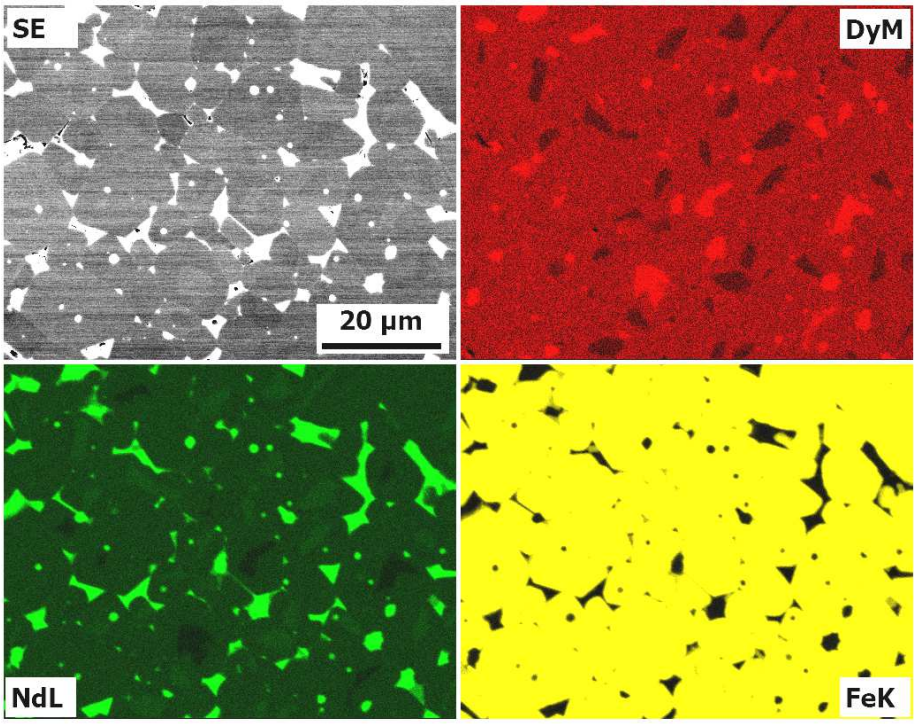

Figure 5-22: EDX map of a $(Nd_{0.9}Dy_{0.1})_{15}Fe_{79}B_6$ magnet produced by blending $Nd_{15}Fe_{79}B_6$ and $(Nd_{0.725}Dy_{0.275})_{15}Fe_{79}B_6$ powders and sintering at 1050 °C.

Table 5-10: Quantitative EDX results of a $(Nd_{0.9}Dy_{0.1})_{15}Fe_{79}B_6$ magnet produced by blending $Nd_{15}Fe_{79}B_6$ and $(Nd_{0.725}Dy_{0.275})_{15}Fe_{79}B_6$ powders and sintering at 1050 °C.

at.%	Dy M	Nd L	Fe K
dark core	0,0	14,1	85,9
shell	1,7	12,3	86,0
bright core	4,6	9,7	85,7
overview	1,8	14,2	84,0

5.3. Temperature stability of the Dy - rich shells

The temperature stability of the core - shell microstructure has been investigated. The intent was to find out, whether a low temperature annealing, e.g. a diffusion heat treatment for several hours, is influencing the microstructure. For this reason, a $(Nd_{0.9}Dy_{0.1})_{15}Fe_{79}B_6$ magnet produced by blending with

(Nd,Dy)-Fe-B as AP was annealed at 1000 °C for up to 120 h. After each heat treatment, a post - sinter annealing (PSA) was added. The demagnetization curves in Figure 5-23 show that the coercivity of the samples only slightly decreased after annealing.

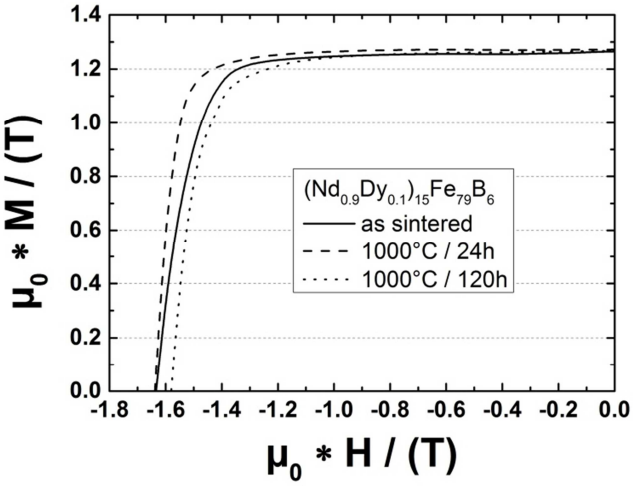

Figure 5-23: Demagnetization curves of $(Nd_{0.9}Dy_{0.1})_{15}Fe_{79}B_6$ magnets produced by blending with (Nd,Dy)-Fe-B as AP. The curves show the as - sintered state, and after a heat treatment at 1000 °C for 24 h as well as 120 h. After each annealing a PSA was conducted.

The core - shell microstructure did not homogenize even after 120 h of annealing (Figure 5-24). The only observable change are the less defined core - shell interfaces. Their thickness increased to about 1 µm after 120 h, which is the distance the Dy atoms diffused within the grains. With this distance and the approximation for the bulk diffusion length $x_{bulk} = \sqrt{D_{Dy,bulk}t}$, a diffusion coefficient $D_{Dy,1000°C}$ of $2 * 10^{-14}\ cm^2/s$ can be estimated. The findings confirm the very small bulk diffusion coefficients for Dy in $Nd_2Fe_{14}B$ at 900 °C (cf. chapter 4.1.4). Regarding the results it can be stated, that a low temperature annealing below 1000 °C will not alter core - shell microstructures due to Dy bulk diffusion.

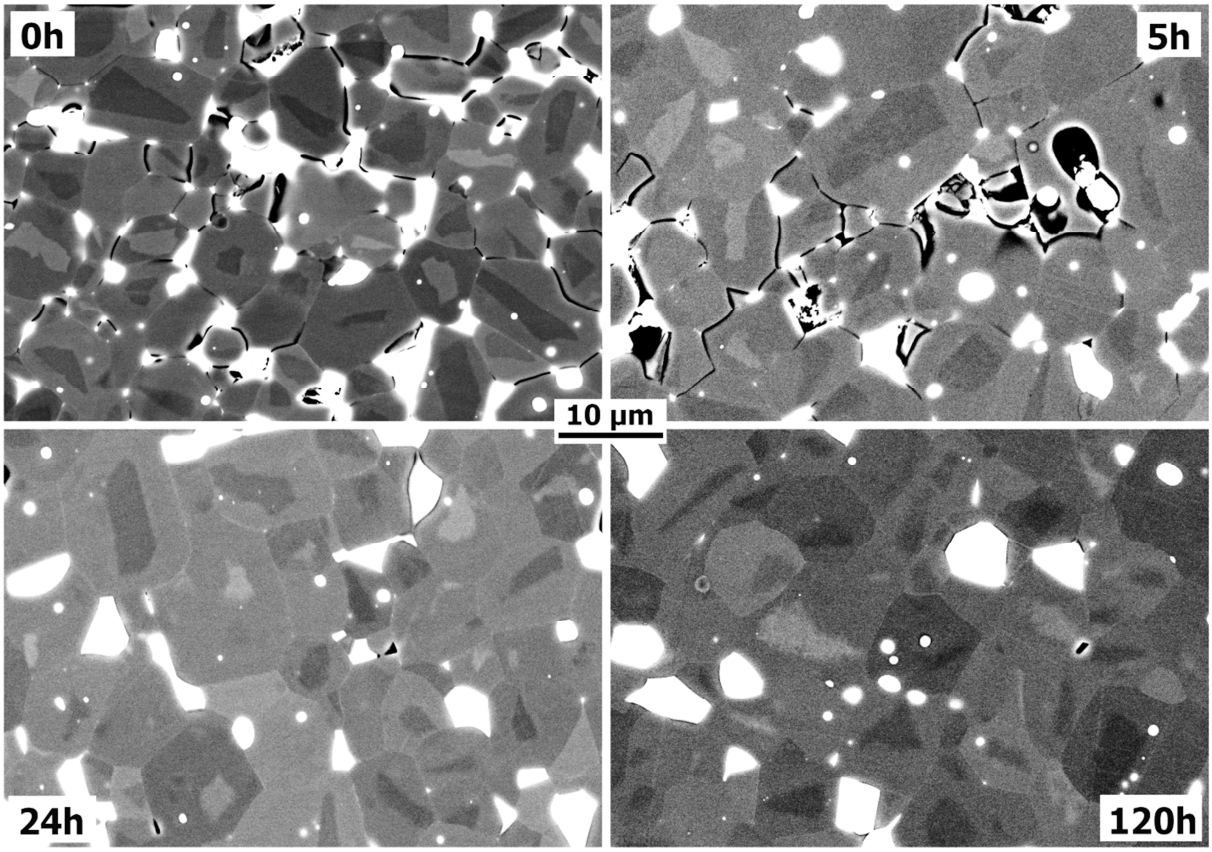

Figure 5-24: BSE SEM images of the microstructure of $(Nd_{0.9}Dy_{0.1})_{15}Fe_{79}B_6$ magnets produced by blending with (Nd,Dy)-Fe-B as AP for the as - sintered state and after heat treatments at 1000 °C for up to 120 h.

6. Conclusions and outlook

The first part of the thesis investigates the grain boundary diffusion process (GBDP) of heavy rare earth (HRE) elements in commercial sintered Nd-Fe-B based permanent magnets. The aim of the process is to increase the overall coercivity and temperature stability of a sintered Nd-Fe-B magnet with a much reduced amount of required additional HRE, compared to conventional processing. The dependence of both microstructure and magnetic properties on the annealing temperature of the Dy diffusion in Dy - lean Nd-Fe-B permanent magnets has been analyzed and an optimum annealing temperature of 900 °C was determined. In depth Microstructural and magnetic characterization proved that the diffusion occurs over the grain boundaries up to a distance of several mm. However, the benefits of the diffusion process are rapidly decreasing for distances greater than 1.5 mm. Coating sintered magnets on all sides can partially compensate for this size restriction, but for many practical applications the maximum thickness of the diffusion processed samples is limited to about 5 mm. The evaluation of diffusion speeds of Dy and Tb in both Dy - rich and Dy - lean commercial Nd-Fe-B magnet with different grain sizes showed that Tb diffuses significantly faster than Dy. From an application point of view this means that with Tb larger magnet geometries can be effectively diffusion processed, compared to Dy.

A disadvantage of the GBDP is the required additional annealing step, which increases the price of the magnet. The majority of the added costs are the related to the processing, not the HRE materials. Therefore, Tb is nowadays the preferred diffusant, since it also provides a nearly twice as large coercivity increase than Dy. For comparative studies Gd and Ce have also been diffused in Dy-rich commercial Nd-Fe-B magnets, and a decrease of the overall coercivity of the magnets was found. Regarding the results, the GBDP was determined to be an very effective tool to increase the coercivity of a sintered Nd-Fe-B magnet. However, the savings due to a reduced amount of HRE after the GBDP need to be weighed against the higher production costs of the magnets. In light of the much decreased HRE prices in recent years (cf. Figure 1-1) it needs to be assessed for given applications, whether the GBDP is economically feasible.

To better understand the relation between lateral coercivity gradients produced by the GBDP and the demagnetization behavior of macroscopic magnets, FEM simulations have been carried out (Loewe et al. submitted to Acta Materialia). First predictions of demagnetization curves show very good matches with experimental data. Further refinement of the model will enable predictions of necessary coercivity

gradients within magnetic assemblies, in order to achieve the desired magnetic demagnetization behavior.

The second part of the thesis explores an alternative to the GBDP, a technique of manufacturing (Nd,Dy)-Fe-B sintered magnets by blending a Dy - free *base powder* (BP) with a Dy - rich *anisotropy powder* (AP) prior to sintering (*patent pending*). The technique provides a core-shell microstructure similar to GBD processed magnets. In difference to previous works, the current approach uses Dy-Fe-B or (Nd,Dy)-Fe-B based ϕ - phases as AP. The aim is to decrease the sintering temperature of the magnets and to avoid the formation of deleterious secondary phases. Furthermore, the AP is produced slightly smaller than the BP in order to facilitate the melting during liquid phase sintering. The coercivity increase per amount of HRE is lower than for the GBDP, because the HRE enriched areas in the vicinity of the GB are much larger. However, in contrast to the GBDP the novel technique is not limited to only a few mm, but is able to produce magnets of any size and shape.
In the produced magnets a pronounced core - shell microstructure within the whole volume was observed with electron microscopy. The coercivity of the so-produced magnets is still below the value of a magnet produced with a single powder. The main reason for this is related to an insufficiently small particle size of the HRE rich AP. Future experiments with more sophisticated milling equipment, i.e. a target mill, are planned in cooperation with a partner project group at the Fraunhofer IWKS / Hanau. Also, another interesting "2 - powder" system will be explored: (Nd,Ce)-Fe-B as BP and Nd-Fe-B as AP. It aims to substitute Nd with the relatively cheap and abundant Ce.

Literature

[Akdogan2014] O. AKDOGAN, A. DOBRYNIN, D. LE ROY, N.M. DEMPSEY, D. GIVORD. *Superferrimagnetism in hard Nd-Fe-B thick films, an original concept for coercivity enhancement*, J. Appl. Phys. 115 (2014).

[Bance2014] S. BANCE, H. OEZELT, T. SCHREFL, G. CIUTA, N.M. DEMPSEY, D. GIVORD, M. WINKLHOFER, G. HRKAC, G. ZIMANYI, O. GUTFLEISCH, T.G. WOODCOCK, T. SHOJI, M. YANO, A. KATO, A. MANABE. *Influence of defect thickness on the angular dependence of coercivity in rare-earth permanent magnets*, Appl. Phys. Lett. 104 (2014).

[Bance2014] S.O. BANCE, H.; SCHREFL, T.; WINKLHOFER, M.; HRKAC, G.; ZIMANYI, G.; GUTFLEISCH, O.; EVANS, R. F. L.; CHANTRELL, R. W.; SHOJI, T.; YANO, M.; SAKUMA, N.; KATO, A.; MANABE, A. *High energy product in Battenberg structured magnets*, Appl. Phys. Lett. 105 (2014).

[Bauer2010] D. BAUER, D. DIAMOND, J. LI, D. SANDALOW, P. TELLEEN, B. WANNERET. *Critical Materials Strategy, US Department of Energy*. 2010.

[Bernardi1998] J. BERNARDI, J. FIDLER, M. SAGAWA, Y. HIROSE. *Microstructural analysis of strip cast Nd–Fe–B alloys for high $(BH)_{max}$ magnets*, J. Appl. Phys. 83 (1998) 6396.

[Brown1945] W.F. BROWN. *Virtues and Weaknesses of the Domain Concept*, Rev. Mod. Phys. 17 (1945) 15-19.

[Capehart1993] T.W. CAPEHART, R.K. MISHRA, G.P. MEISNER, C.D. FUERST, J.F. HERBST. *Steric Variation of the Cerium Valence in $Ce_2Fe_{14}B$ and Related-Compounds*, Appl. Phys. Lett. 63 (1993) 3642-3644.

[Chamayou2007] A. CHAMAYOU, J.A. DODDS. *Chapter 8 - Air Jet Milling*. In: Agba D. Salman MG, Handbook of Powder Technology, Volume 12. Elsevier Science B.V., 2007. 421-435.

[Coey2010] J.M.D. COEY. *Magnetism and Magnetic Materials*: Cambridge University Press, 2010.

[Cook2001] B.A. COOK, J.L. HARRINGA, F.C. LAABS, K.W. DENNIS, A.M. RUSSELL, R.W. MCCALLUM. *Diffusion of Fe, Co, Nd, and Dy in R-2(Fe1-xCox)(14)B where R = Nd or Dy*, J. Magn. Magn. Mater. 233 (2001) L136-L141.

[Croat1984] J.J. CROAT, J.F. HERBST, R.W. LEE, F.E. PINKERTON. *Pr-Fe and Nd-Fe-Based Materials - a New Class of High-Performance Permanent-Magnets*, J. Appl. Phys. 55 (1984) 2078-2082.

[de Groot1998] C.H. DE GROOT, K.H.J. BUSCHOW, F.R. DE BOER, K. DE KORT. *Two-powder $Nd_2Fe_{14}B$ magnets with DyGa-addition*, J. Appl. Phys. 83 (1998) 388-393.

[Doser1988] M. DOSER, G. KEELER. *Long-term stability of Fe-B-Nd-Dy alloys made by Dy_2O_3 additions*, J. Appl. Phys. 64 (1988) 5311-5313.

[Eckert1991] D. ECKERT, P. NOTHNAGEL, K.H. MÜLLER, A. HANDSTEIN. *The Influence of Texture on the Magnetization Behavior of Sintered Nd-Fe-B Magnets*, J. Magn. Magn. Mater. 101 (1991) 385-386.

[EU Commission2010] EU COMMISSION. *Critical raw materials for the EU. Report of the Ad-hoc Working Group on defining critical raw materials*, Ad-hoc Working Group: July 2010 (2010) 84.

[Fahnle1993] M. FAHNLE, K. HUMMLER, M. LIEBS, T. BEUERLE. *Ab-Initio Electron Theory for Hard-Magnetic Rare-Earth-Transition-Metal Intermetallics*, Appl. Phys. A 57 (1993) 67-76.

[Fernengel1996] W. FERNENGEL, A. LEHNERT, M. KATTER, W. RODEWALD, B. WALL. *Examination of the degree of alignment in sintered Nd-Fe-B magnets by measurements of the remanent polarizations*, J. Magn. Magn. Mater. 157 (1996) 19-20.

[Fiorillo2004] F. FIORILLO. *Characterization and Measurement of Magnetic Materials*: Elsevier 2004.

[Fisher1951] J.C. FISHER. *Calculation of Diffusion Penetration Curves for Surface and Grain Boundary Diffusion*, J. Appl. Phys. 22 (1951) 74-77.

[Fritz1992] K. FRITZ, B. GRIEB, E.T. HENIG, G. PETZOW. *The Influence of Dy on the Phase-Relations of (Nd,Dy)-Fe-B Alloys*, Z. Metallk. 83 (1992) 157-161.

[Gabay2011] A.M. GABAY, M. MARINESCU, W.F. LI, J.F. LIU, G.C. HADJIPANAYIS. *Dysprosium-saving improvement of coercivity in Nd-Fe-B sintered magnets by Dy_2S_3 additions*, J. Appl. Phys. 109 (2011).

[Gauß2016] R. GAUß, O. GUTFLEISCH. *Magnetische Materialien—Schlüsselkomponenten für neue Energietechnologien*. Rohstoffwirtschaft und gesellschaftliche Entwicklung. Springer, 2016. 99-118.

[Ghandehari1986] M.H. GHANDEHARI. *Reactivity of Dy_2O_3 and Tb_4O_7 with $Nd_{15}Fe_{77}B_8$ Powder and the Coercivity of the Sintered Magnets*, Appl. Phys. Lett. 48 (1986) 548-550.

[Givord1988] D. GIVORD, P. TENAUD, T. VIADIEU. *Coercivity mechanisms in ferrites and rare earth transition metal sintered magnets ($SmCo_5$, Nd-Fe-B)*, IEEE Trans. Magn. 24 (1988) 1921-1923.

[Goto2010] R.S. GOTO, S.; MATSUURA, M.; TEZUKA, N.; UNE, Y. SAGAWA, M. *Microstructure During the Fabrication Process of Nd-Fe-B Sintered Magnets using Atomized Powders*. 21st Workshop on Rare-Earth Permanent Magnets and their Applications. Bled, Slovenia, 2010.

[Graham2009] C. GRAHAM, B. CULLITY. *Introduction to magnetic materials*: John Wiley & Sons, 2009.

[Grieb1989] B. GRIEB, G. SCHNEIDER, E.T. HENIG, G. PETZOW. *Structural Investigations and Constitution Along $Fe_{14}(Nd_{1-x}(Tb\ or\ Dy)_x)_2B$*, Z. Metallk. 80 (1989) 515-519.

[Gutfleisch2000] O. GUTFLEISCH. *Controlling the properties of high energy density permanent magnetic materials by different processing routes*, J. Phys. D: Appl. Phys. 33 (2000) R157-R172.

[Gutfleisch2011] O. GUTFLEISCH, M.A. WILLARD, E. BRUCK, C.H. CHEN, S.G. SANKAR, J.P. LIU. *Magnetic Materials and Devices for the 21st Century: Stronger, Lighter, and More Energy Efficient*, Adv. Mater. 23 (2011) 821-842.

[Hadjipanayis1983] G.C. HADJIPANAYIS, R.C. HAZELTON, K.R. LAWLESS. *New Iron-Rare-Earth Based Permanent-Magnet Materials*, Appl. Phys. Lett. 43 (1983) 797-799.

[Harimoto2007] D.M. HARIMOTO, Y. *Development of High Performance Nd-Fe-B Sintered Magnets*, Hitachi Met. Tech. Rev. 23 (2007) 69.

[Harris1987] I.R. HARRIS, P.J. MCGUINESS, D.G.R. JONES, J.S. ABELL. *Nd-Fe-B Permanent-Magnets - Hydrogen Absorption Desorption Studies (Hads) on $Nd_{16}Fe_{76}B_8$ and $Nd_2Fe_{14}B$*, Phys. Scr. T19b (1987) 435-440.

[Harris1985] I.R. HARRIS, C. NOBLE, T. BAILEY. *The Hydrogen Decrepitation of an $Nd_{15}Fe_{77}B_8$ Magnetic Alloy*, J. Less.-Common Met. 106 (1985) L1-L4.

[Harrison1961] L.G. HARRISON. *Influence of Dislocations on Diffusion Kinetics in Solids with Particular Reference to Alkali Halides*, Trans. Faraday Soc. 57 (1961) 1191-1199.

[Hatch2011] G.P. HATCH. *Critical rare earths: Global supply and demand projections and the leading contenders for new sources of supply*, Technology Metals Research, LLC (2011).

[Hattori2009] T. HATTORI, H. ISHIHARA, S. SUGIMOTO, R. GOTO, N. TEZUKA, Y. UNE, M. SAGAWA. *Microstructural Evaluation of Nd-Fe-B Jet-Milled Powders*, Mater. Trans. 50 (2009) 2347-2350.

[Herbst1991] J.F. HERBST. *$R_2Fe_{14}B$ Materials - Intrinsic Properties and Technological Aspects*, Rev. Mod. Phys. 63 (1991) 819-898.

[Herbst2012] J.F. HERBST, M.S. MEYER, F.E. PINKERTON. *Magnetic hardening of Ce2Fe14B*, J. Appl. Phys. 111 (2012).

[Hilzinger2013] R. HILZINGER, W. RODEWALD. *Magnetic Materials*: Wiley, 2013.

[Hirosawa1986] S. HIROSAWA, Y. MATSUURA, H. YAMAMOTO, S. FUJIMURA, M. SAGAWA, H. YAMAUCHI. *Magnetization and Magnetic-Anisotropy of $R_2Fe_{14}B$ Measured on Single-Crystals*, J. Appl. Phys. 59 (1986) 873-879.

[Horbach2007] J. HORBACH, S.K. DAS, A. GRIESCHE, M.P. MACHT, G. FROHBERG, A. MEYER. *Self-diffusion and interdiffusion in $Al_{80}Ni_{20}$ melts: Simulation and experiment*, Phys. Rev. B 75 (2007).

[Hrkac2014] G. HRKAC, T.G. WOODCOCK, K.T. BUTLER, L. SAHARAN, M.T. BRYAN, T. SCHREFL, O. GUTFLEISCH. *Impact of different Nd-rich crystal-phases on the coercivity of Nd-Fe-B grain ensembles*, Scripta Mater. 70 (2014) 35-38.

[Hrkac2010] G. HRKAC, T.G. WOODCOCK, C.L. FREEMAN, A. GONCHAROV, J. DEAN, T. SCHREFL, O. GUTFLEISCH. *The role of local anisotropy profiles at grain boundaries on the coercivity of $Nd_2Fe_{14}B$ magnets*, Appl. Phys. Lett. 97 (2010).

[Huang2015] S.L. HUANG, H.B. FENG, M.G. ZHU, A.H. LI, Y.F. LI, Y.C. SUN, Y. ZHANG, W. LI. *Optimal design of sintered Ce9Nd21FebalB1 magnets with a low-melting-point (Ce,Nd)-rich phase*, Int J Min Met Mater 22 (2015) 417-422.

[Hubert2014] A. HUBERT, R. SCHÄFER. *Magnetic Domains: The Analysis of Magnetic Microstructures*: Springer, 2014.

[ICSD2014] ICSD. *Inorganic Crystal Structure Database*. https://icsd.fiz-karlsruhe.de, 2014.

[Kaneko2004] Y. KANEKO. *Technological Evolution and Application Trends of NdFeB Sintered Magnets in Japan*. Proceedings of the 18th Workshop on High Performance Magnets & Their Applications. Annecy (France), 2004.

[Khlopkov2004] K. KHLOPKOV, O. GUTFLEISCH, D. ECKERT, D. HINZ, B. WALL, W. RODEWALD, K.-H. MÜLLER, L. SCHULTZ. *Local texture in Nd–Fe–B sintered magnets with maximised energy density*, J. Alloys Compd. 365 (2004) 259-265.

[Khlopkov2007] K. KHLOPKOV, O. GUTFLEISCH, D. HINZ, K.-H. MÜLLER, L. SCHULTZ. *Evolution of interaction domains in textured fine-grained Nd2Fe14B magnets*, J. Appl. Phys. 102 (2007) 023912.

[Kim2016] T.-H. KIM, S.-R. LEE, S.J. YUN, S.H. LIM, H.-J. KIM, M.-W. LEE, T.-S. JANG. *Anisotropic diffusion mechanism in grain boundary diffusion processed Nd-Fe-B sintered magnet*, Acta Mater. 112 (2016) 59-66.

[Kim2012] T.H. KIM, S.R. LEE, S. NAMKUMG, T.S. JANG. *A study on the Nd-rich phase evolution in the Nd-Fe-B sintered magnet and its mechanism during post-sintering annealing*, J. Alloys Compd. 537 (2012) 261-268.

[Kirchmayr1991] H. KIRCHMAYR. *Determination of the Anisotropy Field by the Singular Point Detection Method*. In: Long GJ, Supermagnets, Hard Magnetic Materials. Springer Netherlands, 1991. 449-460.

[Kneller1962] E. KNELLER, A. SEEGER, H. KRONMÜLLER. *Ferromagnetismus*: Springer, 1962.

[Komuro2010] M. KOMURO, Y. SATSU, H. SUZUKI. *Increase of Coercivity and Composition Distribution in Fluoride-Diffused NdFeB Sintered Magnets Treated by Fluoride Solutions*, IEEE Trans. Magn. 46 (2010) 3831-3833.

[Kronmüller1987] H. KRONMÜLLER. *Theory of Nucleation Fields in Inhomogeneous Ferromagnets*, Phys. Stat. Sol. B 144 (1987) 385-396.

[Kronmüller1988] H. KRONMÜLLER, K.D. DURST, M. SAGAWA. *Analysis of the magnetic hardening mechanism in RE-FeB permanent magnets*, J. Magn. Magn. Mater. 74 (1988) 291-302.

[Li2009] W.F. LI, T. OHKUBO, K. HONO, M. SAGAWA. *The origin of coercivity decrease in fine grained Nd-Fe-B sintered magnets*, J. Magn. Magn. Mater. 321 (2009) 1100-1105.

[Loewe2015] K. LOEWE, C. BROMBACHER, M. KATTER, O. GUTFLEISCH. *Temperature-dependent Dy diffusion processes in Nd-Fe-B permanent magnets*, Acta Mater. 83 (2015) 248-255.

[Malfliet2008] A. MALFLIET, G. CACCIAMANI, N. LEBRUN, P. ROGL. *Boron - Iron - Neodymium*. Landolt-Börnstein - Ternary Alloy Systems, 11, Subvolume D. Springer, 2008.

[McGuiness1989] P.J. MCGUINESS, E. DEVLIN, I.R. HARRIS, E. ROZENDAAL, J. ORMEROD. *A Study of Nd-Fe-B Magnets Produced Using a Combination of Hydrogen Decrepitation and Jet Milling*, J. Mater. Sci. 24 (1989) 2541-2548.

[Mehrer2007] H. MEHRER. *Diffusion in Solids: Fundamentals, Methods, Materials, Diffusion-Controlled Processes*: Springer, 2007.

[Molycorp Inc.2015] Press release, Molycorp Inc., 2015. http://www.molycorp.com/molycorp-inc-files-restructuring-plan/

[Nakamura2011] H. NAKAMURA, K. HIROTA, T. OHASHI, T. MINOWA. *Coercivity distributions in Nd-Fe-B sintered magnets produced by the grain boundary diffusion process*, J. Phys. D: Appl. Phys. 44 (2011).

[Nishio1996] H. NISHIO, H. TAGUCHI, S. HASHIMOTO, K. YAJIMA, A. FUKUNO, H. YAMAMOTO. *A comparison of magnetic anisotropy constants and anisotropy fields of permanent magnets determined by various measuring methods*, J. Phys. D: Appl. Phys. 29 (1996) 2240-2245.

[Nothnagel1991] P. NOTHNAGEL, K.H. MÜLLER, D. ECKERT, A. HANDSTEIN. *The Influence of Particle-Size on the Coercivity of Sintered NdFeB Magnets*, J. Magn. Magn. Mater. 101 (1991) 379-381.

[Oesterreicher1984] K. OESTERREICHER, H. OESTERREICHER. *Structure and Magnetic-Properties of* $Nd_2Fe_{14}BH_{2.7}$, Phys. Stat. Sol. A: Appl. Res. 85 (1984) K61-K64.

[Oono2011] N. OONO, M. SAGAWA, R. KASADA, H. MATSUI, A. KIMURA. *Production of thick high-performance sintered neodymium magnets by grain boundary diffusion treatment with dysprosium-nickel-aluminum alloy*, J. Magn. Magn. Mater. 323 (2011) 297-300.

[Park2000] K.T.H. PARK, K.; SAGAWA, M. *Effect of Metal-Coating and Consecutive Heat Treatment on Coercivity of Thin Nd-Fe-B Sintered Magnets*. 16th Int. Workshop on Rare-Earth Magnets and Their Applications. Sendai, Japan 2000. 257.

[Popov2015] A.G. POPOV, O.A. GOLOVNIA, V.A. BYKOV. *Pressless process in route of obtaining sintered Nd-Fe-B magnets*, J. Magn. Magn. Mater. 383 (2015) 226-231.

[Predel1995] B. PREDEL. *Nd-Tb (Neodymium-Terbium): Datasheet from Landolt-Börnstein - Group IV Physical Chemistry · Volume 5H: "Li-Mg – Nd-Zr" in SpringerMaterials*. In: Madelung O, editor: Springer-Verlag Berlin Heidelberg, 1995.

[Predel1996] B. PREDEL. *Dy-Nd (Dysprosium-Neodymium): Datasheet from Landolt-Börnstein - Group IV Physical Chemistry · Volume 5E: "Dy-Er – Fr-Mo" in SpringerMaterials*. In: Madelung O, editor: Springer-Verlag Berlin Heidelberg, 1996.

[Raghavan2010] V. RAGHAVAN. *Al-Cu-Dy (Aluminum-Copper-Dysprosium)*, Journal of phase equilibria and diffusion 31 (2010) 282-284.

[Reller2013] A. RELLER, V. ZEPF, B. ACHZET. *The Importance of Rare Metals for Emerging Technologies*. In: Angrick M, Factor X: Re-source - Designing the Recycling Society. Springer Netherlands, 2013. 203-219.

[Rodewald2002] W. RODEWALD, M. KATTER, G.W. REPPEL. *Fortschritte bei pulvermetallurgisch hergestellten Nd-Fe-B Magneten*. Hagener Symposium Pulvermetallurgie, vol. 18, 2002. 225 -245.

[Sagawa2012] M. SAGAWA. *How the World's Strongest "Neodymium Magnet" Came to Exist*. Japan prize talk, 2012.

[Sagawa1984] M. SAGAWA, S. FUJIMURA, N. TOGAWA, H. YAMAMOTO, Y. MATSUURA. *New Material for Permanent-Magnets on a Base of Nd and Fe*, J. Appl. Phys. 55 (1984) 2083-2087.

[Sagawa2000] M. SAGAWA, H. NAGATA, T. WATANABE, O. ITATANI. *Rubber isostatic pressing (RIP) of powders for magnets and other materials*, Mater. Design 21 (2000) 243-249.

[Sagawa2008] M. SAGAWA, Y. UNE. *A new process for producing Nd–Fe–B sintered magnets with small grain size*. 20th International Workshop on Rare Earth Permanent Magnets and their Applications. Knossos, Greece, 2008. 103-105.

[Samardzija2012] Z. SAMARDZIJA, P. MCGUINESS, M. SODERZNIK, S. KOBE, M. SAGAWA. *Microstructural and compositional characterization of terbium-doped Nd-Fe-B sintered magnets*, Mater. Charact. 67 (2012) 27-33.

[Sasaki2015] T.T. SASAKI, T. OHKUBO, Y. UNE, H. KUBO, M. SAGAWA, K. HONO. *Effect of carbon on the coercivity and microstructure in fine-grained Nd-Fe-B sintered magnet*, Acta Mater. 84 (2015) 506-514.

[Sawatzki2014] S. SAWATZKI, A. DIRKS, B. FRINCU, K. LOWE, O. GUTFLEISCH. *Coercivity enhancement in hot-pressed Nd-Fe-B permanent magnets with low melting eutectics*, J. Appl. Phys. 115 (2014).

[Schatt2007] W. SCHATT, K.P. WIETERS, B. KIEBACK. *Pulvermetallurgie*: Springer, 2007.

[Schneider1990] G. SCHNEIDER, E.T. HENIG, F.P. MISSELL, G. PETZOW. *Microstructure of Sintered Fe-Nd-B Magnets*, Z. Metallk. 81 (1990) 322-329.

[Schneider1986] G. SCHNEIDER, E.T. HENIG, G. PETZOW, H.H. STADELMAIER. *Phase-Relations in the System Fe-Nd-B*, Z. Metallk. 77 (1986) 755-761.

[Seelam2014] U.M.R. SEELAM, T. OHKUBO, T. ABE, S. HIROSAWA, K. HONO. *Faceted shell structure in grain boundary diffusion-processed sintered Nd-Fe-B magnets*, J. Alloys Compd. 617 (2014) 884-892.

[Sepehri-Amin2013] H. SEPEHRI-AMIN, T. OHKUBO, K. HONO. *The mechanism of coercivity enhancement by the grain boundary diffusion process of Nd-Fe-B sintered magnets*, Acta Mater. 61 (2013) 1982-1990.

[Sepehri-Amin2013] H. SEPEHRI-AMIN, T. OHKUBO, S. NAGASHIMA, M. YANO, T. SHOJI, A. KATO, T. SCHREFL, K. HONO. *High-coercivity ultrafine-grained anisotropic Nd-Fe-B magnets processed by hot deformation and the Nd-Cu grain boundary diffusion process*, Acta Mater. 61 (2013) 6622-6634.

[Sepehri-Amin2012] H. SEPEHRI-AMIN, T. OHKUBO, T. SHIMA, K. HONO. *Grain boundary and interface chemistry of an Nd-Fe-B-based sintered magnet*, Acta Mater. 60 (2012) 819-830.

[Shinba2005] Y. SHINBA, T.J. KONNO, K. ISHIKAWA, K. HIRAGA, M. SAGAWA. *Transmission electron microscopy study on Nd-rich phase and grain boundary structure of Nd-Fe-B sintered magnets*, J. Appl. Phys. 97 (2005).

[Stoner1948] E.C. STONER, E.P. WOHLFARTH. *A Mechanism of Magnetic Hysteresis in Heterogeneous Alloys*, Philos. Trans. R. Soc. London, Ser. A 240 (1948) 599-642.

[Sugimoto2011] S. SUGIMOTO. *Current status and recent topics of rare-earth permanent magnets*, J. Phys. D: Appl. Phys. 44 (2011).

[Suryanarayana2001] C. SURYANARAYANA. *Mechanical alloying and milling*, Prog. Mater Sci. 46 (2001) 1-184.

[Trout1988] S.R. TROUT. *Use of Helmholtz Coils for Magnetic Measurements*, IEEE Trans. Magn. 24 (1988) 2108-2111.

[Uestuener2006] K. UESTUENER, M. KATTER, W. RODEWALD. *Dependence of the mean grain size and coercivity of sintered Nd-Fe-B magnets on the initial powder particle size*, IEEE Trans. Magn. 42 (2006) 2897-2899.

[Vacuumschmelze GmbH & Co KG2014] VACUUMSCHMELZE GMBH & CO KG. *Selten-Erd-Dauermagnete VACOMAX • VACODYM*. http://www.vacuumschmelze.de/de/produkte/dauermagnete-systeme/dauermagnete/nd-fe-b/vacodym.html, 2014.

[Velicescu1995] M. VELICESCU, P. SCHREY, W. RODEWALD. *Dy-Distribution in the Grains of High-Energy (Nd,Dy)-Fe-B Magnets*, IEEE Trans. Magn. 31 (1995) 3623-3625.

[Watanabe2013] N. WATANABE, M. ITAKURA, M. NISHIDA. *Microstructure of high coercivity Nd-Fe-Co-Ga-B hot-deformed magnet improved by the Dy diffusion treatment*, J. Alloys Compd. 557 (2013) 1-4.

[Weber2012] R.J. WEBER, D.J. REISMAN. *Rare Earth Elements: A Review of Production, Processing, Recycling, and Associated Environmental Issues*, US EPA Region (2012).

[Woodcock2014] T.G. WOODCOCK, F. BITTNER, T. MIX, K.H. MÜLLER, S. SAWATZKI, O. GUTFLEISCH. *On the reversible and fully repeatable increase in coercive field of sintered Nd-Fe-B magnets following post sinter annealing*, J. Magn. Magn. Mater. 360 (2014) 157-164.

[Woodcock2014] T.G. WOODCOCK, Q.M. RAMASSE, G. HRKAC, T. SHOJI, M. YANO, A. KATO, O. GUTILEISCH. *Atomic-scale features of phase boundaries in hot deformed Nd-Fe-Co-B-Ga magnets infiltrated with a Nd-Cu eutectic liquid*, Acta Mater. 77 (2014) 111-124.

[Woodcock2012] T.G. WOODCOCK, Y. ZHANG, G. HRKAC, G. CIUTA, N.M. DEMPSEY, T. SCHREFL, O. GUTFLEISCH, D. GIVORD. *Understanding the microstructure and coercivity of high performance NdFeB-based magnets*, Scripta Mater. 67 (2012) 536-541.

[www.metal-pages.com] accessed September 2016.

[www.nasdaq.com] accessed September 2016.

[Xu2011] F. XU, L.T. ZHANG, X.P. DONG, Q.Z. LIU, M. KOMURO. *Effect of DyF_3 additions on the coercivity and grain boundary structure in sintered Nd-Fe-B magnets*, Scripta Mater. 64 (2011) 1137-1140.

[Yan2010] G.L. YAN, P.J. MCGUINESS, J.P.G. FARR, I.R. HARRIS. *Optimisation of the processing of Nd-Fe-B with Dysprosium addition*, J. Alloys Compd. 491 (2010) L20-L24.

[Yan2006] M. YAN, L.Q. YU, W. LUO, W. WANG, W.Y. ZHANG, Y.H. WEN. *Change of microstructure and magnetic properties of sintered Nd-Fe-B induced by annealing*, J. Magn. Magn. Mater. 301 (2006) 1-5.

Curriculum Vitae

Personal information

Name	Konrad Löwe
Date of birth	18 March, 1984
Place of birth	Stralsund, Germany

Education

since 10/2010	PhD studies of Materials Science / TU Dresden & TU Darmstadt
10/2004 - 09/2010	University studies of materials science / TU Dresden Final grade: 1.5 Title: Diplom Ingenieur / graduate engineer Topic of diploma thesis: „Investigation of the Thermal Decomposition Reaction in the Magneto-caloric System $La(Fe,Si,Co)_{13}$“ Advisor: Prof. Dr. habil. Oliver Gutfleisch
09/2003 - 07/2004	Civilian service Caretaker in the child- and youth psychiatry, Medical Centre West, Stralsund
08/1994 - 07/2003	Goethe Gymnasium, Stralsund Final grade: 1.9

Own publications, patent applications and conference contributions

Publications

K. Loewe, D. Benke, C. Kübel, T. Lienig, K.P. Skokov, O. Gutfleisch (2016).
„Grain boundary diffusion of different rare earth elements in Nd-Fe-B sintered magnets by experiment and FEM simulation" Acta Materialia 124: 421-429.

K. Loewe, M. Durrschnabel, L. Molina-Luna, R. Madugundo, B. Frincu, H. J. Kleebe, O. Gutfleisch and G. C. Hadjipanayis (2016).
"Microstructure and magnetic properties of melt-spun Alnico-5 alloys." Journal of Magnetism and Magnetic Materials **407**: 230-234.

K. Loewe, C. Brombacher, M. Katter and O. Gutfleisch (2015).
"Temperature-dependent Dy diffusion processes in Nd-Fe-B permanent magnets." Acta Materialia **83**: 248-255.

K. Loewe, J. Liu, K. Skokov, J. D. Moore, H. Sepehri-Amin, K. Hono, M. Katter and O. Gutfleisch (2012). "The effect of the thermal decomposition reaction on the mechanical and magnetocaloric properties of La(Fe,Si,Co)(13)." Acta Materialia **60**(10): 4268-4276.

T. Helbig, **K. Loewe**, S. Sawatzki, M. Yi, B. Xu and O. Gutfleisch (2016).
"Experimental and Computational Analysis of Magnetization Reversal in (Dy, Nd)-Fe-B Core Shell sintered Sintered Magnets" Acta Materialia, submitted.

S. Sawatzki, A. Dirks, B. Frincu, **K. Loewe** and O. Gutfleisch (2014).
"Coercivity enhancement in hot-pressed Nd-Fe-B permanent magnets with low melting eutectics." Journal of Applied Physics **115**(17): 17A705.

J. Liu, J. D. Moore, K. P. Skokov, M. Krautz, **K. Loewe**, A. Barcza, M. Katter and O. Gutfleisch (2012). "Exploring La(Fe,Si)(13)-based magnetic refrigerants towards application." Scripta Materialia **67**(6): 584-589.

Tugulu, S., **K. Loewe**, D. Scharnweber and F. Schlottig (2010).
"Preparation of superhydrophilic microrough titanium implant surfaces by alkali treatment." Journal of Materials Science-Materials in Medicine **21**(10): 2751-2763.

Iida, K., **K. Loewe**, L. Kuhn, K. Nenkov, G. Fuchs, G. Krabbes, G. Behr, B. Holzapfel and L. Schultz (2009). "Recycling process for 123-type bulk superconductors." Physica C-Superconductivity and Its Applications **469**(15-20): 1153-1156.

Patent application

K. Loewe, W. Fernengel, K. Skokov, O. Gutfleisch (2016).
„Künstlicher Dauermagnet und Verfahren zur Herstellung des künstlichen Dauermagneten“
File number 10 2015 107 486.9 / PCT-file number PCT/EP2016/060633

Conference contributions

2016 Magnetism and Magnetic Materials Conference (MMM), New Orleans, USA.
“Grain Boundary Diffusion of Different Rare Earth Elements in Nd-Fe-B Sintered Magnets by Experiment and FEM Simulation”
K. Loewe, D. Benke, T. Lienig, M. Duerrschnabel, L. Molina-Luna, K.P. Skokov, O. Gutfleisch

2016 International Workshop on Rare-Earth and Future Permanent Magnets and their Applications (REPM), Darmstadt, Germany
“The diffusion of Rare Earth elements in Nd-Fe-B sintered magnets correlated with FEM simulations“
K. Loewe, D. Benke, T. Lienig, K. Skokov, O. Gutfleisch

2016 Symposium of the German Physical Society (DPG), Regensburg, Germany
“Coercivity Enhancement of Nd-Fe-B Permanent Magnets by Grain Boundary Diffusion”
K. Loewe, T. Lienig, D. Benke, O. Gutfleisch

2015 Symposium of the German Physical Society (DPG), Berlin, Germany
“Effect of Microstructure on Spinodal Decomposition and Magnetic Properties of Melt-Spun Alnico”
K. Loewe, M. Duerrschnabel, R. Madugundo, G. C. Hadjipanayis, O. Gutfleisch

2014 International Workshop on Rare Earth and Future Permanent Magnets and Their Applications (REPM), Annapolis, USA
“Temperature Dependent Dy Diffusion Processes in Nd-Fe-B Permanent Magnets”
K. Loewe, C.Brombacher, M. Katter, O. Gutfleisch
+
“Effect of Grain Size on Spinodal Decomposition and Magnetic Properties of Melt-Spun Alnico”
K. Loewe, F. Tabary, B. Frincu, X. Hu, O. Gutfleisch, G. C. Hadjipanayis

2014 Symposium of the German Physical Society (DPG), Dresden, Germany
“The mechanisms of the Dy Grain Boundary Diffusion Process in sintered NdFeB permanent magnets“
K. Loewe, C. Brombacher, M. Katter, O. Gutfleisch

2013 TMS Annual Meeting & Exhibition (TMS), San Antonio, USA
“Investigation of Coercivity Mechanisms in High Performance (Dy,Nd)-Fe-B Permanent Magnets with Core-Shell Structure”
K. Loewe, T. Woodcock, C. Brombacher, M. Katter, O. Gutfleisch, S. Sawatzki (speaker)

2012 IEEE International Magnetics Conference (Intermag), Vancouver, Canada
„The effect of the thermal decomposition reaction on the mechanical and magnetocaloric properties of $La(Fe,Si,Co)_{13}$“

K. Loewe; Liu, J.; Skokov, K.; Moore, J.D.; Sepehri-Amin, H.; Hono, K.; Katter, M.; Gutfleisch, O.

2012 Joint European Magnetics Symposia (JEMS), Parma, Italy
"Investigation of Dy Diffusion Pathways in high performance Nd-Fe-B permanent magnets"
K. Loewe, C. Brombacher, M. Katter, M. Rührig, O.Gutfleisch

Acknowledgement

First of all, I want to thank my supervisor, Prof. Dr. Oliver Gutfleisch, for giving me the opportunity to write my PhD thesis in his work group. During the now almost 7 years in the group, his support and assistance were invaluable and an inspiration to my work.

I also want to thank Prof. Dr. George C. Hadjipanayis, who kindly agreed to co - referee my thesis.

I thank our work group of Functional Materials. During the years, many of you became more than colleagues and were part of the wonderful time I had in Darmstadt. Special thanks goes to Konstantin Skokov, for long hours of discussions and supervision. Learning to produce sintered magnets “Russian style” certainly was fascinating. I thank Christoph Schwöbel and Bahar Fayyazi for correcting my thesis, Imants Dirba for XRD measurements, Leopold Diop and Iliya Radulov for PPMS measurments, Simon Sawatzki for many things along the way, Daniel Simon and Tim Lienig for countless hours with the box, and everyone else who helped to make this work possible.

I thank Christoph Brombacher from Vacuumschmelze GmbH & Co KG for the collaboration for fruitful discussions. Also I thank the BMBF for funding during the PerEMot project.

Last but not least, I am grateful to Wilhelm Fernengel, who always had an open ear for my many practical questions. His comprehensive knowledge and fascination for Nd-Fe-B magnets enabled me to produce my samples with the quality they have.